UNIVERSITAT POLITÈCNICA
DE CATALUNYA
BARCELONATECH

PhD program in Aerospace Science & Technology

Active Flow Control Methods for Aerodynamic Applications

Doctoral thesis by:
Wasim Sarwar

Thesis advisor:
Fernando Mellibovsky

Physics Department - Aerospace Engineering Division
Barcelona, May, 2020.

Acknowledgements

First of all, I would like to express my sincere gratitude to my advisor Prof. Fernando Mellibovsky for his continuous support during the course of PhD research, for his patience, motivation, and the immense knowledge. His guidance helped me all the time in research and the thesis writing. I could not have imagined having a better supervisor and mentor. My sincere thanks also goes to Dr. Josep Bergada, for all the insightful long discussions that played a key role in the completion of this thesis. I thank my fellow lab-mates for the stimulating discussions, for the sleepless nights we were working together, and for all the fun we have had in the last three years.

I would like to thank my family: my mother and brother, sisters, and my wife for supporting me spiritually throughout writing this thesis and my life in general.

Abstract

The cylinder in cross flow has been the subject of many numerical and experimental studies since it provides a deep insight of the physical phenomena occurring in a wide range of flow regimes. Despite a number of investigations at Reynolds number ($Re = 3900$), there has been a constant debate on the important aspects of the flow such as spanwise resolutions, lateral domain extent, convergence of turbulent statistics in the near wake, the so called U-V streamwise velocity profiles at $x = 1D$, where D is the cylinder diameter, and the critical Re for the onset of shear layer instability together with its characterization. In this thesis, an attempt has been made to address some of these issues and report new results through Direct numerical simulations (DNS) by employing spanwise domain extents i.e. $L_z = 1.5D, 2D, 2.5D, \pi D$ at the moderate flow regime i.e. $Re = 2000$, where boundary layer is still laminar while the near wake has gone fully turbulent. Intermittent bursts of shear layer instability have been spotted at this Re indicating the signs of the incipient laminar to turbulent transition in the separating shear layer. It is further confirmed that the secondary instability develops in the regions between the opposite sign large scale spanwise vortices and features a phase lag of 225°. Pseudo-Floquet analysis gives a good prediction of fastest growing mode consistent with the present and previous numerical investigations along with experimental measurements.

In the second part of the thesis, active flow control (AFC) past circular cylinder has been thoroughly investigated with the aid of parametric analysis at the same Re. We applied spanwise-dependent fluidic actuation, both steady and time-dependent, on the flow past a circular cylinder at $Re = 2000$. The actuation takes place in two configurations: in-phase blowing and suction from the slits located at ±90° (top and bottom) with respect to the upstream stagnation point for both steady and time-periodic actuation, and blowing and suction from the top and bottom

slits traveling oppositely with respect to each other in the spanwise direction. Optimal forcing amplitude and wavelength are obtained by sweeping across the parametric space. Spanwise-dependent time-independent forcing with wavelength $\lambda_z = 2D$ has been found the optimal one in terms of drag reduction and attenuation in lift fluctuations. Time-dependent spanwise-dependent forcing via spanwise-traveling-sinusoids with spatial frequency forcing half of the unforced natural vortex shedding frequency yields the highest drag reduction and attenuation in lift fluctuations followed by a forced spatial frequency case with the unforced natural vortex shedding frequency for the AFC configuration with spanwise-traveling-sinusoids.For periodic spanwise-dependent in-phase forcing, an adequate improvement in aerodynamic parameters by forcing at an unforced natural shedding frequency was observed, however, a significant increase in drag and lift-fluctuations was observed when the flow was forced at a frequency close to the unforced shear layer instability, indicating a potential candidate for energy harvesting applications.

Finally, in the last part of the thesis, time-dependence of flow inside novel laminar-fluidic-oscillator has been analyzed using DNS. Again, pseudo-Floquet stability analysis has been utilized to predict the fastest growing Fourier modes along the homogeneous direction. Supplementary three-dimensional numerical study has also been conducted for the suitable cases at various Re. It has been found that steady flow inside fluidic oscillator's cavity bifurcates from steady state to time-periodic state through supercritical Hopf bifurcation. The secondary transition inside fluidic oscillator's cavity occurs through the breaking of flow symmetry about the cavity axis by pitchfork supercritical bifurcation.

Contents

List of Figures

Chapter 1

Introduction

Boundary layer is defined as a thin layer of fluid which has velocity gradients normal to the surface due to the viscosity of the flowing fluid over the surface of an object. Boundary layer flows could be subjected to adverse pressure gradients, such as a body immersed in a fluid flow thickens or the flow moves through widening passages that leads the flow to depart from the surface, and this process of flow detachment from the surface is commonly known as boundary layer separation. Massive suction wakes follow the point of flow separation which leads to the performance degradation in a number of aerospace applications.

The performance of an aerodynamic object is limited by the separation point due to occurrence of heavy energy losses. This flow separation is at the origin of higher aerodynamic drag, vibration, and noise for a wide range of applications such as air, road and sea vehicles; flow past bridge pillars, tall buildings, risers, and power lines etc. Therefore, controlling the boundary-layer/flow separation has been a focal point of many studies [18]. The term boundary-layer-control covers a large spectrum of processes/methods by which boundary layer behavior could be altered. Prominent examples are triggering the transition of boundary layer from laminar to turbulent state, providing excess momentum to boundary layer flow to delay separation etc.

It is well known fact the shear layer instability is caused by Kelvin-Helmholtz mechanism, and its occurrence moves upstream in flow past bluff bodies with the increase in Reynolds number. Figure 1.1(a) shows the schematics of a typical Kelvin-Helmholtz instability developing at the magnetic interface of two fluid streams of different velocities: a magnetic interface separating two regions with background flows of different velocities is subject to a perturbation at stage(2), as the system evolves in time, sufficiently strong flows will amplify the perturbation, causing nonlinear wave steepening at stage(3), until vortex formation occurs in stage(4). Further evolution typically renders the system turbulent. At moderately high Re in the transitional
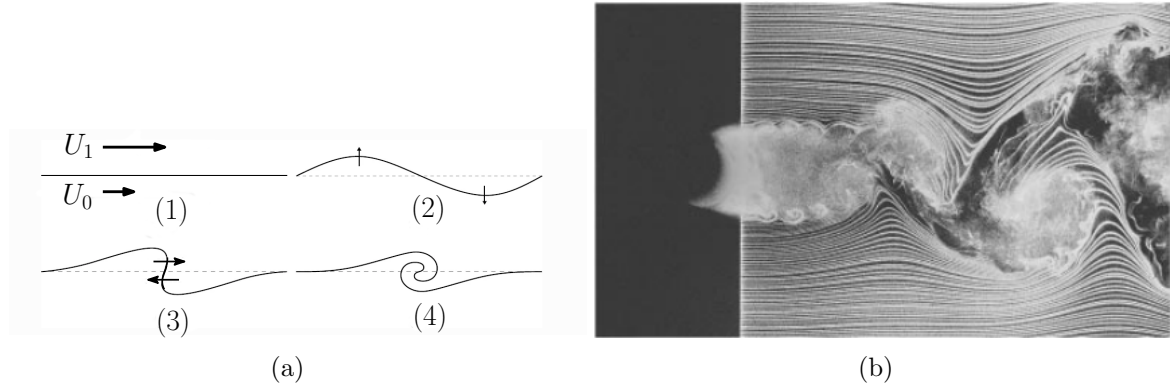
Figure 1.1: Kelvin-Helmholtz instability. (a) development stages of Kelvin-Helmholtz instability at the interface of two flows with different velocities , (b) Kelvin-Helmholtz instability in the shear layers separating from a circular cylinder at $Re = 7000$ [1].

flow regime, Kelvin-Helmholtz instability is observed to occur in the shear layers separated from the circular cylinder surface, flapping synchronously, as shown in figure 1.1(b). In the critical flow regime, it occurs in the proximity of the separation point which leads to flow reattachment and results in significant drag reduction for flow over bluff body [19]. There has been a scatter in the literature about the critical Reynolds number for the onset of shear layer instability, and it has been reported to occur experimentally at the Reynolds number as low as 350 [20] and [1] could not observe it below Reynolds numbers of 2600 for oblique vortex shedding mode. Linear stability analyses have attempted to explain the cause for this disagreement and linked it to convective nature of shear layer instability [21] which might be triggered by the background noise in the experiments and due to the amplification of round off errors via non-linear effects in the computations. It has been well documented that shear layer instability could be excited within some ranges of frequencies even at lower Reynolds number [22]. Active flow control (AFC) experienced explosive growth from the pioneering experiments of Prandtl in 1904. Ever since a huge number of research efforts have been spent to seek the optimal control methods to manipulate the flow field around the aerodynamic bodies. AFC attains control authority via addition/subtraction of momentum in the mean flow, which varies from brute-force approaches, in which forcing amplitude is sufficient enough to modify the mean flow, to more effective techniques [23, 24, 25] which exploits inherent flow instabilities using small amplitude disturbances, especially, spanwise modulation [26] has been proven utterly effective for the attenuation, and even suppression in the laminar regime, of primary instability of bluff body wakes alongside substantial reduction of drag force

2
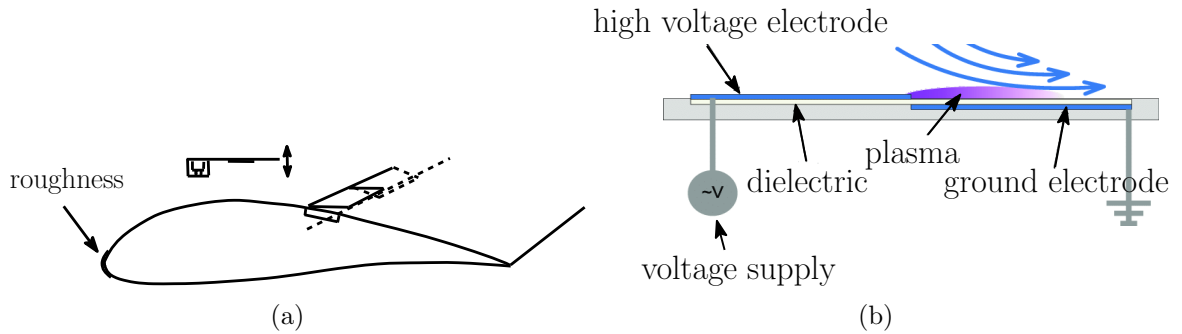
Figure 1.2: Active flow control devices. (a) The insert shows the IAIPr8 airfoil, the cavity, and a schematic description of the actuator [2], (b) schematic of plasma actuator [3]

for a wide range of flow regimes. Time-dependent actuation of flows past bluff bodies has also demonstrated promising results in the subcritical flow regimes [27, 28, 29].

In order to realize the flow control past bluff bodies various kinds of actuators have been developed over the decades and we provide an overview of the recently developed devices for active flow control applications.

AFC actuators can be classified into different types, based on their operation [18] as described below

Moving object/surface

In this classification, flow is actuated by means of physical motion (translation/rotation) of the actuator. Prominent examples are moving surfaces [30] and mechanical valves. These device interact with the near flow field by introducing perturbation through the motion of external surfaces, which in turn energises the fluid. vibrating flaps [2] is the one such example as shown in figure 1.2(a). The downside of these devices is that they are subject to mechanical failure due to the presence of moving parts and require regular maintenance.

Plasma actuators

The working of these type of actuators is based on the plasma, formed between the oppositely charged electrodes arranged asymmetrically, by the application of high voltage. The surrounding fluid is ionized and accelerated under the action of applied electric field as indicated in figure 1.2(b). These devices have recently gained popularity owing to their solid state nature and fast response time. Prominent examples include single dielectric barrier discharge (SDBD) [3], and in particular, local arc filament [31], spark-jet [32] are famous for high speed applications.

Fluidic

3

These are the most common type of flow actuators which introduce perturbation in the mean flow through injection or suction of fluid. These are further sub-classified into zero-net-mass-flux (ZNMF) actuators and non-ZNMF actuators. In ZNMF devices, a periodic disturbance is introduced into the mean flow by means of alternate ingestion and expulsion of the surrounding fluid without the need of any source/sink . Synthetic jet (see figure 1.3(a)) is the prominent example of this type. In contrast, the non-ZNMF actuators require supply input for their operation and, consequently, produce pulsating-jets/sweeping-jet based on the type of actuator. Sweeping/spatially oscillating fluidic oscillators are further divided into feedback-free [33], single-feedback [34] and two-feedback channel fluidic oscillators (see figure 1.3(b), two feedback channel fluidic oscillator). A number of experimental studies have been conducted on these device due to the renewed interest in these devices for their higher robustness and reliability.
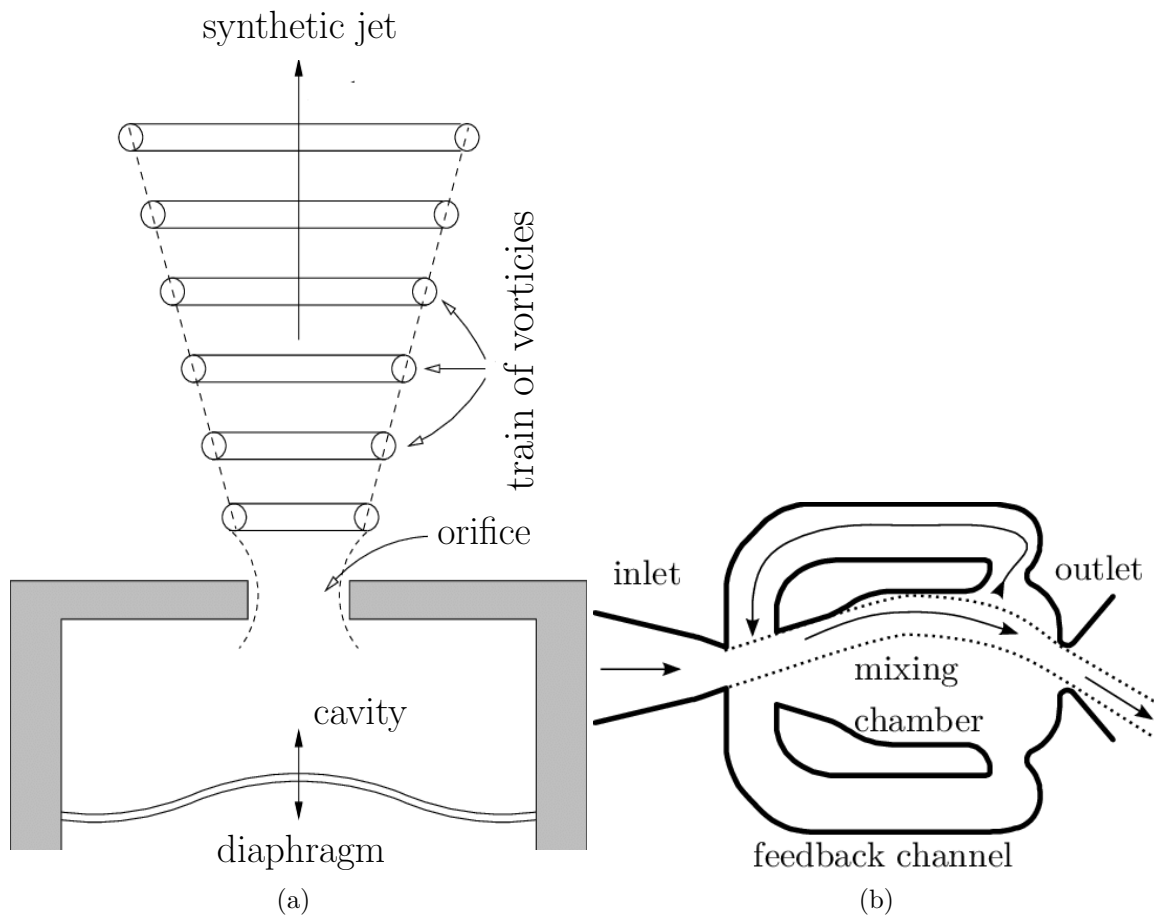
Figure 1.3: Active flow control devices. (a) synthetic jet actuator [4], and (b) a typical two-feedback channel fluidic oscillator

1.1 Objective of the present thesis

The objective of this present PhD thesis is the numerical investigation of flow past circular cylinder in the transitional regime together with the implementation of AFC to improve the aerodynamic performance through suction and blowing from the slits located at the top and bottom of the circular cylinder in the in-phase configuration.

The flow behind circular cylinder is, essentially, a canonical problem for flow past bluff bodies so it provides a framework for the deep understanding of various physical phenomena occurring in the wake of bluff bodies such as the ones mentioned earlier. Numerical solution of flow past cylinder will be integrated for sufficiently long time to obtain converged statistics for primary and shear layer instability frequencies which will be later used for the time-dependent actuation of flow past circular cylinder.

AFC will be applied to flow past circular cylinder at the same Reynolds number. Parametric study will be opted to explore the optimal forcing amplitude, wavelength and actuation frequency to improve the aerodynamics performance. Time-dependent actuation of flow past circular cylinder will be applied in two configurations: in-phase blowing and suction from the slits located at $\pm 90°$ with respect to upstream stagnation point, and blowing and suction traveling oppositely with respect to each other in the spanwise direction. Time-dependence will be investigated for flow inside a novel laminar fluidic oscillator in the framework of dynamical systems and bifurcation theory.

1.2 Outline of the thesis

This dissertation is aimed at the aerodynamic analysis of flow past circular cylinder in the transitional regime with and without forcing, and time-dependence investigation of laminar fluidic oscillator using high order numerical methods $i.e.$ Spectral element methods (SEM). Chapter 2 is concerned with the study of three dimensional wake of circular cylinder via DNS, analyzing in detail the vortex shedding of primary instability along-with the computation of secondary instability's length scales. Different spanwise domain lengths are considered to evaluate the relevant impact of spanwise domain length on the so called U-V streamwise velocity profiles in the near wake. Pseudo-Floquet analysis has been carried out to find the fastest growing mode along with the identification of regions where growth is maximized.

Chapter 3 deals with the parametric study related to the forcing of the flow past a circular cylinder at the same Re. Time-dependent actuation from the top and bottom

slots on the cylinder surface, in in-phase configuration, has been applied and optimal forcing wavelength, forcing amplitude, and forcing frequency has been identified. It also contains the quantification of drag reduction and suppression of lift fluctuation for various types of flow actuation methods and highlights the corresponding explanation of the prospective mechanisms for the drag reduction.

In Chapter 4, different flow regimes have been characterized in the novel-laminar-fluidic-oscillator. The physical mechanism underlying the transition from steady to time-periodic flow state has been identified and its subcritical/supercritical nature has been evaluated via high order numerical method. The second transition inside fluidic oscillator leading to asymmetric flow about the fluidic oscillator axis has been characterized as well and the relevant physical mechanism driving this transition is identified. The final chapter presents the concluding remarks and suggests the possible future work.

Chapter 2

Investigation of flow past circular cylinder at Reynolds number ($\boldsymbol{Re} = 2000$)

2.1 Introduction

The flow past a circular cylinder is a canonical problem for flow past bluff bodies. A large number of numerical and experimental studies have been conducted over a wide range of Reynolds number to gain deep understanding of the flow phenomena occurring behind bluff bodies such as laminar to turbulent transition, separating shear layers and shedding of Kármán type vortices.

The flow past a circular cylinder features a two-dimensional steady symmetric wake behind circular cylinder which progressively increases in longitudinal extent with Reynolds number and destabilizes at $Re \lesssim 47$, ($Re = UD/\nu$ is the Reynolds number based on cylinder diameter D, upstream flow velocity U and fluid kinematic viscosity ν), into a still two-dimensional time-dependent (space-time-symmetric) flow, so-called von Kármán vortex shedding, characterized by alternate shedding of vortices from the opposite sides of a cylinder [35]. This flow regime is at the origin of increased aerodynamic drag [36, 37], vibration [38, 39], and acoustic noise [40, 41].

The two-dimensional nature of von Kármán shedding has been reported to endure for $Re \lesssim 190$, beyond which spanwise invariance is broken. The two-dimensional wake flow becomes unstable to two distinct types of three-dimensional modes i.e. mode A and mode B reported in the literature in the so-called wake transition regime $Re \in 180, 260$, possess not only distinct length scales but also different symmetry properties that hint at the potentially different triggering mechanisms. Their inception is also responsible for the appearance of discontinuity in the Strouhal curve as a

function of Re [42]. Mode A is characterized by the inception of vortex loops that are stretched by shear to give rise to streamwise vortex pairs with spanwise wavelengths $\lambda_z = 3D \sim 4D$. Mode A has been detected from as low as $Re \gtrsim 180$, such that it co-exists with the two-dimensional periodic state in a small Re-range which characterizes the flow behavior as hysteretical and, consequently the spanwise-invariance-breaking bifurcation being sub-critical [43]. Mode B, on the other hand, appears at a slightly higher $Re \gtrsim 250$ with characteristic wavelength $\lambda_z = 1D$ [44] compared to Mode A. Mode B is, infact, a manifestation of the second spanwise-invariance-breaking bifurcation of the already unstable two-dimensional periodic state at $Re \sim 259$ [37]. The evolution from mode A to mode B involves intermittency i.e. the transfer of the time-fraction of occurrence of Mode A and B from former to latter. Mode B becomes the dominant structure at $Re \simeq 260$ and exhibits remarkable spanwise-coherence.

vortex dislocation also exists in the so-called wake transition regime that appear in the form of intermittent large-scale spot-like structures that dominate the wake as they are convected downstream [45, 46]. Their appearance results in low frequency irregular fluctuation in the wake together with discontinuous drop of shedding frequency.

The boundary layers separated from the either side of the circular cylinder undergo turbulent transition at high Re [47] by the onset of Kelvin-Helmholtz instability that only becomes detectable from $Re \gtrsim 1200$ [46, 1]. The Kelvin-Helmholtz instability in its nascent stage appears in the form of small scale vortices that accumulate downstream and subsequently dominated by primary instability. Kelvin-Helmholtz instability frequency has been reported to scale as $f_{\mathrm{KH}}/f_{\mathrm{vK}} \sim Re^{1/2}$ [46] based on outer velocity and boundary layer thickness at separation, where the subindices in f_{KH} and f_{vK} stand for Kelvin-Helmholtz and von-Kármán, respectively. However, a best fit to a collection of experimental data suggest a scaling should rather be $f_{\mathrm{KH}}/f_{\mathrm{vK}} \sim Re^{0.67}$ [48, 1]. The apparent resonance between f_{KH} and f_{vK} at $Re \simeq 260$ [1] has been considered a reason for high spanwise-coherence of mode B at this particular value of Re.

Spanwise end-conditions and aspect ratio have been reported to dictate the vortex shedding from a circular cylinder in the transitional regime. In the early transition regime, a large scatter in the spanwise-wavelength of structures has been observed in the range $\lambda_z \in [3,5]D$, [49, 14, 50, 51, 52], but when data including local-phase dislocation was properly filtered, the spanwise wavelengths followed closely the maximum growth rate predicted by linear stability analysis, $\lambda_z^{\mathrm{A}} = 3.96D$. In the late transitional regime, where mode B is dominant, the spanwise-wavelength scattering

is already low and wavelengths $\lambda_z \simeq 1D$ are observed in the near wake ($x/D < 3$), close enough to the second linear instability of the already unstable two-dimensional vortex shedding flow, with $\lambda_z^{\mathrm{B}} = 0.82D$. In this regime, the spanwise wavelength has been reported to scale as $1/\sqrt{Re}$ [50], confirmed by experimental investigation in the range $Re \in [300 - 2200]$ [14]. In the far wake ($x/D > 10$), however, the same experiment report that the spanwise wavelength becomes fairly independent of Re and remains of order $\lambda_z/D \sim O(1)$ [14].

The variation of the spanwise wavelength of streamwise vortices along the wake at fixed Re has been analyzed both experimentally [14, 15], using both flow visualization and two-probe cross-correlation, and numerically [13], through the use of the Hilbert transform. The cross-flow sampling location has a large impact in the near-wake structures length-scale, which renders any comparison impractical. Sufficiently far downstream away from the cylinder, in the far wake, this effect is less noticeable and the typical wavelength is observed to clearly saturate at a fairly constant value.

There exists ample experimental evidence, backed by sound theoretical arguments, that turbulence in spatially developing flows depends, even asymptotically, on upstream conditions (*i.e.* the particulars of the turbulent flow generator) [53, 54]. This holds true for planar wakes [55] and, in particular, for the turbulent wake past a cylinder. Planar wakes past blunt bodies of characteristic blockage size D can be split in four distinct regions, namely the near wake ($x/D \lesssim 4$), the mid wake ($4 \lesssim x/D \lesssim 50$), the far wake ($50 \lesssim x/D \lesssim 1000$) and the asymptotic wake ($x/D \gtrsim 1000$) [56]. The near wake is subject to direct interaction with the wake generator and bears strong correlation with aerodynamic parameters such as the base pressure coefficient or the aerodynamic forces on the body. Beyond this wake formation region, which contains the mean recirculation bubble, no action or perturbation has any mensurable effect whatsoever on the flow field around the body. The mid wake is different from the far wake in that shed vortices remain detectable, while the mean flow becomes self-similar in the far wake. A certain universality develops in the asymptotic wake, if only for conveniently scaled (with the local centerline velocity deficit and the local length scale) mean velocity profiles. Meanwhile, spreading rates and high order turbulent moments, including Reynolds stresses, can in principle depend on upstream conditions [54]. In the case of the cylinder wake, complete self-preservation has been established experimentally at $Re = 2000$ beyond $x/D \gtrsim 260$ [57].

While mean flow statistics are fairly independent of Re in the far wake behind a cylinder once within the shear-layer transition regime ($Re \gtrsim 1200$), second order flow statistics (Reynolds stresses) only become so for $Re \gtrsim 10000$ [58].

There is considerable consensus as to the mid wake flow topology within the early shear-layer transition regime, as evidenced by the good agreement across a wide range of experimental [59, 60, 61, 9, 11] and numerical [62, 63, 64, 65, 66, 67, 11, 68] studies of crossflow distribution of mean velocity components at varying flow rates. High order flow statistics also show reasonable agreement provided that sufficiently close Re are considered.

In the near wake, besides the fact that statistics are no longer expected to be independent of Re, results are at odds among the various experimental and numerical studies, even at coincident Re. In trying to shed light on the cause for disagreement, the flow at $Re = 3900$ has become a recurrent benchmark case since the experiments of [59] and [61]. Two distinct flow states have been reported, named U- and V-type after the outline of the mean streamwise velocity crossflow profile in the very near-wake of the cylinder at $x/D = 1$. The U-state is characterised by a longer recirculation bubble L_r (not to be confused with wake formation length), a slightly higher vortex shedding frequency f_{vK}, lower base pressure suction coefficient $-C_{p_b} = 2(p_\infty - p_b)/(\rho U_\infty^2)$, lower aerodynamic forces (mean drag C_D and root-mean-square of lift $C_{L_{\mathrm{rms}}} = \sqrt{\langle C_L^2 \rangle}$), lower Reynolds stresses $\langle u'u' \rangle$, $\langle u'v' \rangle$ and $\langle v'v' \rangle$, and characteristic double-peak distributions of $\langle u'u' \rangle$ both in the streamwise direction along the wake centerline and in the near-wake cross-stream direction [62, 63, 11, 66, 65, 67, 69, 70, 68, 71]. The V-state, in contrast, features a smaller L_r, slightly lower f_{vK}, higher $-C_{p_b}$, C_D, $C_{L_{\mathrm{rms}}}$, and $\langle u'u' \rangle$, $\langle u'v' \rangle$ and $\langle v'v' \rangle$, and inflection plus single-peak streamwise and four-peak cross-stream distributions of $\langle u'u' \rangle$ [59, 66, 65, 72, 69, 70, 68, 71]. Table 2.1 summarizes a number of experiments, along with relevant experimental conditions and a bunch of flow parameter results that allow characterization of the corresponding type of solution. The experiments, run at several $Re \sim O(10^3)$ on experimental setups of different spanwise extent, include Particle Image Velocimetry (PIV), Laser Doppler Velocimetry (LDV) and Hot Wire Anemometry (HWA) measurements and varying levels of free-stream turbulence (Tu). Statistics have been collected over variable counts of vortex shedding cycles. It becomes clear from the flow parameter values, that V-type solutions are favoured at large Re or in the presence of higher Tu, U-type profiles being common for sufficiently low Re and low Tu experiments. These studies also seem to point at a gradual transition from one state to the other as Re is increased in the same experimental setup with all other parameters constant.

Table 2.2 contains an extensive list of numerical simulations of the flow past a circular cylinder at Reynolds numbers relevant to the regime under scrutiny. Summarised alongside the main results (to be compared with the experimental results

Table 2.1: Literature review of experimental results for the flow past a circular cylinder. Reported are, when available, the flow measurement method (HWA: hot wire anemometry; PIV: particle image velocimetry; LDV: laser doppler velocimetry), preturbulence level Tu, Reynolds number Re, cylinder span size L_z, number of vortex shedding cycles recorded for statistics N_s, von Kármán frequency f_{vK}, Kelvin-Helmholtz frequency f_{KH}, wake instability frequency f_w, recirculation bubble length L_r, mean drag coefficient C_D and rms fluctuation C'_D, lift coefficient rms fluctuation C'_L, base pressure coefficient $-C_{p_b}$, and location of the boundary layer separation θ_{sep}

Experimental

Author [Ref]	Method	Tu	Re	L_z	N_s	f_{vK}	f_{KH}	f_w	L_r	C_D	C'_D	C'_L	$-C_{p_b}$	θ_{sep}
Norberg [6]	HWA	0.1%	2000	240	?	0.213			1.65	0.98			0.84	
		1.4%	3000	80		0.209			1.44	1.03			0.89	
		0.1%	3000	80		0.204			0.99	1.13			1.05	
		0.1%	8000	80		0.199			0.90	1.20			1.12	
		1.4%	8000	80						0.98				
Lourenco and Shih [59]	PIV	0.67%	3900	84	7680				1.18					
Ong and Wallace [61]	HWA	?	3900	21	29	0.21							??	
Norberg [9]	LDV	< 0.1%	1500	65	1350									85±2
Norberg [7]	LDV	< 0.1%	3900	65	?	0.212			1.79					
		< 0.1%	1500	65		0.210			1.66					
		< 0.1%	3000	65					1.40					
		< 0.1%	5000	65					1.17					
		< 0.1%	8000	65					1.02					
		< 0.1%	10000	65										
Konstantinidis et al. [10]	LDV	< 0.1%	1500	105	?	0.215			1.77			0.045		
		< 0.1%	4400	105								0.100		
Konstantinidis et al. [12]	PIV	3.3%	1550	10	?									
		3.3%	2150	10										
		3.3%	2750	10										
		3.3%	7450	10										
		3.3%	2160	10					1.58					
Konstantinidis and Balabani [8]	PIV	3%	2150	10	?	0.215								
Dong et al. [73]	PIV	?	4000	8.78	2856				1.47					
Parnaudeau et al. [11]	PIV	< 0.2%	3900	20	250	0.208			1.51					
	HWA	< 0.2%	3900	20										

11

of table 2.1) are the most significant simulation parameters such as the numerical method used, the spanwise periodic extent of the domain, in-plane and spanwise resolutions (and order of the discretisation) and the number of vortex shedding cycles collected for statistics. The in-plane domain size and the time discretisation method and order have been deemed appropriate for all cases and are therefore not reported. The last column indicates whether the reported results feature a U-type or V-type cross-stream velocity profile in the near wake and/or the statistically averaged results are compatible with one or the other. UV indicates results that appear to be halfway between U- and V-type states, while the question mark denotes inconclusive results.

There has been much controversy as to whether there is a unique near wake topology or, if both states may occur, under what circumstances should one or the other be expected.

Based on L_r and C_{p_b} as indirect indicators, a gradual transition from the U-toward the V-state with increasing Re has been reported by several experimental studies [78, 79, 80, 6]. The U-state would seem to dominate at $Re \sim 2000$, while the V-state has completely taken over from $Re \gtrsim 10000$ on. This trend has been later confirmed by direct measurement of mean and second order flow statistics in the near wake of the cylinder [9]. Increased preturbulence levels Tu have been shown to shift the gradual transition to slightly lower Re-values [6], while an insufficient cylinder aspect ratio L_z/D, such that the spanwise boundary conditions drive the flow, has a stabilising effect for the U-state [5]. This suggests that the spanwise size of near-wake structures might be playing an important role on near-wake flow statistics, as numerics seem to substantiate [65, 73, 77]. Simulations are usually undertaken with periodic boundary conditions in the spanwise direction and an insufficient spanwise domain size ($L_z/D \leq \pi$ at $Re = 3900$) has been shown to favour the U-state, all other parameters kept constant. The V-state can however be artificially recovered in small domains when the spanwise direction is under-resolved [74, 63, 64, 66, 69, 70] allegedly due to insufficient viscous dissipation of turbulent kinetic energy. The same applies to overly coarse in-plane resolutions, which also result in V-state selection [66, 71]. In the case of LES simulation, over-dissipative subgrid scale models also tend to induce the U-state even in domains of allegedly sufficient spanwise extent [65, 71], while under-dissipative models induce V-type profiles in short spanwise domains [71, 69, 70].

The large scatter of results, which yield conflicting values for most of the mean integral quantities, has ocasionally been ascribed to unconverged statistics due to exceedingly short time series of data (insufficient sample size) [67, 69], although this alone cannot explain all of the observed discrepancies. A statistical analysis of near

12

Table 2.2: Literature review of numerical results for the flow past a circular cylinder. Besides some of the parameters reported in table 2.1, listed are the numerical method employed (DNS: direct numerical simulation; LES: Large Eddy simulation; FVM: Finite Volumes Method; FDM: Finite Difference Method; SEM: Spectral Element Method; SDM: Spectral Difference Method), the spanwise periodic extent of the domain L_z, the in-plane N_{xy} and spanwise N_z resolutions (the superindex indicates discretisation order, F for Fourier) and near wake solution topology Sol (U: U-state; V: V-state; UV: mixed; ?: inconclusive)

Author [Ref]	Method	Re	L_z	N_z	N_{xy}	N_s	f_{vK}	f_{KH}	f_w	L_r	C_D	$-C_{pb}$	θ_{sep}	Sol.
Present results: case 1	DNS SEM	2000	1.5	64	4040^8	66	0.218	1.237		1.50	1.015	0.88	92.0	U
case 2			2	64	4040^8	58	0.212	1.121		1.58	0.987	0.83	90.3	U
case 3			2.5	128	5484^8	55	0.215	0.839		1.66	0.975	0.80	90.0	U
case 4			π	96	5484^8	22	0.211			1.71	0.961	0.79	90.0	U
Lehmkuhl et al. [68]	DNS FVM	3900	π	128	72700	858	0.215	1.34	0.0064	1.36	0.935	0.88	88	UV
						L:250	0.218			1.55	0.979	0.98	87.8	U
						H:250	0.214			1.26	0.877	0.98	88.3	V
Gsell et al. [13]	DNS FVM	3900	2π	300	150000	330	0.21			1.35	0.93		86.8	UV
Kravchenko and Moin [66]	LES FDM	3900	π	48^F	27780^S	7	0.21	1.365		1.363	1.019	0.933	88	UV
Ma et al. [65]	DNS SEM	3900	π/2	48	10570	?	0.203			1.59	0.84			V
			1.5π	8	27780		0.206			1.04	0.98			UV
			2π	24	9021^{10}		0.212			1.30	0.97			V
			1.5π	48	9021^{10}		0.219			1.07	1.07			UV
Mittal [74] ($c_s = 0.032$)	LES SEM	3900	1.5π	64^F	9028	7	0.213			1.28	0.898		88	U?
($c_s = 0.196$)			1.5π	64^F	9028	7	0.208			1.76	0.765		89	U?
Mittal [63]	LES FDM	3900	π	48^F	48120	12	0.203			1.40	1.0	0.93	86.9	UV?
							0.206			1.36	0.95	0.95	85.8	V
Breuer [64]	LES FVM	3900	π	64	27225	>22	0.215		~0.007	1.372	1.016	0.941	87.4	UV?
				32			0.215			1.043	1.097	1.069	88.5	V
				32			0.215			1.686	0.969	0.867	86.7	U
				64			0.215			1.115	1.099	1.049	87.9	V
							0.215			1.114	1.036	1.036	88.2	V
Dong et al. [73]	DNS SEM	3900	1.5π	128^F	9028	40–50	0.21?	1.539		1.36	0.978	0.85	88.2	V
				192^F	111443		0.208			1.18				V
Franke and Frank [67]	LES FVM	3900	π	33	35584	42	0.209			1.64				UV
			2π	64			0.215							U
Chen et al. [71]	iLES FVM	2580	π	56	70000	50	0.206			1.00	0.95	0.73		V
			π	20	12500	50	0.22			1.66		1.04		U
Mohammad et al. [75]	iLES SDM	2580	π	18^3	7880^3	20	0.210			1.12	1.03	0.88	87.4	V
			π	18^2	7880^2	20	0.208			1.18	0.93	0.96		UV
Lodato and Jameson [76]	iLES SDM	2580	3.2	10^3?	1847^3?	300	0.214						87.3	U
Wissink and Rodi [77]	DNS FVM	3300	4	512	416556	10	0.216						90.3	V
				256	63336		0.216						90.3	U
Beaudan and Moin [62]	DNS FDM	3900	π	48^5	19584^5	6	0.216			1.56	0.96	0.89	85.3	U
Tremblay [72]	DNS FVM	3900	π	112	419364	60	0.22			1.3	1.03	0.93	85.7	UV

wake velocity time series from direct numerical simulation, spanning over 800 vortex shedding cycles, detected a very low frequency of about 3% of the Strouhal number that was traced back to an instability of the mean recirculation bubble size [68]. Conditional and phase averaging revealed that the mean statistics might be in fact the weighted mean of two modes, a high and a low energy mode, corresponding to the V- and U-state, respectively. In this light, the scatter of inconsistent results would be a consequence of averaging too short time-series at different phases along the low frequency cycle. The low-pass filtered signals do not consist of memoryless intermittent switching between the two so-called modes, such that the scenario of two strange saddles linked by heteroclinic connections can be discarded altogether. The temporal dynamics would rather correspond to an instability of a unique state, although further inquiry shall be required to test this hypothesis. In any case, the physical mechanism underlying the low frequency evolution of the near wake remains unaccounted for. The loopback mechanism by which the high energy short recirculation bubble should progress towards a lower energy longer bubble and then back remains a mistery. Even though the unconverged statistics issue might apply to almost all preceding numerical studies and a few of the experiments [59], most experimental studies analyse sufficiently long data series that the low frequency could have been detected and the mean state obtained [6, 9, 10, 73, 11]. Instead, U-type near wake statistics are reported in most cases.

All things considered, it would seem that there is in fact a gradual shift from U- to V-type near wake statistics as Re is increased and that the former is still dominant at $Re = 3900$. Observation of V-type short recirculation bubbles would therefore be an artifact of either biased statistics or, in the case of numerical simulation, too coarse a resolution to capture the dissipative length-scales.

In this chapter we focus here on the cylinder shear layers and wake regime at $Re = 2000$, with the intention of probing the occurrence of the U- and V-states when the Kelvin-Helmholtz instability is perceptible but sufficiently weak that turbulent statistics are modest in the near wake. Comparison with $Re = 3900$ will be established once the simulation has been calibrated against experimental [1, 81, 6, 9, 7, 10, 12] and numerical [77, 75, 76, 71] data at $Re \in [1500 - 3000] \sim 2000$.

2.2 Problem formulation and numerical approach

The incompressible flow around an infinitely long spanwise-aligned circular cylinder is governed by the Navier-Stokes equations, which, after suitable non-dimensionalization

with cylinder diameter D, fluid kinematic viscosity ν and upstream flow velocity U, read

$$\frac{\partial \mathbf{u}}{\partial t} + (\mathbf{u} \cdot \nabla)\mathbf{u} = -\nabla p + \frac{1}{Re}\nabla^2 \mathbf{u},$$
$$\nabla \cdot \mathbf{u} = 0,$$

(2.1)

where $\mathbf{u}(\mathbf{r};t) = (u, v, w)$ and $p(\mathbf{r};t)$ are the non-dimensional velocity and pressure, respectively, at non-dimensional location $\mathbf{r} = (x, y, z)$ and advective time t. x (u), y (v) and z (w) denote streamwise, crossflow and spanwise coordinates (velocity components), respectively. $Re = UD/\nu$ is the Reynolds number. The domain in the streamwise-crossflow plane takes $(x, y) \in [-20, 50] \times [-20, 20]$ (see figure **??**), while periodic boundary conditions $[\mathbf{u}, p](\mathbf{r} + L_z\hat{\mathbf{k}}; t) = [\mathbf{u}, p](\mathbf{r}; t)$ are assumed in the spanwise direction with periodicity length $L_z = 2$. The spanwise domain extent has
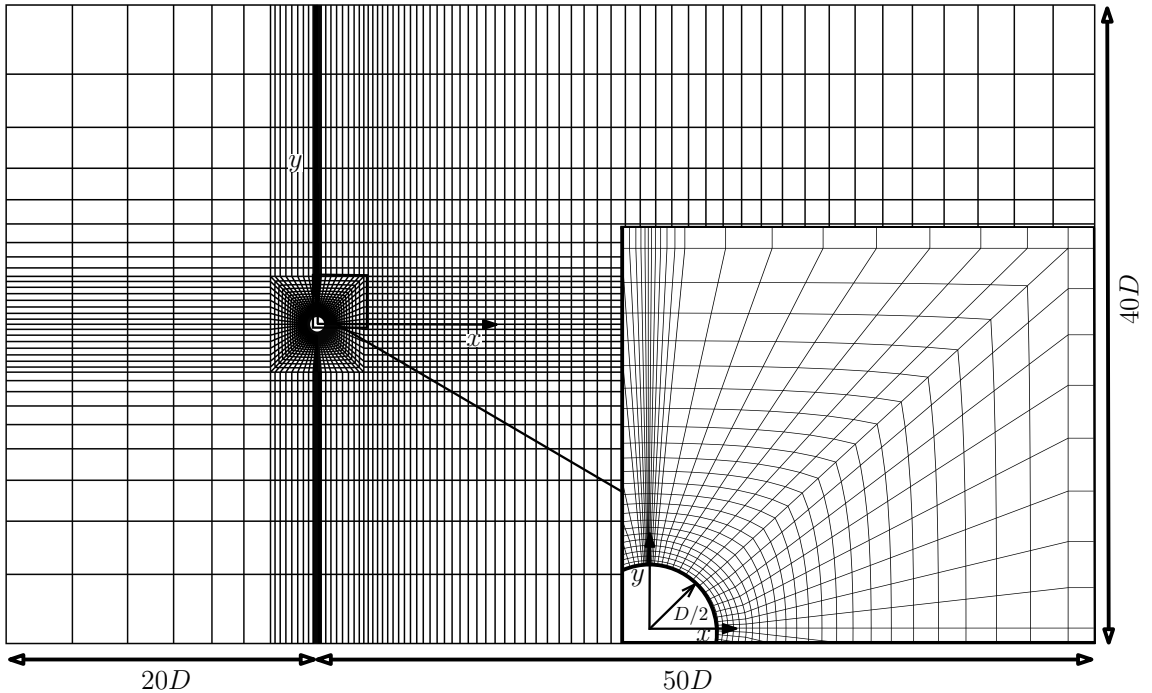
Figure 2.1: Computational domain and mesh. The inset shows a detail of the mesh around the cylinder and in the near wake. The streamwise-crossflow plane is discretised in high order quadrilateral spectral elements.

been chosen to fit a minimum of three typical spanwise structures (streamwise vortex pairs) in the near wake, as estimated by the empirical scaling $\lambda_z \sim 20Re^{-0.5}$ at $x = 3$ [14]. The size of the structures is known to grow along the wake [14, 61] but not as much as to not fit in the computational domain. The boundary conditions for velocity are unitary Dirichlet at the upstream boundary $\mathbf{u}(-20, y, z) = \hat{\imath}$, non-slip on the cylinder wall $\mathbf{u}_w = 0$, slip wall on the upper and lower boundaries $\partial_z u(x, \pm 20, z) =$

$v(x, \pm 20, z) = \partial_z w(x, \pm 20, z) = 0$ and homogeneous Neumann at the downstream boundary $(\nabla \mathbf{u} \cdot \hat{\mathbf{n}})(50, y, z) = 0$. For pressure, high order homogeneous Neumann boundary conditions are applied everywhere except for the downstream boundary, where homogeneous Dirichlet conditions $p(50, y, z) = 0$ are imposed.

The flow has been evolved in time using the incompressible Navier-Stokes solver of the tensor-product-based spectral/finite element package Nektar++ [82]. Spatial discretisations of 5484 and 4040 high-order quadrilateral elements have been employed in two different meshes in the streamwise-crossflow plane, with Lagrange polynomial expansions up to order $P - 1 = 7$. A continuous Galerkin projection has been enforced across element boundaries. A particularly refined mesh has been set up in the vicinity of the cylinder, as shown in the inset of figure 2.1, to properly resolve boundary layers and separation, as well as in the near wake, where turbulent fluctuations may have significant impact on the flow field topology around the cylinder. Fourier expansions with resolutions $N_z = \pm 64, \pm 96, \pm 128$ modes have been deployed in the periodic spanwise direction along with Orzag's 3/2 rule for dealiasing. For AFC implementation, a mesh with 5484 high order quadrilateral elements has been employed in the streamwise-crossflow plane along with Fourier expansion with spanwise resolution $N_z = \pm 64$. In order for the discrete operators to preserve the symmetries of their continuous counterparts, the advection term has been written in skew-symmetric form. For the time discretisation, a second order velocity-correction splitting scheme with a time-step $\Delta t = 0.0002$ has been adopted as providing sufficient time-integration accuracy.

The instantaneous velocity field has been split following

$$\mathbf{u}(\mathbf{r}; t) = \bar{\mathbf{u}}(\mathbf{r}_2) + \underbrace{\mathbf{u}_2'(\mathbf{r}_2; t) + \mathbf{u}_3(\mathbf{r}; t)}_{\mathbf{u}'(\mathbf{r}; t)}, \tag{2.2}$$

where $\mathbf{r}_2 = (x, y)$ and $\bar{\mathbf{u}} = (\bar{u}, \bar{v}) = \langle \mathbf{u} \rangle_{zt}$ is the spanwise- and time-averaged two-dimensional mean velocity field. $\mathbf{u}' = (u', v', w')$ is the time-dependent (fluctuating) velocity field. The von Kármán spanwise vortex shedding mode is represented by

$$\mathbf{u}_2'(\mathbf{r}_2; t) = \mathbf{u}_2(\mathbf{r}_2; t) - \bar{\mathbf{u}}(\mathbf{r}_2), \tag{2.3}$$

with $\mathbf{u}_2(\mathbf{r}_2; t) = \langle \mathbf{u} \rangle_z$ the spanwise-averaged instantaneous two-dimensional velocity field. Finally, $\mathbf{u}_3 = \mathbf{u} - \mathbf{u}_2$ represents the purely three-dimensional perturbation velocity field. The Reynolds stress tensor is defined to include the fluctuations both

due to von Kármán vortex shedding and the three-dimensional deviation away from it:

$$- \langle \mathbf{u}' \otimes \mathbf{u}' \rangle = - \begin{pmatrix} \langle u'u' \rangle & \langle u'v' \rangle & \langle u'w' \rangle \\ & \langle v'v' \rangle & \langle v'w' \rangle \\ & & \langle w'w' \rangle \end{pmatrix}. \tag{2.4}$$

2.3 Baseline case discussion

2.3.1 Global quantities

The most salient global quantities that result from our numerical simulations are listed in table 2.2. The statistics are deemed sufficiently converged for cases 1 through 3, while case 4 may require longer runs. Cases 3 and 4 have enhanced in-plane resolution with respect to 1 and 2 (5484 against 4040 7th-order spectral elements), while spanwise resolution is highest for case 3 ($\sim$ 50 Fourier modes per spanwise unit), followed by case 1 ($\sim$ 42), case 2 ($\sim$ 32) and case 3 ($\sim$ 31). The lowest resolutions used here qualify as broadly adequate in view of published literature and, all other parameters kept constant, only further coarsening had an observable effect on statistics. On the other hand, increasing the spanwise size of the domain from $L_z = 1.5$ (case 1) to 2.5 (case 3) does have a noticeable impact on all global quantities, while further increase to $L_z = \pi$ has little to no effect. We will therefore focus the analysis on case 3, as it gathers the highest resolution, seemingly adequate spanwise extent, and the sufficiently long time integration that is required to produce well converged statistics.

Vortex shedding frequency $f_{\mathrm{vK}} = 0.215$ stands in perfect agreement with experiments both at the same or close-by Reynolds number [6, 10, 8] and at noticeably higher Re [61, 6, 7, 11], given that the evolution of the Strouhal number in this regime is rather flat [5].

Mean drag coefficient has not often been reported in experiments, but our result $C_D = 0.975$ is in very close agreement with the few cases where it has [6, 59]. Consistency with numerical simulations at similar Re is also good [71] and the somewhat higher values reported at the very common $Re = 3900$ are entirely compatible with the slightly increasing trend expected in this regime. Also the lift coefficient r.m.s. fluctuations $C'_L = 0.102$ fall within the range reported in the only experiments where these have been measured [7].

The distribution of the mean pressure coefficient $C_p(\theta)$ (solid line) along the cylinder wall is shown in figure 2.2a. The stagnation point, clearly identifiable with $C_p(0) = 0$ at $\theta = 0°$, is followed by a quick descent of C_p as the flow accelerates

17
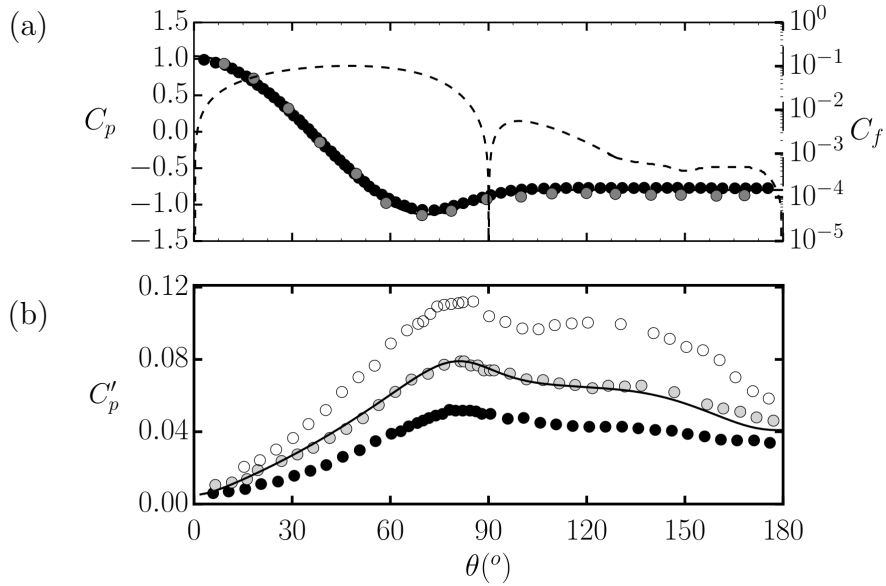
Figure 2.2: (a) Mean pressure C_p (left axis, solid) and skin friction C_f (right axis, dashed) coefficients distributions on the cylinder surface. Also shown are experimental distributions of C_p by [5] (black circles: $Re = 1500$, aspect ratio 50) and [6] (dark gray circles: $Re = 3000$). (b) Rms fluctuation of the pressure coefficient C_p'. Circles indicate experimental results by [7] at $Re = 1500$ (black), 4400 (light gray) and 5000 (white).

and reaches a minimum at $\theta \simeq 70.7°$. Here recompression starts and separation occurs shortly after at $\theta_{\mathrm{sep}} = 90.0°$, as indicated by the null mean friction coefficient $C_f = 2\tau_{\mathrm{w}}/(\rho U_\infty)$ (dashed line; τ_{w} is the wall shear stress). Beyond the mean separation point, C_p keeps increasing but quickly saturates at cylinder base value $C_{p_b} = -0.80$, such that the distribution becomes flat. Meanwhile, C_f quickly recovers beyond separation except that friction acts in the upstream direction, and then decreases non-monotonically down to null at the base of the cylinder. The C_p distribution compares favourably with experiments. Numerical results closely follow [5], measured at $Re = 1500$, while the boundary layer remains attached. The computed flat C_p distribution in the detached region falls precisely in between experiments at $Re = 1500$ (black circles, [5]) and $Re = 3000$ (dark gray circles, [6]). The higher values reported at $Re = 3900$ obey the known increasing trend of $-C_{p_b}$ beyond $Re \gtrsim 2000$ [5, 83]. The rms fluctuation of the pressure coefficient C_p' is shown in figure 2.2b. Fluctuations are almost imperceptible at the stagnation point and rise steadily along the front surface of the cylinder. They peak at $\theta \simeq 85$, just ahead of the boundary layer separation point. Beyond this point, they remain fairly high although a slight decreasing trend is observed as the cylinder base is approached. Comparison with ex-

18

periments by [7] are fair. The functional shape is closely mimicked by our numerical results and quantitative comparison places our $Re = 2000$ results in between experimental results at $Re = 1500$ (black circles) and $Re = 5000$ (empty circles). Very close agreement is achieved with experiments at $Re = 4400$ (light gray circles) but whether this is a result of experimental or numerical inaccuracies or reveals actual physics consisting of a C'_p plateau in the range $Re \in [2000 - 4400]$ is a question that cannot be elucidated from existing data.

The separation point, at $\theta_{sep} = 90.0$, is slightly retarded with respect to numerical simulations at $Re = 3900$ reported in the literature (see table 2.1). The only experimental attempt at measuring it produced a value $\theta_{sep} = 85 \pm 2$ at $Re = 3900$, while no numerical or experimental study has ever reported it for $Re = 2000$ to the authors knowledge.

2.3.2 Near-wake topology and statistics

The near-wake mean velocity field $\bar{\mathbf{u}}(\mathbf{r}_2)$ consists in a closed recirculation bubble, as illustrated by the mean flow-field streamlines in figure 2.3(a).

Within the enclosed recirculation bubble, delimited at the rear by a stagnation point, a symmetric vortex pair is clearly discernible. The streamlines distribution compares favourably with PIV measurements by figure 2.4(a) for a steady cylinder at $Re = 2150$, as also do the time-averaged velocity magnitude contours. The high cross-stream gradients of velocity magnitude along the top and bottom boundaries of the recirculation bubble indicate the presence of strong shear layers. The statistical symmetry with respect to the wake centreline is clear, which constitutes a good indicator that the data samples are sufficiently large.

Contour plots of second order flow statistics are shown in figure 2.3. The normal-streamwise ($\langle u'u' \rangle$, figure 2.3a) and streamwise-cross-stream Reynolds stresses ($\langle u'v' \rangle$, figure 2.3c) have symmetric and anti-symmetric extrema, respectively, away from the wake centre-line. While $\langle u'u' \rangle_{max}$ occurs at the rear part but still within the recirculation bubble, $\langle v'v' \rangle_{min}$ falls right behind the bubble closure. Both Reynolds stresses peak right in the vortex formation region and their contours extend upstream along the shear layers separated from either side of the cylinder. The maximum cross-stream normal Reynolds stress ($\langle v'v' \rangle$, figure 2.3b) occurs on the wake centre-line just beyond the downstream boundary of the recirculation bubble. Qualitative agreement with PIV measurements by figure 2.4 is fair. Statistical symmetry of Reynolds stress distribution is also accomplished. The maximum spanwise normal Reynolds stress ($\langle w'w' \rangle$, not shown) occurs also on the wake centre-line.
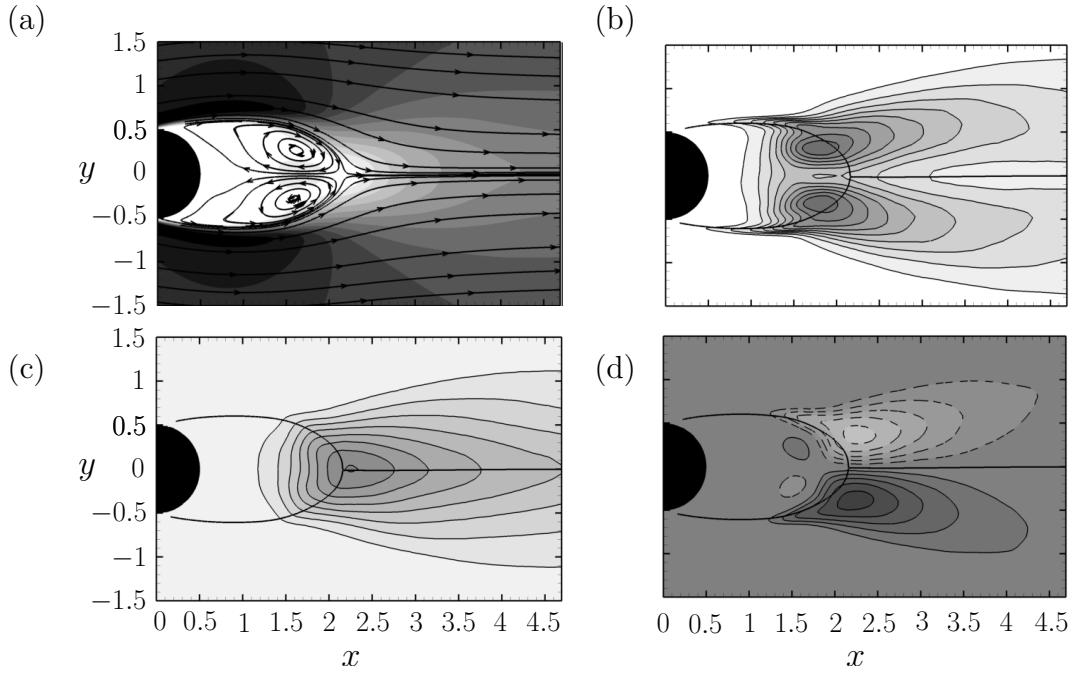
Figure 2.3: Contour plots of near-wake Reynolds stresses. a) contour plots of velocity magnitude $|\mathbf{u}| \in [\mathbf{0}, \mathbf{1.5}]$, b) $\langle u'u' \rangle \in [0.0, 0.32]$ in steps $\Delta \langle u'u' \rangle = 0.02$, (c) $\langle v'v' \rangle \in [0.0, 0.85]$, $\Delta \langle v'v' \rangle = 0.05$, and (d) $\langle u'v' \rangle \in [-0.2, 0.2]$, $\Delta \langle u'v' \rangle = 0.02$. Solid (dotted) lines correspond to positive (negative) contours. The thick black line delimits the recirculation bubble.
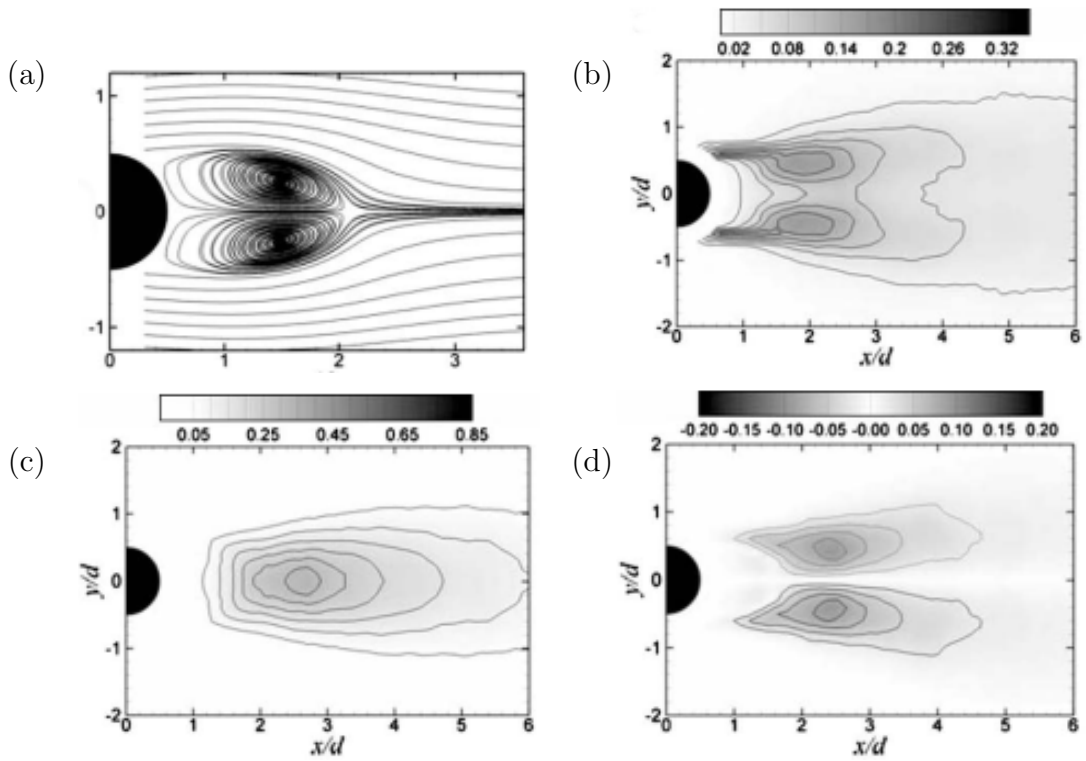
Figure 2.4: Contour plots of near-wake Reynolds stresses [8]. (a) streamlines, b) $\langle u'u' \rangle$, (c) $\langle v'v' \rangle$, and (d) $\langle u'v' \rangle$.

Table 2.3 reports extrema and streamwise location of near-wake flow field statistics along the wake centre-line, corresponding to current simulations and several experimental and numerical published results.

Cases 1 and 2, corresponding to rather short spanwise domains, feature rather small maximum velocity defect $(1 - \bar{u}_{\min})$ along the wake centre-line at a location relatively close to the cylinder base, comparable to that reported in the literature at higher Reynolds numbers of $Re \simeq 3900 \sim 4000$ [9, 11, 73, 66]. Cases 3 and 4 have instead $x_{\bar{u}}$ at locations perfectly compatible with experiments at close-by Reynolds numbers [9], although $|\bar{u}_{\min}|$ seems to be a little low. Centreline streamwise normal Reynolds stresses ($\langle u'u' \rangle$) show the expected double-peak distribution, with the first peak location and height in excellent agreement with experiments [9, 10]. The location of the second peak is also within reasonable distance of experimental results, but the height appears slightly low. The same occurs with the single-peak location and value of cross-flow ($\langle v'v' \rangle$) and spanwise ($\langle w'w' \rangle$) normal Reynolds stresses. The location is correctly predicted but the peak height is somewhat off.

Absolute in-plane peak values for $\langle u'u' \rangle$, $\langle v'v' \rangle$ and $\langle u'v' \rangle$, reported in table 2.4 are in reasonably good agreement with experiments by [12, 8].

Figure 2.5a shows the mean streamwise velocity distribution along the wake centre-line $\bar{u}(x, 0)$. Starting from rest at the cylinder base (corresponding to $x = x_b = 0.5$), $\bar{u}$ initially decreases into negative, reaches a minimum at about $x \sim 1.5$, then quickly recovers in the near-wake leaving a velocity deficit of around $1 - \bar{u}(x, 0) \sim 0.3$ that is very slowly further recovered in the mid- and far-wakes. The region where $\bar{u}(x, 0) < 0$ delimits the streamwise extent of the mean recirculation bubble, such that the recirculation bubble length L_r is obtained from $\bar{u}(x_b + L_r, 0) = 0$. This is not to be confused with wake formation length, defined as $L_f \equiv \mathrm{argmax}_x[\langle u'u' \rangle(x, 0)] - x_b$. Our numerical results (case 3) follow a trend that is fully compatible with experiments by [9], except that their minima seem to reach fairly lower values (see table 2.3). The location of the minimum for our $Re = 2000$ computation occurs precisely within the range set by the experiments at $Re = 1500$ and 3000. The experiment by [10] at $Re = 2150$, instead, features minima very close to our numerical results, although the data displays significant scatter and the velocity defect recovery appears unusually slow. It must be bore in mind that preturbulence levels were particularly high in these experiments. The experiment by [11] at $Re = 3900$ shows also minimum $\bar{u}(x, 0)$ and recovery rate similar to those in our numerics, while at the same time the minimum is located halfway between the minima of [9] for $Re = 3000$ and 5000.

Table 2.3 (rotated)

Author [Ref]	Case	Re	$\bar{u}_{min}$	$x_{\bar{u}}$	$\langle u'u'\rangle_{max}$	$x_{\langle u'u'\rangle}$	$\langle v'v'\rangle_{max}$	$x_{\langle v'v'\rangle}$	$\langle u'v'\rangle_{max}$	$x_{\langle u'v'\rangle}$	$\langle w'w'\rangle_{max}$	$x_{\langle w'w'\rangle}$
Present results:	case 1	2000	-0.242	1.520	(0.084)/0.108	(1.466)/2.016	0.392	2.267	-0.106	2.112	0.081	1.832
	case 2		-0.266	1.580	(0.083)/0.108	(1.466)/2.027	0.401	2.245	0.108	2.146	0.083	1.867
	case 3		-0.318	1.672	0.082/0.082	1.523/2.027	0.409	2.187	0.1059	2.269	0.085	1.764
	case 4		-0.302	1.718	0.086/0.087	1.504/2.004	0.373	2.245	0.111	2.215	0.093	1.764
Norberg [9]		1500	-0.4	1.75	0.09/0.1024	1.51/2.23					0.1521	1.61
		3000	-0.44	1.65	0.1089/0.1156	1.45/2.09					0.1296	2.08
		5000	-0.45	1.42	0.1225/0.1296	1.23/1.83					0.1521	1.86
		8000	-0.35	1.17	(0.1369)/0.2025	(1.02)/1.62					0.1521	1.41
		10000	-0.38	1.04	(0.1369)/0.1849	(0.96)/1.50						
Konstantinidis et al. [10]		1550			0.1089	2.1						
		2150			0.1024	2.1						
		2750			0.0961	2.1						
		7450			0.1225	1.5						
Parnaudeau et al. [11]		3900	-0.34	1.59			0.2809	2.1				
Lourenco and Shih [59]		3900	-0.24	0.72			0.2916	2.1				
Beaudan and Moin [62]		3900	-0.33	1.00			0.3136	2.1				
Kravchenko and Moin [66] $N_z = 48^F$		3900	-0.37	1.4-1.5	0.087	1.372	0.4761	1.5				

Table 2.3: Peak values of flow field statistics along wake centreline. Double-valued streamwise normal Reynolds stress columns ($\langle u'u'\rangle_{max}$ and $x_{\langle u'u'\rangle}$) denote double-peak or inflection plus peak distribution. Inflection points are given in parentheses.

Table 2.4 (rotated)

Author [Ref]	Case	Re	$\bar{u}_{min}$	$x_{\bar{u}}$	$\langle u'u'\rangle_{max}$	$x_{\langle u'u'\rangle}$	$\langle v'v'\rangle_{max}$	$x_{\langle v'v'\rangle}$	$\langle u'v'\rangle_{max}$	$x_{\langle u'v'\rangle}$	$\langle w'w'\rangle_{max}$	$x_{\langle w'w'\rangle}$
Present results:	case 1	2000			0.211	1.691	0.392	2.267	-0.106	2.112	0.081	1.832
	case 2				0.206	1.751	0.401	2.245	0.108	2.146	0.083	1.867
	case 3				0.180	1.736	0.409	2.187	0.1059	2.269	0.085	1.764
	case 4				0.177	1.803	0.373	2.245	0.111	2.215	0.093	1.764
Konstantinidis et al. [12]		2160			0.15		0.32		0.09			
Konstantinidis and Balabani [8]		2150			0.16		0.33		0.09		0.09	
Dong et al. [73]					0.114	??			0.11	2.05		
Parnaudeau et al. [11]	PIV	4000	-0.252	1.5	0.2025	1.55			0.14	1.90		
	DNS	3900	-0.291	1.35	0.1806	1.72						
Lehmkuhl et al. [68]	Mean	3900	-0.261	1.396	0.237	1.576	0.468	2.00	-0.125	1.941	0.085	1.764
	L	3900	-0.323	1.590	0.223	1.723	0.441	2.105	-0.126	2.107		
	H	3900	-0.233	1.334	0.270	1.489	0.520	1.922	-0.136	1.941		

Table 2.4: Peak values of off-centreline near-wake flow field statistics.
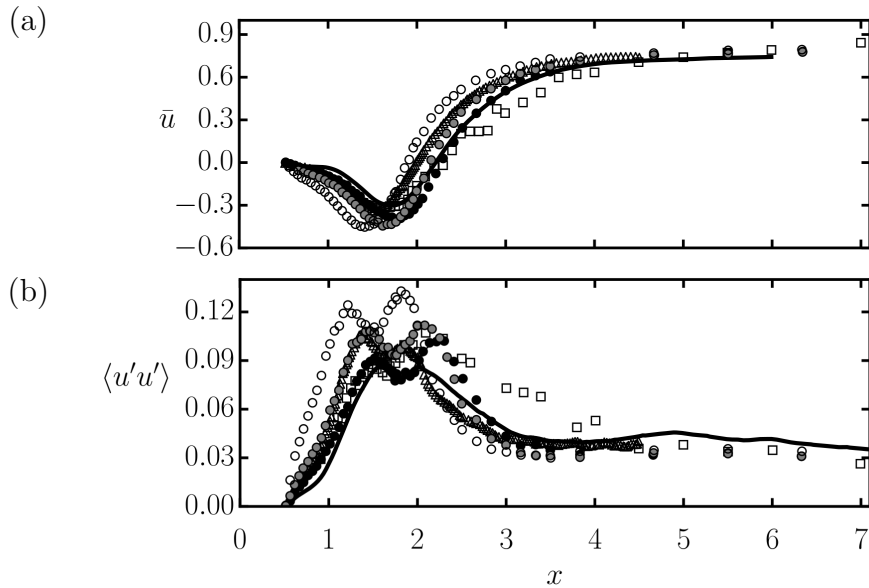
Figure 2.5: Recirculating region characteristics along the wake center-line: (a) mean streamwise velocity ($\bar{u}$) profile and (b) Reynolds streamwise normal stress ($\langle u'u' \rangle$) profile along the wake center-line. Shown are case 3 (solid line); experiments by [9] (circles, full black: $Re = 1500$, dark gray: $Re = 3000$, empty: $Re = 5000$), [10] (squares: 2150) and [11] (triangles: $Re = 3900$).

Comparison of the streamwise distribution of the streamwise velocity fluctuation autocorrelation (streamwise normal Reynolds stress) $\langle u'u' \rangle (x, 0)$ along the wake centre-line, shown in figure 2.5b, is somewhat less straightforward. While [9] reports two-peak distributions, typical of U-type wake states, that shift to lower x and higher maxima as Re is increased, [10] presents the inflection plus peak distribution that is characteristic of V-type states. The transformation of $\langle u'u' \rangle (x, 0)$ double peak distribution to inflection plus peak distribution points to the potential transition of wake towards the fully developed state through the shear layer turbulent-transition mechanism within the wake formation region. The recovery tails of the latter are also longer, possibly due to high preturbulence levels. The distal peak in the double-peak distributions of [9] is higher than the proximal peak, the dissymmetry being larger at the lowest $Re = 1500$. [11] also observed a double-peak distribution at $Re = 3900$, but the first peak rises slightly above the second in this case. The $\langle u'u' \rangle (x, 0)$ distribution in our numerical simulations on the two largest spanwise domains employed (cases 3 and 4) seem closer to [11] than [9] or [10], even though the latter explore Reynolds numbers closer to ours. When shorter spanwise domains are used, however, the distributions tend to the inflection plus peak characteristic shape. This is in overt contradiction with prior observations that the U-type state is favoured by

23

smaller spanwise domains. The issue remains unexplained.

The agreement with experiments is fair in the mid-wake and beyond, as cross-stream profiles of velocity components and Reynolds stresses at various locations $x \geq 3$ confirm (Not shown). Computationally obtained profiles overlap reasonably with experimentally measured [61, 12] and numerically computed [62, 65, 77, 71] distributions.

The categorization of the near-wake state into U- or V-type is based on the cross-stream profile of streamwise velocity at a precise streamwise location: $\bar{u}(1, y)$. As already stated in §4.1, every shape ranging from a clear-cut U to a sharp V has been reported in the literature. Figure 2.5 points at a gradual evolution of wake statistics as Re is increased, but at the same time unveils high sensitivity to experimental conditions, such as free-stream turbulence level which has a significant impact on the shear layer instability due to its convective nature [21]. While the size of the recirculation bubble in the near wake seems to evolve smoothly with Re for a given experimental setup, different experiments report dissimilar bubble sizes at the same exact Re, such that comparing cross-stream velocity distributions at a fixed location is at the very least deceptive. The effect of experimental conditions or numerical details can, to a great extent, be accounted for with an offset in Re. Comparison at a location defined in relative terms appears thus as a much sounder approach. Results compared in this way cannot be expected to match exactly, since not only the size but also the topology of the recirculation bubble evolves with Re. Accordingly, the transformation from one experiment and Reynolds number to another can only partially be explained in terms of a mere streamwise scaling or shift. We choose here to scale the x coordinate to align the location of the minimum of $\bar{u}$.

Figure 2.6 shows cross-stream velocity profiles of streamwise ($\bar{u}$) and cross-stream ($\bar{v}$) velocities at $x = 1, 1.5, 2$ for [9, 12] and close-by locations $x = 1.06, 1.54, 2.02$ for [11]. Statistically averaged profiles are expected to be reflection-symmetric with respect to the wake centre-line: $[\bar{u}, \bar{v}](x, y) = [\bar{u}, -\bar{v}](x, -y)$. Failure to preserve this symmetry would indicate lack of symmetry in the experiment (or in the measurement probe locations) or, alternatively, poorly converged statistics due to insufficient data. In this sense, the degree to which the symmetry is accomplished acts as a metric for the quality of the results. Although the degree of asymmetry in the raw simulation data was already small, we have chosen here to symmetrise numerically obtained profiles as a means of doubling the data sample size. The cross-stream profiles of streamwise velocity $\bar{u}$ evolve from a U shape very close to the cylinder base ($x \simeq 1$) towards a V shape as we move backward within the near-wake ($x \simeq 2$). This alone
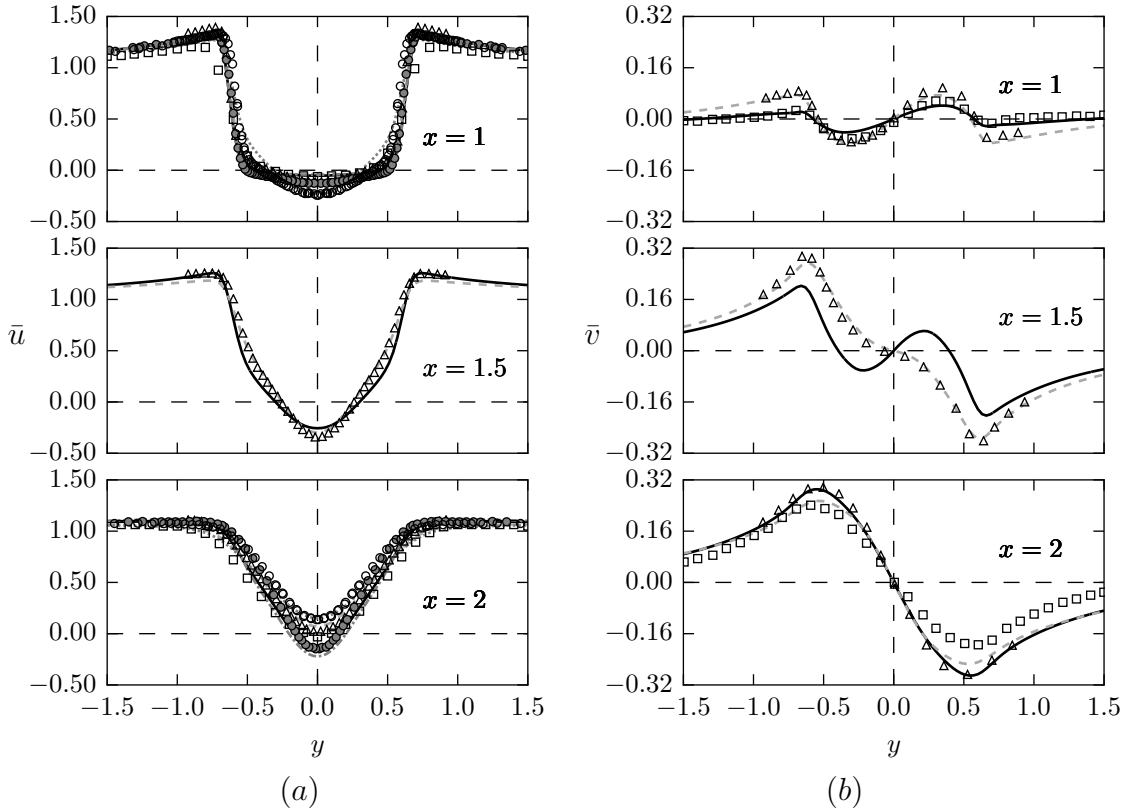
Figure 2.6: Cross-stream profiles of mean (a) streamwise $\bar{u}$ and (b) cross-stream $\bar{v}$ velocities in the near wake. Sampling locations are $x = 1$ (top), $x = 1.5$ (middle) and $x = 2$ (bottom). Shown are case 3 (solid line); experimental results by [12] (squares, $Re = 2160$), [9] (circles, dark gray: $Re = 3000, 3500$; open circles: $Re = 5000$), and [11] (triangles, $Re = 3900$, at close-by locations $x = 1.06, 1.54$ and 2.02); numerical results corrected for [9] (dash-dotted gray, $Re = 3000, 3500$; dotted gray $Re = 5000$) and for [11] (dashed gray).

illustrates how U- or V-shaped profiles can be obtained at will by adequately shifting the sampling location. Wakes that are topologically identical but have slightly different recirculation bubble lengths will produce very different results if the same location is chosen for comparison. As a matter of fact, our raw data features slightly flatter profiles at $x = 1$ and $x = 1.5$, and somewhat lower velocities at $x = 2$ when compared with [11]. When sampling locations are corrected for recirculation bubble size, the agreement is remarkable in spite of the significant disparity in Reynolds number ($Re = 2000$ here against $Re = 3900$ for the experimental data). Remaining discrepancies can be safely ascribed to this fact and also to mild experimental inaccuracies, as evidenced by a slight asymmetry in the profiles. Something similar occurs when analyzing cross-stream velocity profiles $\bar{v}$ in figure 2.6b. The significant deviations observed at $x = 1$ and 1.5, with much flatter profiles, are fully resolved upon
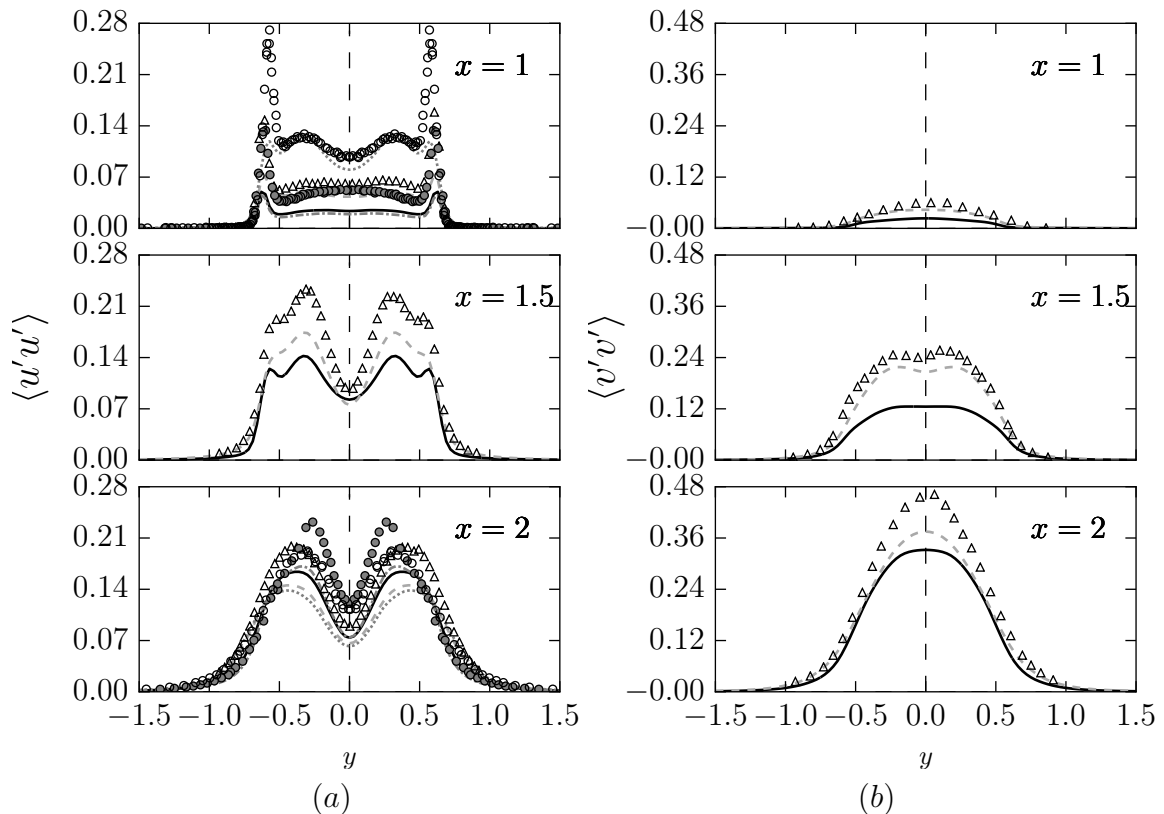
Figure 2.7: Cross-stream profiles of normal Reynolds stresses (second order moments) in the near wake. (a) Streamwise $\langle u'u' \rangle$ and (b) cross-stream $\langle v'v' \rangle$ velocity fluctuation self-correlations. Styles and symbols as in figure 2.6.

correction. At $x = 2$ the agreement was already good prior to correction and scaling weakens the agreement. The different wake topologies are to be held responsible for this.

Taking [9] as a baseline for comparison, bubble length correction of simulation results yields fairly good recovery of $\bar{u}$ profiles at both $Re = 3000$ and 5000, while no experimental data is available for $\bar{v}$. Finally, the numerical bubble size is sufficiently close to that obtained at $Re = 2160$ by [12] so that the correction to be applied is almost imperceptible. The agreement is fair at all locations for $\bar{u}$ and all but $x = 2$ for $\bar{v}$, where the experiments produced a slightly flatter profile than observed in the numerics.

Cross-stream profiles of second order moments, *i.e.* Reynolds stresses, are shown in figures 2.7 and 2.8. Streamwise velocity fluctuation self-correlations $\langle u'u' \rangle$ display the double-peak shape (with nearly fluctuation-free wake core) at $x = 1$ that is characteristic of the U-type wake state. Two distinct phenomena are responsible for these peaks, which are located on the top and bottom boundaries of the recirculation bubble. On the one hand, the shear layers resulting from boundary layer detachment at either side of the cylinder flap synchronously due to the von Kármán instability and the associated shedding of alternate counter-rotating vortices. On the other, these same shear layers are subject to turbulent transition, with the ensuing occurrence of

26
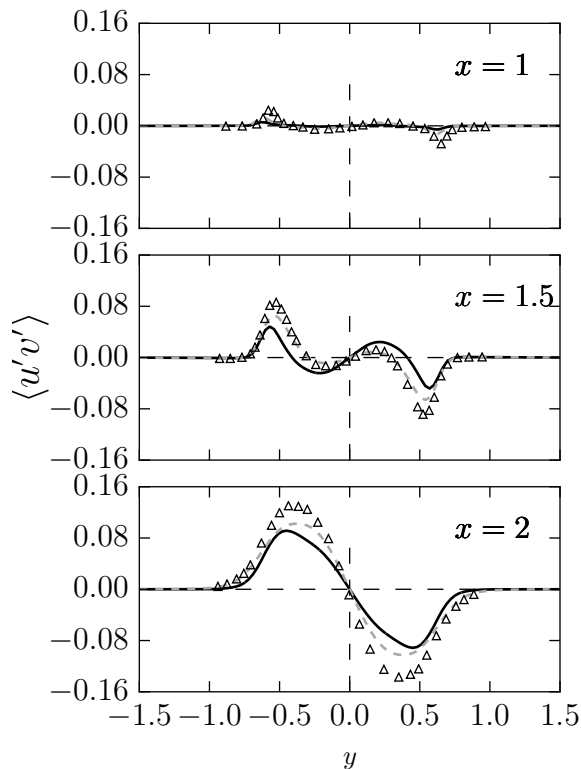
Figure 2.8: Cross-stream profile of shear Reynolds stresses or streamwise-cross-stream velocity fluctuations cross-correlations $\langle u'v' \rangle$. Styles and symbols as in figure 2.6.

turbulent fluctuations. As we progress downstream within the near-wake, the amplitude increase of the shear layer flapping results in the diffusion of Reynolds stresses, such that the peaks broaden and drift towards the wake centre-line as fluctuations gradually penetrate the recirculation bubble core. The $\langle u'u' \rangle$ profile shape compares favourably with experiments by [11], but the levels are significantly lower for the numerical data, particularly so in the very near-wake. Correction for recirculation bubble size acts in the right direction by lifting the plateau around wake centre-line to comparable levels, but peak values remain low. Contrasting with experimental data by [9] at $Re = 3000$ ($x = 1$) and $Re = 3500$ ($x = 2$) also qualitatively captures the right functional shape but quantitatively falls short of experimental values. In this case, correction does not improve the situation, as the minimum of $\bar{u}$ for numerics and experiments is already aligned and the scaling factor is very close to unity. Nonetheless, while it is not surprising that turbulent fluctuation levels are higher at the higher Re at which the experiments were done, the outline of the profiles is properly captured by the numerics. The exact same reasoning applies to cross-stream velocity self-correlations (figure 2.7b) and streamwise-cross-stream cross-correlations (depicted in figure 2.8), for which only the experimental data of [11] is available. Once again qualitative agreement is excellent, while quantitative match is improved by correction but remains elusive. There is a reasonable explanation to the level mismatch in second order statistics. Peak values of Reynolds stresses occur within the shear

layers developing at either side of the cylinder and turbulence levels in this region are naturally dependent on shear layer thickness, which in turn scales with Reynolds number. Quantitative agreement is therefore not to be expected.

2.4 Discussion

2.4.1 Shear layer instability

Planar steady shear layers may be subject to the Kelvin-Helmholtz instability. In the case of the transitional flow past a cylinder, the shear layers resulting from boundary layer separation are neither planar nor steady. The Kármán instability induces a flapping motion of the wake and a secondary instability of the von Kármán street introduces a spanwise modulation that propagates upstream in the wake and reaches, to some degree, the immediate vicinity of the cylinder. Notwithstanding this, shear layer instability has been observed in the cylinder near wake. The precise critical value Re_{KH} (or Re_{SL}) for the inception of the Kelvin-Helmholtz (or shear layer) instability is largely dependent on extrinsic factors such as end boundary conditions, background disturbance intensity, preturbulence levels, etc [48]. For an experimental setup favouring parallel shedding conditions the instability might occur as early as $Re_{\mathrm{SL}} = 1200$, while oblique shedding pushes the shear layer instability to $Re_{\mathrm{SL}} = 2600$. The large scatter in the values of Re_c might have been attributed to the convective nature of shear layer instability and its high sensitivity to the environmental forcing such as background noise, free-stream turbulence level and boundary conditions [21]. The instability, when present, emerges as a spatially developing train of small scale vortices characterised by velocity fluctuations of a frequency that is substantially higher than that of Kármán vortices. Kelvin-Helmholtz vortices are continuously being generated early on in the shear layer and grow as they are advected downstream. When they reach the Kármán vortex formation region, a number of them accumulate, coalesce and are swallowed into the forming wake vortex. Using theoretical scaling arguments for the separating boundary layer on the cylinder walls and the ensuing shear layers to fit experimental data from several sources, [1] suggested a power law f_{SL}/f_{vK}=0.0235$Re^{0.67}$ relating the shear layer $f_{SL} \equiv f_{KH}$ and von Kármán f_{vK} shedding frequencies.

A velocity probe strategically located in the shear layer at $(x, y, z) = (0.8, 0.6, 1.25)$ clearly detects the flapping motion of the wake for most of the time, as shown by the low-frequency-low-amplitude oscillation of the cross-stream velocity v in the inset of figure 2.9.
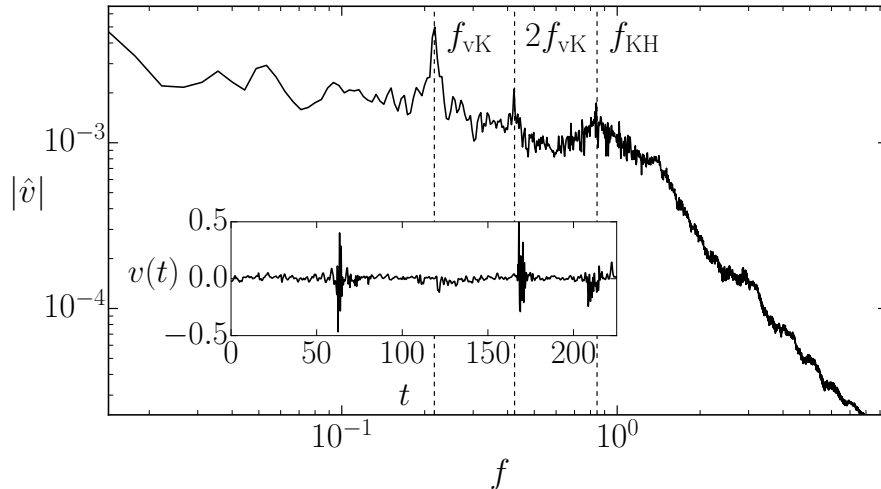
Figure 2.9: Average spectrum of the cross-flow velocity signals along a probe array located in the shear layer at $(x, y) = (0.8, 0.6)$. The inset shows one such signal for the probe at $(x, y, z) = (0.8, 0.6, 1.25)$.

The signal, however, experiences occasional sudden bursts of much higher frequency and amplitude. Averaging the individual spectra of 64 velocity signals measured for a time lapse in excess of $20 \sim 25$ vortex shedding cycles along a probe array at $(x, y) = (0.8, 0.6)$ results in the average spectrum shown in figure 2.9. Alongside the distinct vortex shedding fundamental frequency peak f_{vK} and its first harmonic, a broad-band low amplitude peak f_{SL} is discernible. This peak corresponds to the shear layer instability and, although the associated velocity fluctuations are large, its moderate amplitude results from the phenomenon occurring only occasionally. The peak is located at $f_{SL} \simeq 3.902 f_{vK}$, which falls right on top of the power law advanced by [1].

In order to suppress the von Kármán-related oscillation from the probe array readings and thus isolate the shear layer oscillation, the signals have been processed with a high-pass fifth-order Butterworth filter with cutoff frequency $f_c = 0.7$. The filtered signals are displayed as space-time diagrams in figure 2.10.

While there are no traces of the von Kármán frequency, which has been effectively filtered, occasional velocity oscillations are clearly observed as ripples that are elongated, albeit localised, in the spanwise direction. Very low amplitude ripples are perceptible here and there, but only a few grow to remarkably high amplitude. These oscillations are consistent with the passage of small spanwise vortices resulting from a Kelvin Helmholtz instability of the shear layer, but the incipient three-dimensionality of the flapping shear layer restrains their spanwise extent, which remains always well below $1D$. This does not preclude that, at higher Reynolds, shear
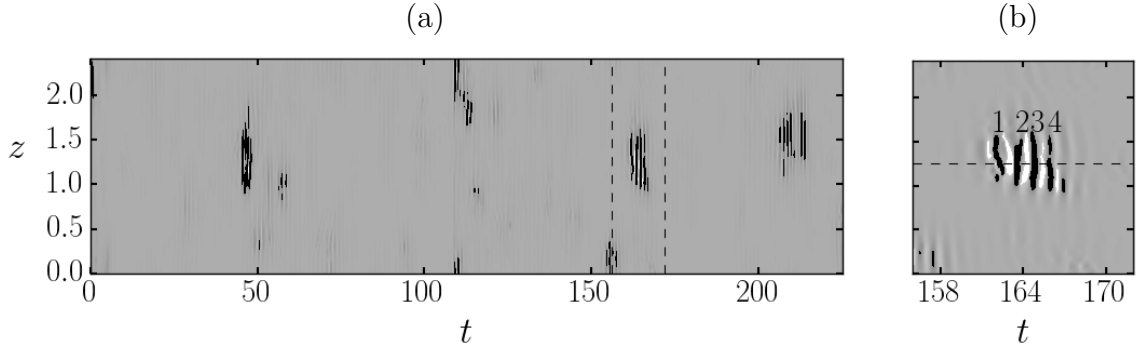
Figure 2.10: Space-time diagram of filtered crossflow velocity v at $(x, y)=(0.8, 0.6)$. (a) Full time series. (b) Detail of the interval $t \in [158, 172]$ (indicated with dashed lines in panel (a)) showing the passage of Kelvin-Helmholtz vortices. The horizontal and vertical dashed lines indicate the (z, t) coordinates drawn in figure 2.11. Labels 1, 2, 3 and 4 indicate stripes that correspond to consecutive shear-layer vortices traversing the location of the probe array.
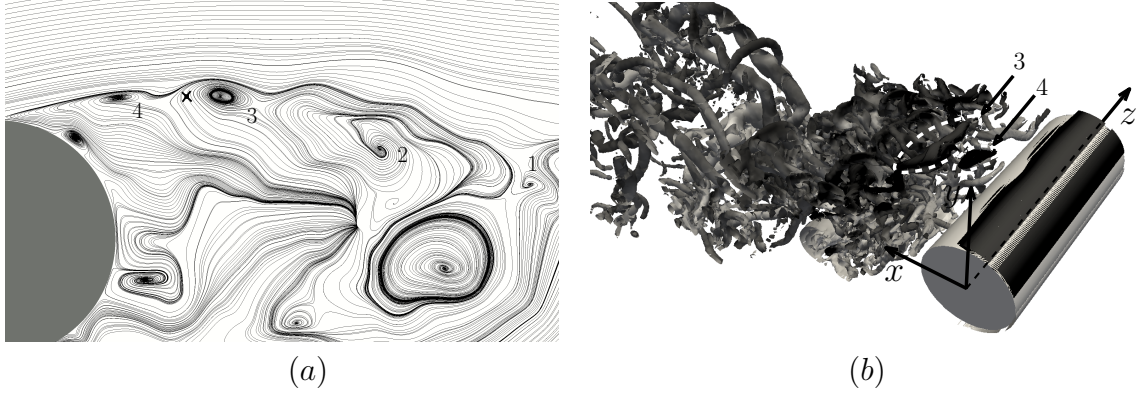
Figure 2.11: Kelvin-Helmholtz instability in the shear-layer. (a) Streamlines of the instantaneous velocity field at $z = 1.25$ and $t = 165.7$, as indicated in fig 2.10. The cross indicates the location of the probe. The labels indicate consecutive shear-layer vortices. (b) Visualization of shear-layer vortices using the Q-criterion with value 5; colouring by spanwise vorticity $\omega_z \in [-10, 10]$.

layer vortices become more elongated in the spanwise direction thus preserving better two-dimensionality, as observed by [1]. The intensification of the Kelvin-Helmholtz instability renders it perceptible further upstream on the shear layers, out of reach of the wake three-dimensionalisation that occurring downstream. The intermittency factor at the probe location, defined as the fraction of the time that high frequency oscillations are present, is $\gamma \simeq 6$, although much longer time series would be required to obtain converged values.

Figure 2.11 depicts cross-sectional streamlines at $z = 1.25$ of the instantaneous velocity field at $t = 165.7$, in the close vicinity of four consecutive shear-layer vortices duly numbered and labeled in figure 2.10. Vortices 1, 2 and 3 have already traversed the sampling probe location (cross sign), while vortex 4 is headed towards it.

In the context of global instability theory, the shear layer instability might have been absolute or convective in nature in the present computations. The shear layer instability is an absolute one and that the only reason why it appears and disappears is related to the transient nature of the shear layer, which is chaotic on account of the cylinder wake regime. To substantiate this, One way of checking this could be to freeze the flow at several time instants and then perform linear stability analyses. We might then observe that for some snapshots the shear layer is absolutely unstable and at some others perfectly stable. This would account for the intermittent nature of the instability. However, it cannot be discarded that the instability isconvectiveand that it is simply triggered from time to time by the turbulent nature of the wake and then travels downstream and disappears. To test this, local limited-time perturbations has to be applied in the upstream region of the shear layer and monitor their evolution. If this triggers an instability that stays, it is of absolute nature. If the instability grow as it is advected downstream but after passing it leaves the shear layer laminar, then it is convective.

2.4.2   Secondary instability of Kármán vortices

The secondary instability of the von-Kármán vortex street demonstrate distinct characteristics in the transitional flow regime in terms of length scales of three-dimensional structures and their spanwise coherence neglecting large scale three-dimensional effects such as vortex dislocations. In the following sections the phase at which three-dimensional structures exhibit maximum strength within the von-Kármán vortex shedding cycle is evaluated alongside the computation of spanwise lengthscale of large coherent three-dimensional structures via rigorous mathematical tool (Hilbert transform), and finally global linear stability analysis is employed to determine the least stable mode together the location at which maximum growth rate is recorded.

2.4.2.1   Temporal relationship of large coherent three-dimensional structures

The cylinder wake is three-dimensional from Reynolds numbers as low as $Re \lesssim 190$ [42] following well established secondary instabilities of von Kármán vortices [43, 37]. Here we are interested in the remnants of these instabilities at a much higher Reynolds number $Re = 2000$, for which von Kármán vortices remain the dominant structure in the wake, but are perturbed by spanwise modulation and superimposed spatiotemporal turbulent fluctuations.

In order to analyse the three-dimensional nature of the flow, we have followed [14] in decomposing the flow field in a primary (two-dimensional, $\mathbf{u}_2(\mathbf{r}_2; t) = \bar{\mathbf{u}}(\mathbf{r}_2) + \mathbf{u}_2'(\mathbf{r}_2; t)$) and a secondary (three-dimensional, $\mathbf{u}_3(\mathbf{r}; t)$) components. In the restricted spanwise extent of the computational domains employed there is no room for the development of oblique shedding or vortex dislocation, such that this decomposition does indeed properly separate all three-dimensional effects from primary vortex shedding.

Figure 2.12a shows the space-time diagram of streamwise velocity u for a probe array located beyond the vortex formation region at $(x, y) = (3, 0.5)$. A vertical-
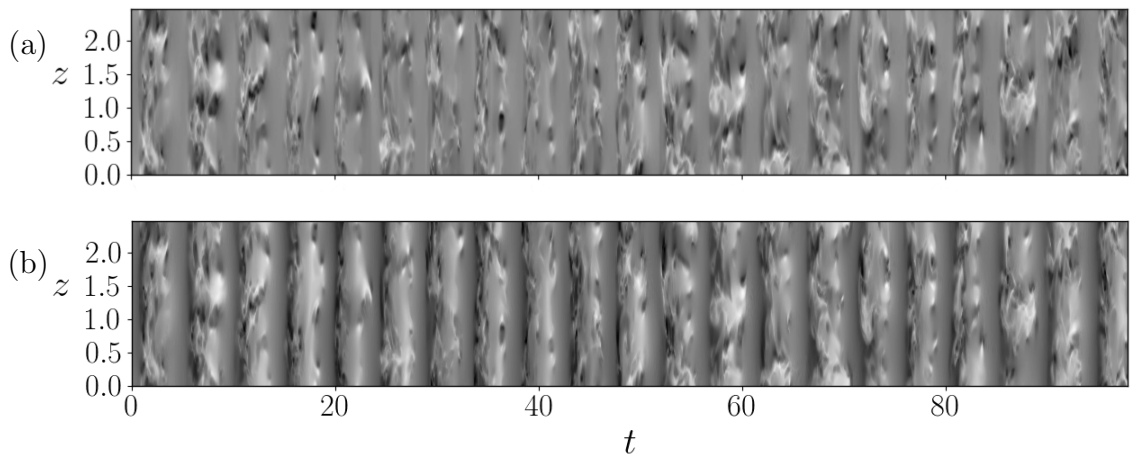
Figure 2.12: Space-time diagrams of streamwise velocity at $(x, y) = (3, 0.5)$ for (a) the total (primary and secondary combined) $u = u_2 + u_3$, and (b) secondary flow u_3.

banded pattern, associated with vortex shedding, is clearly distinguishable. The effect of subtracting the primary flow from the total flow, yielding the secondary flow in isolation, is shown in figure 2.12b. It is clear from the alternate homogeneous and inhomogeneous stripes that three-dimensionality is concentrated at certain phases along the vortex shedding cycle.

The spectra of the total, primary u_2 and r.m.s. secondary $u_3^{\mathrm{rms}} \equiv \sqrt{\langle u_3^2 \rangle_z}$ streamwise velocity signals are shown in figure 2.13a. As expected, the primary signal has a clear peak at the Strouhal frequency and two higher harmonics are also discernible. The secondary signal is somewhat flatter, but protrusions at the Strouhal frequency and a couple of harmonics are still visible, which indicates that the signals are coupled. The cross-spectral-density S_{23} of the primary and secondary signals is shown in figure 2.13 to analyse the cross-correlation or coherence between the signals. There is a clear peak of the cross-spectral-density modulus ($A_{23} \equiv |S_{23}|$, top panel) at precisely the Kármán frequency, indicating that the energy contents at this frequency of either signal is correlated. The cross-spectral-density phase ($\varphi_{23} \equiv \arg(S_{23})$) reveals
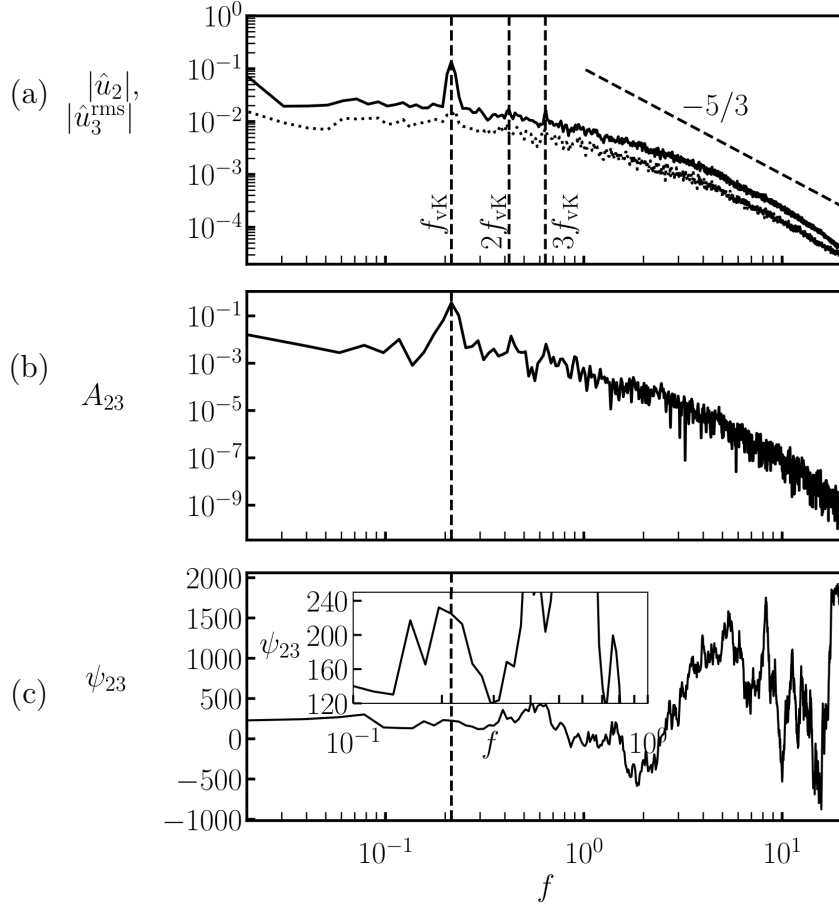
Figure 2.13: Spectra of the total (u, black), primary (u_2 dark gray) and r.m.s. secondary (u_3^{rms}, light gray) flow components at the streamwise velocity signal at $(x, y) = (3, 0.5)$. (b) Cross-spectral-density S_{23} of the primary u_2 and secondary u_3^{rms} signals pair (top: cross-modulus $A_{23} \equiv |S_{23}|$, bottom: cross-phase $\varphi_{23} = \arg(S_{23})$).

an associated phase lag $\varphi_{23}(f_{\mathrm{vK}}) \simeq 225°$. Since the primary signal peaks upon the crossing of the Kármán vortex through the sampling location, the detected phase lag implies that three-dimensionality is maximum in the trailing portion of the braid region that connects counter-rotating consecutive vortices.

Figure 2.14 illustrates the location of maximum three-dimensionality with two snapshots of the spanwise vorticity field that are apart by exactly $\varphi_{23}(f_{\mathrm{vK}})$ along one vortex shedding cycle. The first one corresponds to a maximum of the primary signal as recorded at the sampling location (cross), which is being traversed by a Kármán vortex. The second one, taken $\varphi_{23}(f_{\mathrm{vK}})$ later, shows that the sampling location is right at the braid region in between consecutive vortices. This is consistent with the short-wavelength mode B observed in the cylinder wake at much lower Reynolds numbers, as the instability leading to it is known to nucleate at the braid shear layers [84, 37],
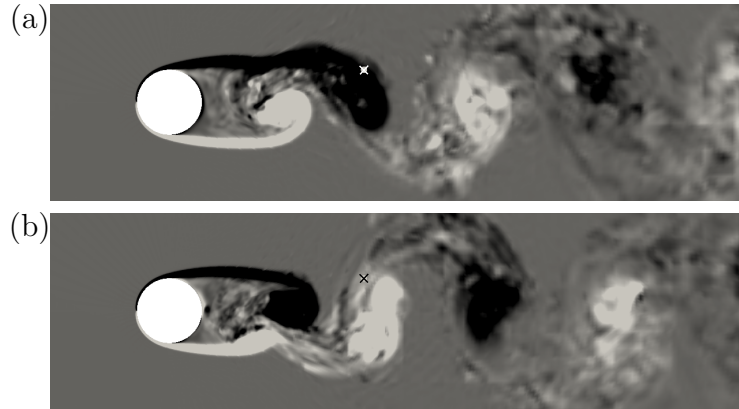
Figure 2.14: Instantaneous spanwise vorticity ω_z field snapshots at (a) a maximum of the primary signal u_2 as measured by the sampling probe at $(x,y) = (3, 0.5)$ and (b) a phase $\varphi_{23}(f_{\mathrm{vK}}) = 225°$ later corresponding to a maximum of the secondary signal u_3^{rms}.

while Mode A results from the instability of the vortex core regions. Strong counter-rotating streamwise vortex pairs can be detected in the braid regions every now and then, but the spanwise periodic pattern of mode B has long been disrupted, such that vortices appear in isolation or with irregular spacing at best. The streamwise coherence of mode B streamwise vortices at onset, which accounted for a characteristic symmetry from one braid to the next of opposite sign, is lost once turbulence sets in. Two-dimensional (time and z-coordinate) cross-correlation of u_3 signals taken along probe arrays at $(x, y) = (3, 0.5)$ and $(x, y) = (3, -0.5)$ fail to produce the clear peak one would expect for space-time drifts $(\zeta, \tau) = (0, \pi/f_{\mathrm{vK}})$ if mode B symmetry was preserved. The effect of turbulent transition is that of decorrelating any two signals separated by relatively short time or streamwise distance.

2.4.2.2 Spanwise length-scale of large coherent three-dimensional structures

Quantification of the spanwise length-scale of the large coherent three-dimensional structures that are present in the wake requires monitorisation of some quantity along spanwise lines. Particularly useful are signals that cancel out exactly for two-dimensional vortex-shedding, as their mere deviation from zero is a sign of three-dimensionality. Fourier spectral differentiation has been employed along spanwise probe arrays to compute $\tilde{\omega}_y = \dfrac{\partial u}{\partial z}$, as an indicator of cross-stream vorticity. The usual approach of computing spanwise self-correlation or performing Fourier analysis works fine for spanwise(-pseudo)-periodic flow structures but fails whenever the structures appear in isolation or show some localisation features. The reason is that self-correlation and Fourier transforms act globally on the signal and provide global

$$ (a) \qquad\qquad\qquad\qquad (b) $$
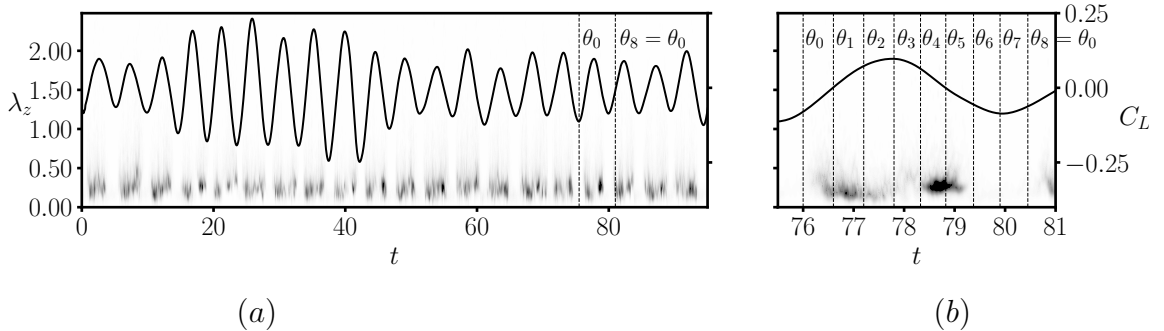
Figure 2.15: Time evolution of the lift coefficient C_L (right axis) and PDF of the instantaneous spanwise wavelength λ_z distribution at $(x, y) = (3, 0.5)$, scaled by the mean instantaneous envelope $\langle A_\omega \rangle_z$ (left axis). (a) Full time-series. (b) Detail for $t \in [75, 82]$. The vertical dashed lines indicate the time instants for 8 equispaced C_L signal phases $\theta_i = 2\pi i/8$ ($i \in [0, 7]$).

information, such that structure spacing rather than size can be detected. A powerful tool for analysing the local spectral features of a signal is the Hilbert transform. Spectrograms, wavelet transforms or the Hilbert-Huang transform are alternative means, but the simplicity and versatility of the Hilbert transform makes it more suitable for the analysis of spanwise length-scales in the cylinder wake [13].

The $\tilde{\omega}_y(z, t)$ signal is turned into an analytical signal using the Hilbert transform in the spanwise coordinate

$$ \omega(z, t) \equiv \tilde{\omega}_y^a(z, t) = \tilde{\omega}_y(z, t) + \mathrm{i}\mathcal{H}_{\tilde{\omega}_y}(z, t) = A_\omega(z, t)\mathrm{e}^{\mathrm{i}\varphi_\omega(z, t)} $$

The modulus $A_\omega \equiv |\omega|$ and phase $\varphi_\omega \equiv \arg(\omega)$ of the analytical signal contain information on the local amplitude (envelope) and phase, respectively, of the original signal. The instantaneous local spanwise wavelength of the signal is then recovered from

$$ \lambda_z(z, t) = \frac{2\pi}{\frac{d\varphi_\omega}{dz}} $$

The probability density function (PDF) of λ_z has been computed via normal/Gaussian kernel density estimation with a bandwidth $\Delta z = 0.04$ and scaled by the mean instantaneous envelope $\langle A_\omega \rangle_z(t)$ so as to account for the energy level contained in the most predominant three-dimensional structures.

Figure 2.15 presents the time evolution of the $\langle A_\omega \rangle_z$-scaled λ_z-PDF instantaneous distributions as processed from readings by the probe array located at $(x, y) = (3, 0.5)$. The shading denotes instantaneous probability distribution of λ_z, darker regions corresponding to the most recurrent length-scales of energetic spanwise structures. Long wavelength structures are rare, as evidenced by the predominance of white for large λ_z.

Meanwhile, shaded regions appear for relatively low λ_z in the form of time-localised spots with a certain (pseudo-)periodicity. Energetic spanwise structures occur intermittently, with characteristic frequency (that of vortex shedding) and spanwise size distribution. The C_L signal has been superimposed to the colourmap to illustrate the existing correlation between the occurrence of spanwise flow structures and the vortex shedding process. As already anticipated by the secondary flow space-time diagram of figure 2.12, three-dimensionality occurs predominantly at certain phases of the vortex-shedding cycle, which translates into precise streamwise locations along the vortex street, namely the braid regions in between opposite sign vortices.

The C_L signal has been used to uniquely define a phase along the vortex-shedding cycle. The Hilbert transform has been used again, this time to turn C_L into an analytical time signal $C_L^a(t) = C_L(t) + \mathrm{i}\mathcal{H}_{C_L}(t)$, such that the phase can be obtained as $\theta(t) \equiv \arg\left(C_L^a(t)\right)$. The right panel of figure 2.15 zooms into a full vortex-shedding cycle and indicates eight equispaced phases $\theta_i = 2\pi i/8$ ($i \in [0,7]$) along it. Four distinct stages can be clearly identified during the cycle. For around one quarter of the cycle, represented by phases θ_6 through $\theta_8 = \theta_0$, the wake has no perceptible three-dimensionality at the sampling location. Later on, three-dimensional spanwise structures of very small size start being observed at the probe array with increasing probability that peaks between phases θ_1 and θ_2. Beyond this first probability peak, the recurrence of the structures declines to some extent reaching a local minimum in between phases θ_3 and θ_4. Past this stage, spanwise structures regain presence and their probability of occurrence reaches a second peak at phase θ_5. The spanwise extent of the three-dimensional structures progressively grows as their recurrence declines from the first probability peak and bounces back toward the second peak. The most probable structures are therefore slightly larger, although still rather small, for the second peak than for the first. Beyond the second peak, three-dimensionality quickly vanishes before the cycle starts anew.

In order to substantiate the cyclic nature of the spanwise flow structures measured at a fixed (x, y)-location in the wake, phase averaging of the flow field has been undertaken. The data comprised in the interval $\theta \in [\theta_i - \pi/8, \theta_i + \pi/8]$ ($i \in [0,7]$) of all available vortex-shedding cycles has gone into averaged phase $\bar{\theta}_i$. The resulting phase-averaged $\langle A_\omega \rangle_z$-scaled PDF distributions at the off-centreline sampling location $(x, y) = (3, 0.5)$ are shown in figure 2.16. Direct time-averaging of the $\langle A_\omega \rangle_z$-scaled PDF distributions (black solid line) already detects the presence, at the sampling location, of three-dimensional structures of size distributed around $\lambda_z = 0.234$. Further, the evolution of the phase-averaged spanwise size distributions corroborates the
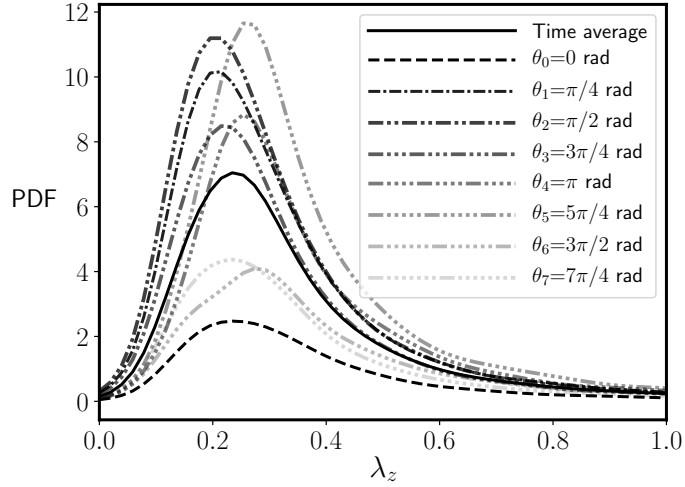
Figure 2.16: Time-averaged (solid line) and phase-averaged (dashed lines, colouring as indicated in the legend) of $\langle A_\omega \rangle_z$-averaged PDF distributions at phases $\theta_i = 2\pi i/8$. Normal/Gaussian kernel density estimation with a bandwidth $\Delta z = 0.04$ has been employed.

observations made for the particular vortex-shedding cycle of figure 2.15. Three-dimensionality is scarce at phase $\bar{\theta}_0$, but spanwise structures start appearing with quickly growing probability that peaks at $\bar{\theta}_2$ with prevailing spanwise size $\lambda_z \simeq 0.204$. Structures become less abundant and/or less energetic for phases $\bar{\theta}_3 \sim \bar{\theta}_4$ as they grow in typical size to $\lambda_z \simeq 0.219$. As the cycle progresses, spanwise structures are fast re-energised and become more recurrent until reaching a new probability peak at phase $\bar{\theta}_5$ with spanwise size distributed around $\lambda_z \simeq 0.28$. Beyond this point, ubiquity of three-dimensional structures sharply drops until becoming almost imperceptible at phase $\bar{\theta}_6$. Three-dimensionality remains insignificant for the rest of the cycle.

Spanwise-averaged flow vorticity snapshots taken at phases θ_0, θ_2 and θ_5 are shown in figure 2.17 to identify the location along the wake where three-dimensional structures occur. Phase-averaged snapshots (figure 2.17b) are shown alongside instantaneous snapshots (figure 2.17a, for the particular vortex-shedding cycle depicted in figure 2.15b) to convey the general recurrence of three-dimensionality at the same locations in the wake. The leading front of the Kármán vortex and the nearly quiescent flow field immediately downstream, (top panel, which corresponds to phase θ_0), preserve a markedly bi-dimensional character. In the downstream portion of the braid region, immediately at the vortex trailing front (mid panels, θ_2), is where the smallest highly energetic three-dimensional structures are to be identified. At the upstream part of the braid region, where it connects with the next Kármán vortex of
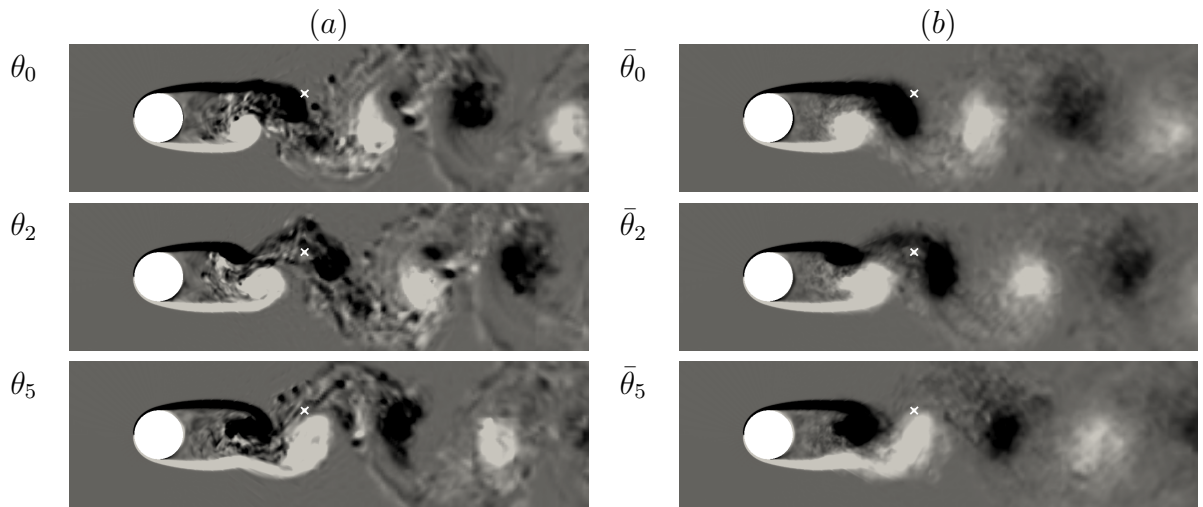
Figure 2.17: Spanwise-averaged spanwise vorticity fields at phases θ_0 (top), θ_2 (mid) and θ_5 (bottom) along the vortex-shedding cycle. Vorticity is in the range $\omega_z \in [-2, 2]$, clear for positive, dark for negative. The cross indicates the sampling location of the signals in figure 2.15. (a) Instantaneous snapshots corresponding to the vortex-shedding cycle of figure 2.15b. (b) Phase-averaged snapshots.

opposite sign (bottom panels, θ_5), high energy spanwise structures of a slightly larger spanwise extent thrive. In-between, in the mid section of the braid region, three-dimensionality appears to be somewhat weaker. As a matter of fact, this is the result of the curved nature of the braid region, such that its core sheet crosses the sampling location, at a fixed cross-stream coordinate, twice. It is natural to assume that the three-dimensional structures extend in fact along the braid region pretty much unaltered, just with a mild propensity to grow from leading to trailing region. The apparent weakening would therefore be a result of the curvature of three-dimensional structures along the braids. This scrutiny of spanwise flow structures confirms the notion, already anticipated by the analysis of the primary and secondary flows, that three-dimensionality is suppressed by the strong spanwise vorticity of Kármán vortices but thrives in the trailing braid regions at a phase 225° later, the precise phase lag that separates the most energetic spanwise structures (θ_5) from the weakest (θ_0). The inquiry into the spanwise length-scale of three-dimensionality further reveals that the structures are of rather small spanwise extent and that their size experiences a periodic evolution along the vortex street.

Figure 2.18 shows instantaneous streamwise cross-sections of cross-stream vorticity $\omega_y(3, y, z)$, containing the probe array (dashed line), at the very same times as in figure 2.17. The probe clearly registers quasi-two-dimensional flow at θ_0 (left panel), although three-dimensional structures are clearly visible at the symmetric y-location
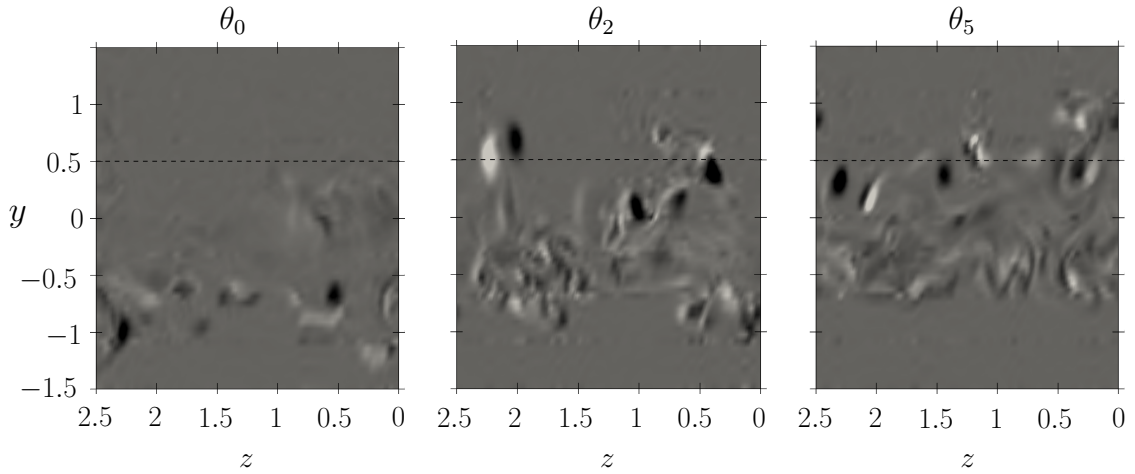
Figure 2.18: Colourmaps on a streamwise cross-section, containing the probe array, of instantaneous cross-stream vorticity $\omega_y(3, y, z)$ at phases θ_0, θ_2 and θ_5. The probe array is indicated with a dashed line.

as a lower braid is traversing the cross-section at the time. At θ_2 (centre panel), the upper braid downstream region is traversing the cross-section. In this case a couple of vortex pairs are spotted at precisely the probe-array location. Note that a Fourier transform or signal autocorrelation along the probe would have provided the spacing between the vortex pairs rather than the local size of each one of them. The Hilbert transform works locally and will in fact produce the characteristic size of every strong vortex traversing the probe array. It must be realised that the sizes given by the Hilbert transform will correspond to that of a compact vortex pair. If, for whatever reason, the vortex pair splits into two counter-rotating vortices that drift apart, the Hilbert transform will be measuring the size of the original vortex pair as though the vortices had remained packed together. We are thus measuring double the size of individual vortices, regardless of whether they appear in pairs or in isolation. At θ_5 (right panel) it is the upstream region of the braid that is traversing the cross-section. Once more, both vortex pairs and isolated vortices can indistinctly be detected at the probe array height.

At the same height but below the wake centre plane (*i.e.* the mirror image of the probe location), three-dimensionality is weaker and less structured than in the braid core, where the strongest vortical structures of clear-cut characteristic size happen to be. We surmise that it is these latter vortices that extract energy from the main shear and constitute the primal instability that then breaks down into the featureless lower-intensity turbulence that dominates the trailing region left behind by the braids in their downstream advection. The low-intensity turbulent region in the bottom half

39
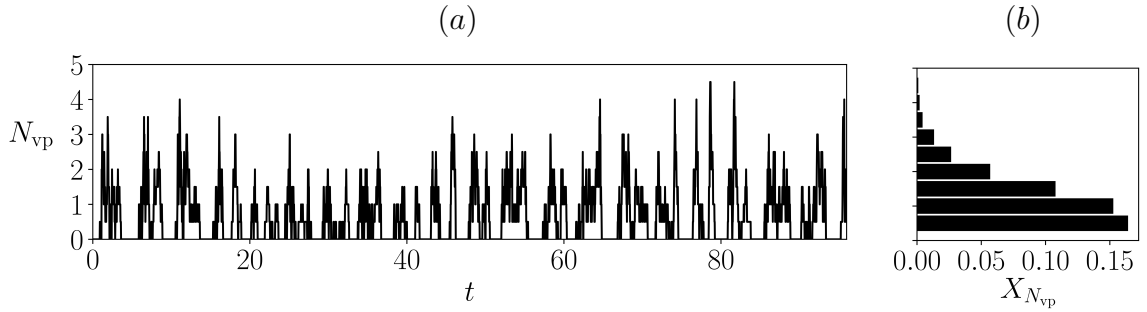
Figure 2.19: Count of vortex pairs traversing the probe array at $(3, 0.5)$. (a) Time evolution of the vortex pair count. The threshold for counting the occurrence of a vortex is $|\tilde{\omega}_y| \geq 8$. (b) Histogram of time fraction $X_{N_{\mathrm{vp}}} \equiv t_{N_{\mathrm{vp}}/T}$ of observation of N_{vp} vortex pairs. Half values result from the detection of isolated vortices.

of the θ_2 and θ_5 panels would therefore correspond to the region just cleared by a lower braid and waiting to be reached by the leading front of an oncoming Kármán vortex. A couple of final considerations regarding structure size measurement need mentioning at this point. First, if we consider vortex pairs as embedded inside an envelope, the instantaneous horizontal size of this envelope as measured at the probe array will oscillate as the vortex, which has a certain streamwise tilt due to braid slope and curvature, traverses it. From the probe, the vortex pair will be seen as either rising or descending and the correct size will only be measured when the vortex cores are at exactly the probe height. This introduces a bias in size measurement towards somewhat smaller-than-actual structures. Also, we have employed $\tilde{\omega}_y$ instead of the real vorticity ω_y for computing structure size. There is no guarantee that the sizes measured will remain the same if different signals are used. Trading some vorticity component for another or for any velocity component might produce different results. Deviations should not be enormous, but the definition of structure size is somewhat loose and can of course depend on the field used for its measurement.

In order to characterise the typical spanwise size of three-dimensional flow structures, the mode (peak) of the time-averaged $\langle A_\omega \rangle_z$-scaled λ_z-PDF distribution, rather than the mean, has been taken as the most probable wavelength $\bar{\lambda}_z$. Due to the skewness of the size distributions, the mean is not a particular good indicator of the most probable spanwise sizes. To provide a measure of distribution spread or variability, a range $[\lambda_z^{\min}, \lambda_z^{\max}]$ has been defined by picking the interval where the PDF remains above 50% of its maximum. Thus typical positive and negative deviations have been defined as $\delta_{\lambda_z}^+ = \lambda_z^{\max} - \bar{\lambda}_z$ and $\delta_{\lambda_z}^- = \bar{\lambda}_z - \lambda_z^{\min}$, respectively.

Figure 2.20 shows the evolution of the typical spanwise size of three-dimensional structures along the wake. The measurements have been taken off-centreline at $y =$

40
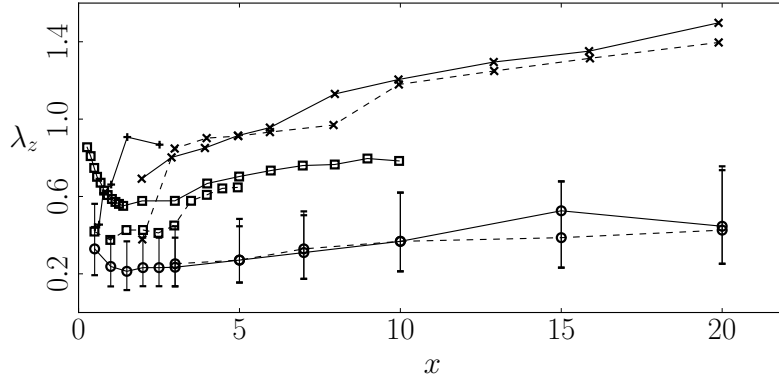
Figure 2.20: Typical spanwise size λ_z of three-dimensional structures along the wake measured off-centreline at cross-stream locations $y = 0.5$ (solid lines) and $y = 1$ (dashed lines). Shown are our numerical results (circles) along with numerical results by [13] at $Re = 3900$ (squares) and experimental results by [14] at $Re = 600$ (crosses) and [15] at $Re = 10000$ (plus signs). The error bars denote the range for which the probability remains above half the peak probability.

0.5 and $y = 1$. The trends for $y = 0.5$ observed by [13] at $Re = 3900$ using a similar analysis are recovered in the present results at $Re = 2000$, although the typical sizes were notably larger in the former study. In our case, the spanwise size of structures decreases from $\bar{\lambda}_z \simeq 0.35$ in the immediate vicinity of the cylinder along the shear layers until reaching a minimum $\bar{\lambda}_z \simeq 0.25$ at about $x \simeq 2 \sim 3$ in the vortex formation region. The size gradually recovers afterwards, asymptotically tending to $\bar{\lambda}_z \simeq 0.4$ by $x = 20$. In [13] the sizes are off by over 0.4. At $y = 1$ we observe the same trends as for $y = 0.5$ and very close values from $x \gtrsim 2.5$ on. In contrast with the observations by [13] at the larger $Re = 3900$, the sizes of the structures in the very near wake at this cross-stream location are meaningless, as three-dimensionality is barely noticeable. This can be ascribed to the lower Re employed in our simulations. Three-dimensionality (and turbulence, for that matter) seems to have a hard time diffusing upstream and cross-stream at $Re = 2000$ but not so much at $Re = 3900$. Comparison with experimental results by [14] at $Re = 600$ and [15] at $Re = 10000$ is hindered by the exceedingly different flow regimes considered and by the methodology employed, which we assess adequate for estimating spanwise structure spacing but not size. To any rate, [14] reports a spanwise size $\bar{\lambda}_z \simeq 0.45$ at $(x, y) = (3, 0.5)$, which is larger but not overly far from our values at the same location. If the three-dimensional structures were to appear in a (pseudo-)periodic spanwise pattern, one would expect to observe $N_{vp} \simeq L_z/\lambda_z$ equispaced vortex pairs filling the entire spanwise extent of the domain. As we have seen this is not the case and vortex pairs appear entirely decorrelated from

one another and vortices in isolation are oftentimes observed. Figure 2.19a shows the instantaneous count of vortex pairs N_{vp} as a function of time. Vortices are counted whenever cross-stream pseudo-vorticity exceeds a certain threshold $|\tilde{\omega}_y| \geq 8$ at the designated location, here $(x, y) = (3, 0.5)$. In some periods, corresponding to the traversal of Kármán vortices, no streamwise vortices are observed at all. Along the braids, isolated streamwise vortices and vortex pairs are regularly detected instead. Up to $4 \sim 4.5$ simultaneous vortex pairs have been detected occasionally, such that the average spanwise spacing between side-by-side pairs is $L_z/N_{vp} = 0.56 \sim 0.63$. This minimum spacing is well above the typical vortex-pair spanwise length-scale reported above, such that not even in these rare occasions do the three-dimensional structures appear in anything remotely resembling a periodic pattern like that observed for the A and B modes at much lower Reynolds numbers. Figure 2.19b presents in a histogram the fraction of time $X_{N_{vp}}$ that the probe array at $(x, y) = (3, 0.5)$ is detecting so many (N_{vp}) simultaneous vortex pairs. Isolated vortices are crossing the probe array just over 15% of the time and close to another 15% of the time a vortex pair (or two isolated vortices) is being detected. In our domain $L_z = 2.5$, the probability of observation of simultaneous vortex pairs is a strictly decreasing function of the number of vortices, with $N_{vp}^{max} = 0.5$ corresponding to maximum probability. It is natural to expect that in a much larger spanwise domain the maximum probability would correspond to a finite number of vortex pairs, larger than 0.5. As a matter of fact, for sufficiently extended domains one would expect N_{vp}^{max} to be inversely proportional to the spanwise domain size L_z, as this maximum is precisely indicating the typical spanwise spacing of vortices in the cylinder wake. One could argue that not respecting this typical spacing at which vortices feel *comfortable* may result in wrong turbulent statistics and that the spanwise size of the domain should at least fit this spacing once. As it **happens**, $L_z = 2.5$ seems to be about the minimum domain size that captures the probability distribution correctly up to the maximum, as the saturating value of $X_{N_{vp}}$ for $N_{vp}^{max} = 0.5$ seems to indicate. Larger domains will properly capture the probability maximum and part of the decreasing trend towards lower N_{vp}, while smaller domains will be forcing the maximum to be at lower spacing values than the cylinder wake would naturally select. We believe this may be among the reasons why insufficient spanwise domain sizes produce wrong statistics, here and in published results.

2.4.2.3 Fastest growing three-dimensional structures

Floquet stability analysis of the time-periodic two-dimensional flow around the cylinder has been successfully employed in the past to pinpoint the Re-regime at which three-dimensionality kicks in [85, 43]. The leading eigenmodes found are consistent with mode A observed in experiments and the hysteresis can be ascribed to the subcritical character of the bifurcation. Meanwhile, the existence of mode B has been tracked down via Floquet analysis to a secondary bifurcation of the already unstable two-dimensional periodic vortex-shedding regime [37]. These bifurcations introducing three-dimensionality to the flow occur in the range $Re \in [188.5, 260]$. If forced computationally to preserve two-dimensionality, vortex-shedding remains time-periodic for still some range of Re. At $Re = 2000$, however, periodicity has long been disrupted and two-dimensional vortex-shedding has become chaotic.

It is highly debatable whether Floquet analysis of the Kármán periodic solution at this regime can capture any of the features of the three-dimensional structures observed in experiments and in fully three-dimensional numerical simulations. Nonetheless, we have chosen here to undertake what we call pseudo-Floquet stability analysis of the underlying two-dimensional solution, which happens to be a pseudo-periodic chaotic state, to compare the fastest growing modes with the structures that arise in direct numerical simulation. Long two-dimensional time integration has been performed to characterise the chaotic state, with velocity and pressure fields $[\mathbf{u}_2^{2D}, p_2^{2D}](\mathbf{r}_2, t)$. Random three-dimensional perturbations $\tilde{\mathbf{u}}$ of wavenumber $\beta_z = 2\pi/\lambda_z$ (λ_z is the fundamental wavelength), scaled to very low amplitude by a factor $\epsilon \sim 10^{-12}$, have been added to $\mathbf{u}_2^{2D}$ at several randomly-picked time-instants and evolved in time using a single spanwise Fourier mode in order to avoid spanwise mode interaction and thus allow straightforward analysis, through direct time evolution, of the modal growth/decay in the linear regime. Since $[\mathbf{u}_2^{2D}, p_2^{2D}]$ exactly satisfy the Navier-Stokes equations, introducing the perturbed field

$$[\mathbf{u}, p](\mathbf{r}; t) = [\mathbf{u}_2^{2D}, p_2^{2D}](\mathbf{r}_2; t) + \epsilon[\tilde{\mathbf{u}}, \tilde{p}](\mathbf{r}; t)$$

results in

$$\frac{\partial \tilde{\mathbf{u}}}{\partial t} + (\mathbf{u}_2^{2D} \cdot \nabla)\tilde{\mathbf{u}} + (\tilde{\mathbf{u}} \cdot \nabla)\mathbf{u}_2^{2D} = -\nabla\tilde{p} + \frac{1}{Re}\nabla^2\tilde{\mathbf{u}}$$
$$\nabla \cdot \tilde{\mathbf{u}} = 0$$

where the nonlinear term $(\tilde{\mathbf{u}} \cdot \nabla)\tilde{\mathbf{u}}$ has been dropped as negligible from its appearing scaled by ϵ^2.
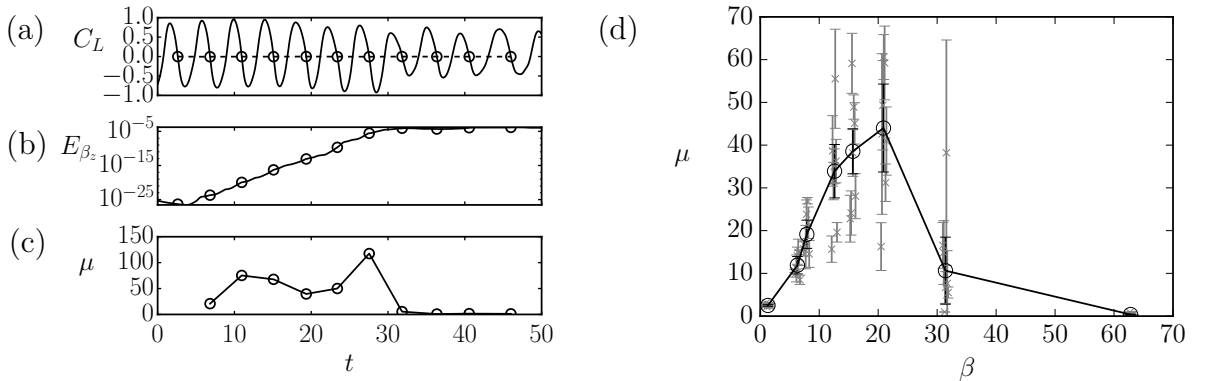
Figure 2.21: Quasi-modal evolution of a perturbation with $\beta_z = 2\pi/\lambda_z = 20.94$ ($\lambda_z = 0.3$) on two-dimensional chaotic vortex shedding at $Re = 2000$. (a) Time evolution of C_L as used to define a Poincaré section (Poincaré crossing marked with circles). (b) Evolution of the perturbation field kinetic energy. (c) Evolution of the multiplier as computed for every two consecutive Poincaré crossings. (d) Value of the multiplier μ as a function of spanwise wavenumber β_z. Seven different initial conditions for the chaotic base flow result in the multiple sets of data for each β_z (gray). All seven are gathered in a unique curve (black line). Error-bars indicate variability of the multiplier in time.

If $[\mathbf{u}_2^{2D}, p_2^{2D}]$ were exactly periodic, Floquet theory's modal ansatz would establish that, after some initial transients t_0, the perturbation field should evolve as

$$[\tilde{\mathbf{u}}, \tilde{p}](\mathbf{r}; t_0 + kT) = [\tilde{\mathbf{u}}_0, \tilde{p}_0](\mathbf{r}) \exp(\sigma kT) \qquad k \in \mathbb{N}$$

where T is the period of the two-dimensional periodic base flow and $\mu \equiv \exp(\sigma T)$ is the leading multiplier, associated to the leading eigenmode $[\tilde{\mathbf{u}}_0, \tilde{p}_0]$.

Here the base flow is not periodic but chaotic and the evolution of the perturbation field cannot be expected to be exactly modal. However, since two-dimensional chaotic vortex shedding retains a high degree of periodicity, the time evolution of the perturbation happens to be quasi-modal. Figure 2.21 shows an example of the growth of the single Fourier mode with $\beta_z = 20.94$ on top of the chaotic two-dimensional base flow. A pseudo-periodic chaotic solution as we have has no unique period, so that we choose to define it as the flight time between consecutive crossings of a purposely devised Poincaré section: $T_k = t_k - t_{k-1}$. In our case, the Poincaré section is pierced by the phase map trajectory every time $C_L = 0$ and $dC_L/dt < 0$, as indicated by the dashed line and the circles in figure 2.21a. The kinetic energy E_{β_z} contained in the unique spanwise Fourier mode employed in the simulation is shown in figure 2.21b. After some initial transients with a slight decrease, the modal energy starts increasing following an exponential trend for $t \gtrsim 10$ until nonlinear saturation occurs for $t \gtrsim 30$.

44

The energy levels of the unique spanwise mode of wave-number β_z at the Poincaré crossings are marked with circles and the multipliers μ_k estimated at crossing k from the energy ratio between consecutive crossings $k-1$ and k as

$$\frac{E_{\beta_z}^k}{E_{\beta_z}^{k-1}} = \frac{\|\tilde{\mathbf{u}}^k\|_{L_2}^2}{\|\tilde{\mathbf{u}}^{k-1}\|_{L_2}^2} = \exp(2\sigma T_k) \equiv \mu_k^2$$

where $\|\cdot\|_{L_2}$ denotes L_2 norm, and plotted in figure 2.21c. As expected for an unstable base flow, the multiplier is greater than unity, but unlike what happens for an exactly periodic base flow, its value is variable along the evolution. In the case of our chaotic two-dimensional vortex shedding, the variability of the multiplier is rather large.

Up to seven different initial base state conditions along the two-dimensional chaotic vortex shedding evolution have been taken and tested for spanwise wavelengths in the range $\lambda_z \in [0.1, 10]$, corresponding to wavenumbers $\beta_z \in [0.628, 62.8]$. The results for the seven individual samples are shown in figure 2.21d as gray crosses with error-bars, which indicate the mean and standard deviation of the multiplier along the time evolution, respectively. In some cases the fluctuation is small, corresponding with initial conditions at a stage of the time evolution where vortex-shedding is particularly well behaved. In others, the variability is huge. Averaging the probability distribution of μ across samples reduces the variability in the multiplier to some extent and produces a softer dependence of the multiplier on the wavenumber. The maximum growth of infinitesimal three-dimensional perturbations seems to occur for spanwise wavenumbers $\beta_z \simeq 20.94$, which corresponds to a spanwise wavelength $\lambda_z = 2\pi/\beta_z \simeq 0.314$. This wavelength is in good agreement with the spanwise size of the structures we observe in the wake region in fully three-dimensional turbulent simulations, particularly so in the very near-wake region at $(x, y) = (0.5, 0.5)$.

A snapshot of the fastest growing leading eigenmode, taken at the time of a Poincaré crossing within the linear regime, is depicted in figure 2.22b, while figure 2.22a shows the instantaneous two-dimensional state at the exact same time. The spanwise vorticity (ω_z) colourmap indicates that the mode is at its strongest along the braid region that connects the newly forming Kármán vortex core in the immediate vicinity of the cylinder and the preceding vortex of the same sign. The instability is local in the sense that exponential growth occurs only at a very precise location within the wake formation region and does not extend to the region where the wake is already in place and the Kármán vortex street well developed. Infinitesimal perturbations of spanwise wavelength $\lambda_z = 2\pi/\beta_z = 0.3$ are therefore exponentially growing only within the most recently generated braid at all times. There is no
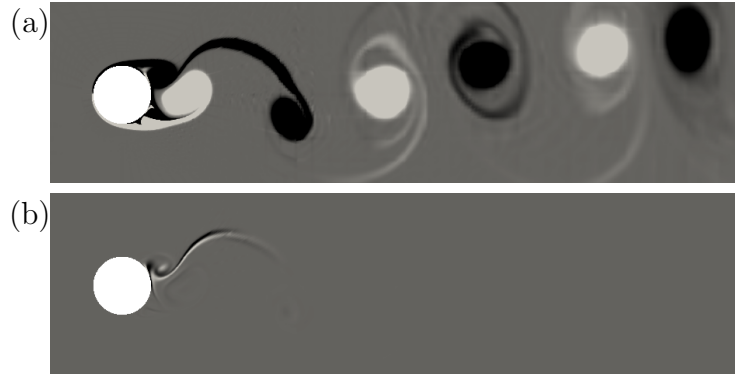
Figure 2.22: Spanwise vorticity (ω_z) colourmaps at the Poincaré section defined by $C_L = 0$ and $dC_L/dt < 0$ of (a) the two-dimensional chaotic vortex shedding solution ($\omega_z \in [-2, 2]$) and (b) the leading eigenmode (arbitrary symmetric ω_y range) for $\beta_z = 20.94$.

guarantee that the perturbation reaches nonlinear saturation unaltered and thus constitutes the origin of the three-dimensional structures observed in experiments and direct numerical simulation, but they certainly have the right spanwise size and are located in the precise flow regions where the structures thrive. This gives an indication that the structures observed in the wake at these transitional regime might bear a strong connection with the fastest growing mode on the underlying two-dimensional base flow.

2.5   Conclusions

Linear stability analysis of the two-dimensional wake of a circular cylinder has been carried out via pseudo-Floquet analysis at Re=2000 to identify fastest growing Fourier modes in the homogeneous direction. DNS of the flow past circular cylinder at the same Re is also carried out using high oder SEM and length scales of the three-dimensional disturbance behind circular cylinder evaluated using Hilbert transform, compares well with wavelengths of unstable modes predicted by stability analysis and power law, i.e. $20/\sqrt{Re}$ suggested by Mansy et al. [14]. The three-dimensional disturbance is seen to be strongest in the near wake region close to the large-scale spanwise vortex formation corroborated by previous investigations. Temporal analysis of the strengths of primary and secondary flow components reveals that strongest three-dimensional spanwise fluctuation occurs once every Karman Strouhal cycle in the braid region between large scale spanwise vortices. The footprints of shear layer vortices have been observed in the spectra of streamwise and cross-stream flow velocities

which are characterized by broadband peak at frequencies other than fundamental frequencies and/or their harmonics. Spanwise wavelength of three-dimensional disturbance has been quantified using Hilbert transform of the pseudo crossflow component of vorticity. Streamwise and cross-stream evolution of the average wavelength display opposite behavior in the shear layer and wake regions: in the shear layer region, average wavelength decrease as a function of streamwise distance until it reaches a minimum value and increases thereafter in the wake region.

Chapter 3

Active flow control implementation for flow over circular cylinder at Reynolds number ($Re = 2000$)

3.1 Introduction

The fluid flow around blunt objects, even in low to moderate flow regimes, results in large unsteady wakes that are the source of aerodynamic drag, vibrations, and noise, while on the other hand, they can be exploited for the enhancement of flow mixing, heat/mass transfer and energy harvesting purposes. The aerodynamic boundary layers (BL) developing on the solid surfaces undergo an early separation due to the strong adverse pressure gradients faced at the leeward side of bluff bodies. This early separation is at the origin of the massive suction wakes. Prominent practical examples are the flows around moving hatchback cars and trucks, high buildings and bridge pillars subject to wind, or wings/blades operating at high angles of attack.

The incompressible flow of a viscous fluid around a circular cylinder constitutes a paradigm of flow separation and unsteady wake formation behind bluff bodies [83], together with backward facing steps (and ramps), humps, and the Ahmed body.

Flow control strategies have been exploited to tame wake unsteadiness and separation over these and other bluff body geometries [86, 87]. Among these strategies, active flow control (AFC) has shown a great potential [88] thanks to its adaptable capability for exploiting Fluid flow global instability modes [89]. Fluidic actuation [18] aims at precisely this by the addition/subtraction of momentum to/from the boundary layers developing in the immediate vicinity of the solid walls. In the case of a cylinder wake, fluidic actuation has been shown very effective in reducing and even suppressing unsteady vortex shedding at flow regimes beyond the secondary three-dimensional

instability [90]. Spanwise dependent actuation has been proved utterly effective for the reduction of fluctuating forces and aerodynamic drag [91, 92, 26, 93]. Kim & Choi [23] found similar results with the application of distributed forcing on the flow past a circular cylinder in the low to moderate Reynolds number flow regimes. In principle, spanwise-dependent actuation induces low amplitude streamwise vortices that naturally develop into strong streaks which ultimately suppress the absolute instability in the near wake [94, 95] showing better performance than spanwise-independent forcing. This efficiency has, nevertheless, only been demonstrated at low flow regimes below the onset of three-dimensionality.

It is pertinent here to clarify local/global and absolute/convective instabilities notions in order to familiarize with these concepts. In order to do so, consider the time-averaged mean velocity profile at a given streamwise location inside the wake such that $U_B(y; Re)$ At the local level of description, it is further necessary to characterize the impulse response, Green's function, of the system within the parallel-flow approximation at each streamwise station. If localized disturbances spread upstream and downstream and contaminate the entire parallel flow, the velocity profile is said to be locally absolutely unstable. If, by contrast, disturbances are swept away from the source, the velocity profile is said to be locally convectively unstable. If the basic flow U_B is not only a function of crossflow coordinate but also it depends on streamwise location then system response has to be evaluated in the entire domain.

Generally, mechanisms associated with vortex-shedding-control ultimately seem to be related to weakening or in some cases elimination of the inherent local instabilities. Leu & Ho (2000) [96] reported reduction in the length of local absolutely unstable region by introducing suction in a two-dimensional plane wake at $Re = 2000$. The global instability was completely annihilated at the critical suction speed, i.e. 46% of free stream velocity. The global linear theory of Monkewitz et al. [97] predicted remarkably good value of threshold suction speed with the incorporation of non-parallel correction term. Giannetti & Luchini [98] found regions of absolute instability by the correlation of direct and adjoint eigenfunctions. The sensitive regions appear to lie within/around the wake center-line and separated shear layers. Kim & Choi [23] found that the distributed forcing with adequate wave length suppressed the wake instability for flow past a circular cylinder. Guercio et al. [99] forced the parallel wakes with streamwise vortices which resulted in streamwise streaks that suppressed the global instability. In order to confirm whether or not suppression of global instabilities is linked to the annihilation of wave-make region, they considered non-parallel wake flow with finite region of absolute instability in their follow-up study.

They found that spanwise dependent forcing resulted in greatly amplified streamwise streaks which have a stabilizing effect on the global instability [100, 95], and the optimal wavelengths were in good agreement with previous findings. The above mentioned stability analyses are linear. However, at higher Reynolds numbers linearized stability equations may become non-normal which may lead to the simultaneous excitation of different modes which may render the control method destabilizing. A control strategy applied to suppress a given mode may simultaneously excite some other modes. Therefore, special care is required when applying control methods to high Reynolds number flows.

Time-dependent actuation at frequencies in the vicinity of natural frequencies of the unsteady wake (vortex shedding or shear layer/ Kelvin-Helmholtz instability) have been proven effective for a wide range of bluff body geometries and flow regimes [29]. Williams et al. [27] found that the global instability ceased to form in the near wake at relatively high forcing amplitudes in the flow past a circular cylinder at post-secondary-instability regime when unsteady perturbation in the from of blowing/suction applied from the surface of the cylinder. He provided explanation of the wake topology based on the symmetry properties of the interacting modes i.e. natural vortex shedding and forcing modes following the decomposition method of [101].Lin et al. [28] inhibited the global instability by forcing the cylinder wake in the turbulent flow regime(Re=10000) by unsteady blowing-suction through the holes on the cylinder surface arranged in a helical pattern. The main idea was to induce three dimensionality which would interact with the two-dimensional von Kármán vortex shedding similar in effect to helical strakes [102]. A large drag reduction [103]is attained for flow past sphere by exciting shear layer instability with periodic blowing and suction from the slots located just upstream of flow separation point. A critical forcing frequency of $2.85f_{vK}$(where f_{vK} is the natural vortex shedding frequency) was reported which exited the shear layer instability and resulted in flow separation delay further downstream. Similar mechanism for drag reduction for flow past circular cylinder was found by Fujisawa & Takeda [104] with the introduction of acoustic excitation at the frequency close to the shear layer instability.

Spanwise dependent forcing has been proven quite successful to inhibit global instability at relatively low Reynolds numbers, similarly, time-dependent actuation is found to be remarkably effective even in the turbulent regime, therefore, application of spanwise-dependent forcing complemented with time-dependence actuation on flow past circular cylinder at Re=2000 is worth exploring. To the author knowledge this area remains to be unexplored which is the subject of present work.
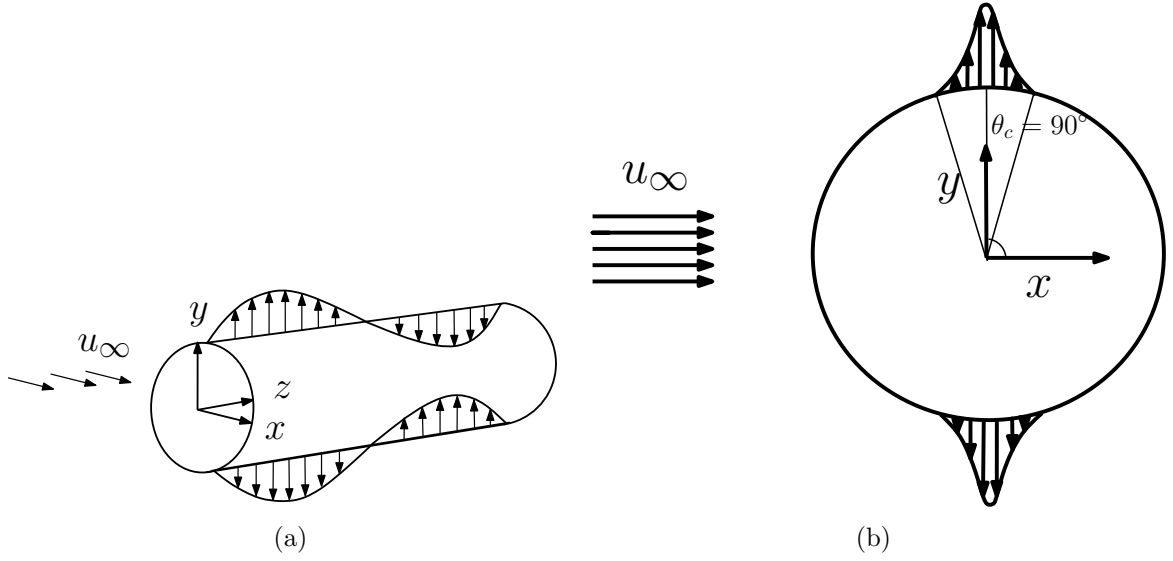
Figure 3.1: Schematic diagram depicting forcing on flow past circular cylinder: (a) prospective view of symmetric forcing about y=0 plane and (b) side view with $\theta_c = 90°, \zeta = 1°$

The incompressible viscous flow past circular cylinder, with AFC implemented, is governed by Navier-Stokes equations, non-dimensionalized by cylinder diameter D, fluid kinematic viscosity ν, and upstream flow velocity U, given by Eq. 2.1. In this thesis, spanwise-dependent forcing in steady and time-periodic manner is implemented from the slits located at the top and bottom surface of the cylinder placed in cross flow. The forcing location was selected slightly upstream of the separation point to excite the boundary layer so that maximum effect of the actuation could be obtained. The forcing has a sinusoidal waveform in the spanwise direction and Gaussian profile in the streamwise-crossflow plane, given as

$$U(D/2, \theta, z) = U_{max} e^{-(\theta-\theta_c)^2/(2\zeta^2)} sin(2\pi z/\lambda_z) \tag{3.1}$$

where U is the local normal velocity to the surface of the cylinder, λ_z is the spanwise forcing wavelength, U_{max} is the maximum forcing velocity, θ_c is the central angle of the slot azimuthal location, and ζ is the slot width. The forcing is symmetric about the wake center plane both in the steady and unsteady configurations. Typical forcing sketch is shown in figure 3.1. Experimental results of circular cylinder in cross flow at Re closer to the present study together with measurement techniques, turbulent intensity levels (Tu), mean drag coefficients ($\bar{C}_D$) and mean base suction coefficients

$(\bar{C}_{p_b})$, recirculation lengths (L_r), spanwise domain extents (L_z), and frequencies related to primary instability (f_{vK}) etc are shown in Table 1. Excellent agreement in the values of $\bar{C}_D$, f_{vK}, and $\bar{C}_{p_b}$ has been observed between present DNS and experimental measurements at closest Re considered in the present numerical experiment.

3.2 Active flow control implementation Results and discussion

3.2.1 spanwise-dependent time-independent(SDTI) forcing

In this section, the mesh with 5484 quadrilateral elements in the streamwise-crossflow plane has been employed, and Fourier mode i.e. $N_z = \pm 64$ have been utilized in the spanwise direction with spanwise domain extent of $L_z = 2D$.

Parametric investigation is carried out with steady forcing to explore optimal settings for forcing amplitude (A) and wavelength (λ). The optimal spanwise wavelength of disturbance is found while keeping the A fixed at the value of 20% of inlet velocity i.e. ($A = 0.2u_0$). The forcing slot is fixed at $\theta = \pm 90°$ with respect to the front stagnation point, and slot width is chosen to be 1 degree. Figure 3.2 shows the evolution of lift and drag coefficients for spanwise wavelength of disturbance ranging from $0.25D$ to $2D$ at a fixed forcing amplitude $A = 0.2u_0$. It is clear from the figure 3.2

| (a) | (b) |
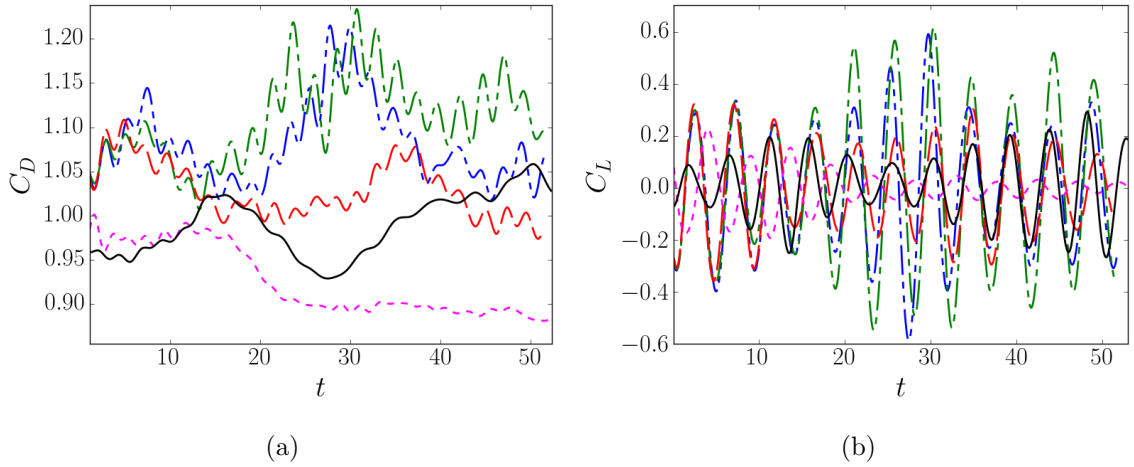
Figure 3.2: Lift and drag coefficients with varying spanwise-forcing-wavelength at $A = 0.2u_0$: (a) drag coefficient; (b) lift coefficient; (solid line, black) uncontrolled case; (dotted line, purple) controlled case with $\lambda_z = 2D$; (— —, red) controlled case with $\lambda_z = D$; (— · —, green) controlled case with $\lambda_z = 0.5D$; (— · · —, blue) controlled case with $\lambda_z = 0.25D$

that forcing wavelength of $2D$ seems to be the most effective in terms of drag and lift fluctuation amplitude reduction. Drag coefficient decreases with the increase of λ_z except for $\lambda_z = 0.5D$ where drag increase is observed. From figure 3.2a, in all control cases except $\lambda_z = 2D$ mean drag coefficient is larger than the uncontrolled case which is evident in mean base pressure coefficient plot as shown in figure 3.3.
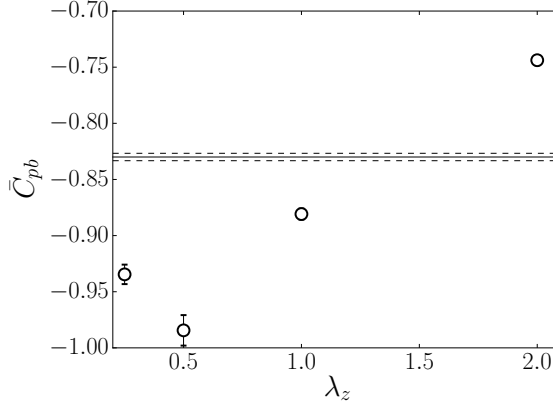
Figure 3.3: mean base-suction coefficient owing to different disturbance wavelengths with fixed forcing amplitude ($A = 0.2$): (solid line) uncontrolled case with dash lines denoting rms values (along the span) about the mean, and the error bars indicate rms values along the span.

This figure shows the time-averaged and spanwise-averaged base pressure coefficient for uncontrolled and controlled cases with error bars showing rms fluctuations along the spanwise direction. These results are similar to the parametric study of [23] at $Re = 100$, where he found gradual decrease of drag coefficient with the increase in disturbance wavelength until optimal wavelength i.e. $\lambda_z = 4D - 5D$ is reached, and beyond optimal wavelength modulation appeared in the time traces of lift coefficient which they related to the variation of vortex shedding frequency along the spanwise direction.

Figure 3.4 shows the vortical activities in the streamwise-crossflow plane occurring in the wake of controlled cases with different wavelengths. The vortical structures are computed following the methodology suggested by [105]. One can readily identify large scale primary instability present in the cylinder wake, together with streamwise vortices appearing in the braid regions between the vortices core regions.

A strong vortical activity is observed for controlled cases with $\lambda_z = 0.5D$ and $1D$. In contrast to that, vortical activity has been disrupted in the near wake for the optimal forcing wavelength case where it starts to develop farther downstream. The distortion of vortices in the optimal case helps recover pressure in the near wake, together with reduction in drag coefficient.

It has been observed that larger actuation wavelengths yield better improvement in the aerodynamic parameters which were not anticipated at the time of numerical study.

Now, we present the effect of forcing amplitude on the global flow parameters i.e.
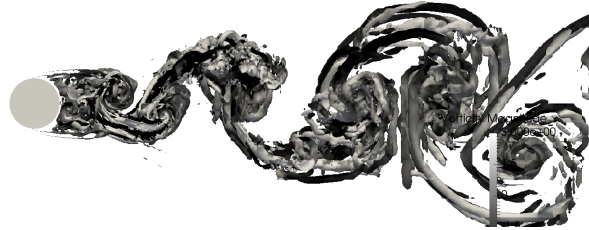
(a)
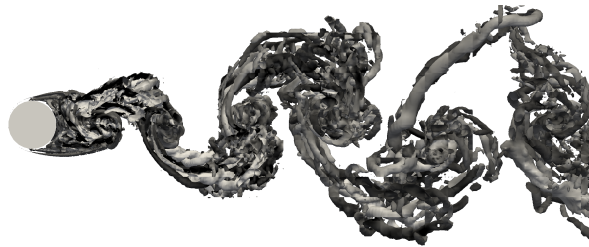
(b)
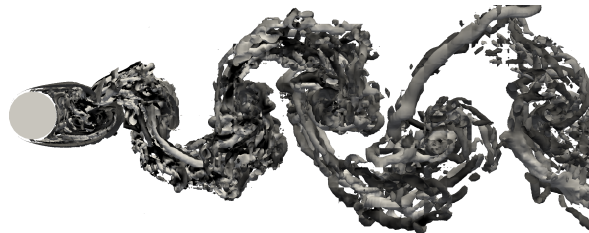
(c)
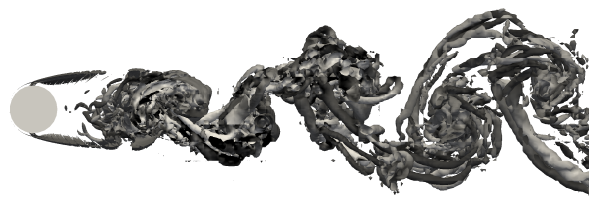
(d)

Figure 3.4: Instantaneous wake structures of controlled cases computed using Q-criterion (iso-surface=1): (a) baseline case (b) $\lambda_z = 0.5D$; (c) $\lambda_z = D$; (d) $\lambda_z = 2D$.
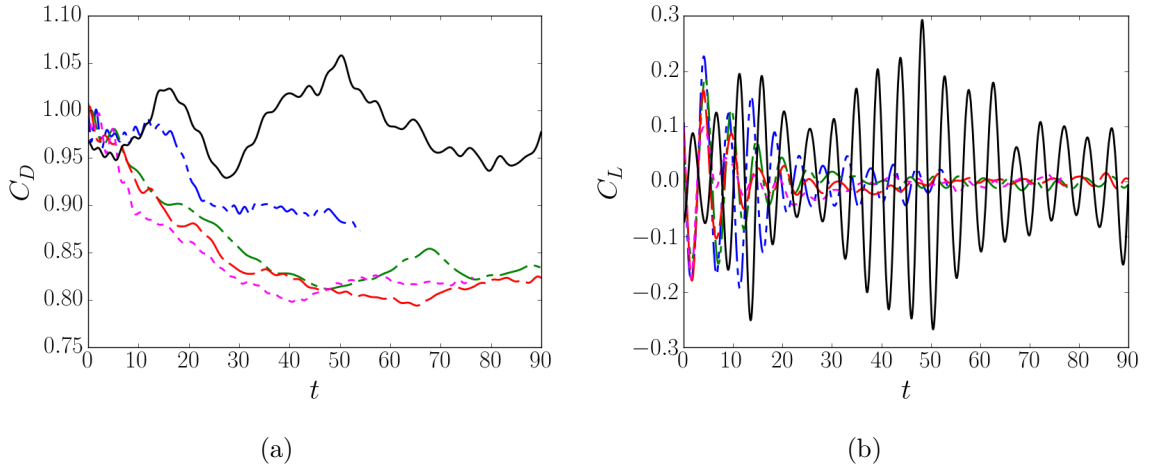
Figure 3.5: Drag and lift coefficients with varying actuation amplitude: (a) drag coefficient (C_D); (b) lift coefficient (C_L); (solid line, black) uncontrolled case; (— ·· —, blue) controlled case with $A = 0.2u_0$; (— · —, green) controlled case with $A = 0.3u_0$; (— —, red) controlled case with $A = 0.4u_0$; (dotted line, purple) controlled case with $A = 0.5u_0$

drag and lift coefficients. The spanwise wavelength of disturbance is fixed at $\lambda_z = 2D$ and the forcing amplitude A is varied from $0.2u_0$ to $0.5u_0$ with an increment of $0.1u_0$, and the spanwise domain length is always set as $L_z = 2D$.

Figure 3.5 shows that drag decreases as the forcing amplitude is increased when compared with the uncontrolled case, however, for cases $A \geq 0.3u_0$, the drag is saturated to a constant value. Similar effects can be seen for the lift coefficient plot where no further reduction in the lift coefficient amplitude is observed beyond $A \geq 0.3u_0$. Therefore, forcing amplitude $A = 0.3u_0$ has been considered as the most effective one for the rest of the analysis.

3.2.2 Periodic spanwise-dependent (PSD) forcing

In this section, we explore the effect of forcing frequency on the global flow parameters and wake instability. Here, the forcing wavelength and amplitude have been set to $\lambda_z = 2D$, $A = 0.3Du_0$. Several researches show promising results in terms of drag reduction and lift attenuation when excitation frequency ranging from $f_{vK} \leq f_e \leq f_{KH}$ was used to force the flow past bluff bodies at moderate Reynolds number, where f_{vK} is the von Kármán shedding frequency, f_e is the excitation frequency, and f_{KH} is the Kelvin Helmholtz instability frequency. We investigate three forcing frequencies corresponding to $f_e = f_{vK}, 2f_{vK}, 4f_{vK}$, where $4f_{vK}$ is closer to the shear layer instability of flow past circular cylinder [106, 107] i.e. $f_{KH} = 1.121$.
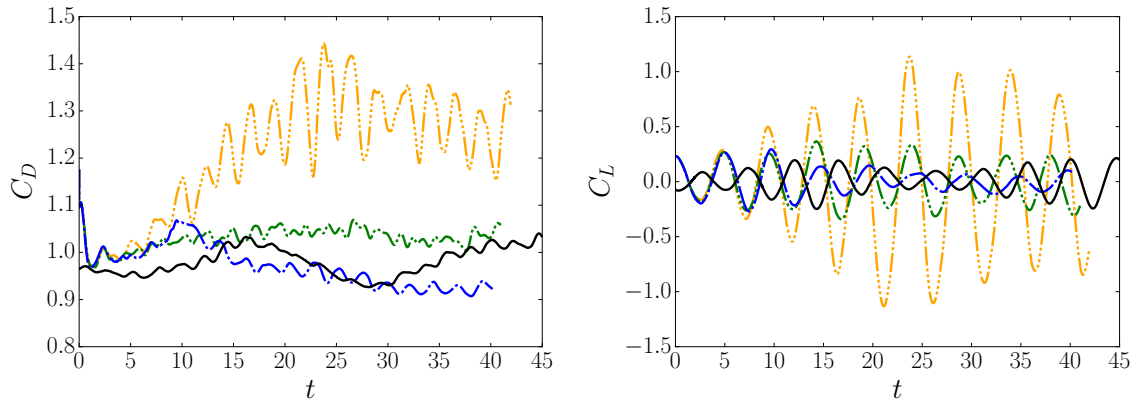
Figure 3.6: Drag and lift coefficients with varying actuation frequency: (a) drag coefficient C_D; (b) lift coefficient C_L. (solid line, black) uncontrolled case; (— · —, blue) controlled case with $f_e = f_{vK}$; (— · · —, green) controlled case with $f_e = 2f_{vK}$; (— · · · · —, orange) controlled case with $f_e = 4f_{vK}$

Figure 3.6 shows the drag and lift coefficients under the influence of different actuation frequencies. There is a reduction in drag and corresponding lift coefficients at excitation frequency $f_e = f_{vK}$ while no significant effect of excitation at $f_e = 2f_{vK}$ is observed on the global flow parameters such as drag and lift coefficients. Interestingly, drag and lift coefficients show substantial increase when forced at $f_e = 4f_{vK}$. This explains the fact that forcing frequency closer to Kelvin Helmholtz instability excites natural shear layer instability and large amplitude lift fluctuation and drag increment is observed as a result of this resonance.

It is also interesting to note that shear layer instability appears intermittently with frequency $f_{KH} = 1.121$ in the baseline case, $L_z = 2D$, which confirms thats the increase in lift fluctuation is caused by excitation of shear layer instability.

Figure 3.7 shows the vortical structures in the streamwise-crossflow plane in the wake of controlled cases with varying forcing frequencies. An intense vortical activity can be spotted for controlled case with $f_e = 4f_{vK}$ resulting in the reduction of formation length together with base pressure as shown in figure 3.8. One can notice an increase in the formation length for controlled case with $f_e = f_{vK}$ causing corresponding increase in base pressure as shown in figure 3.7a. Again, the error bars in the plots are indicating rms values of respective pressure coefficients along the span.

3.2.3 Spanwise traveling sinusoidal (STS) forcing

In this section, we describe the effect of unsteady forcing in the form of moving sinusoids from the slits located on the top and bottom surface of the cylinder, traveling

(a)

(b)

(c)
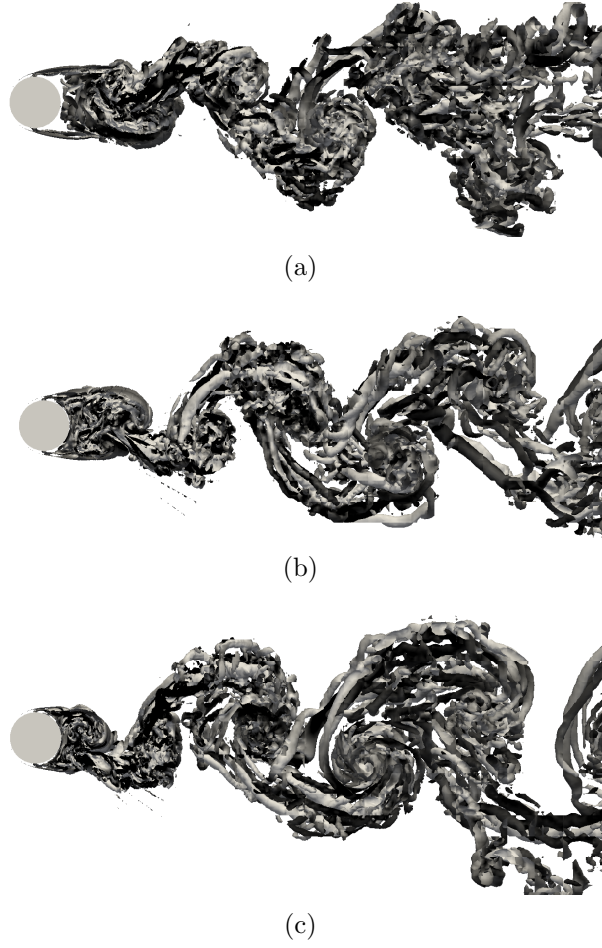
Figure 3.7: Instantaneous wake structures of PSD controlled cases computed using Q-criterion(iso-surface=1): (a) $f_e = f_{\text{vK}}$; (b) $f_e = 2f_{\text{vK}}$; $f_e = 4f_{\text{vK}}$.

oppositely along the span with the speed $S = 0.5f_{\text{vK}}\lambda_z$, $f_{\text{vK}}\lambda_z$ such that forcing on top and bottom become in-phase as PSD every $2D/af_{\text{vK}\lambda_z}$ and anti-phase exactly in between, where $a = 0.5, 1$. Again, the forcing wavelength and amplitude has been set to $\lambda_z = 2D$, $A = 0.3u_0$. Figures 3.9a and 3.9b show both the reduction and suppression of drag coefficient and lift fluctuation compared to uncontrolled case. Nevertheless, the amount of drag reduction and suppression of lift fluctuation is more for $S = 0.5f_{\text{vK}}\lambda_z$ as compared to $S = f_{\text{vK}}\lambda_z$, which is probably related to the spanwise disruption of shear layer evolution phenomena in the near wake which is explained later.

Figure 3.10 shows the vortical structures in the streamwise crossflow plane in the wake of controlled cases with varying forcing speeds. It is quite clear that vortical activity is disrupted in the near wake of controlled case $S = 0.5f_{\text{vK}}\lambda_z$ and vortex formation occurs further downstream as compared to the $S = f_{\text{vK}}\lambda_z$. The further the
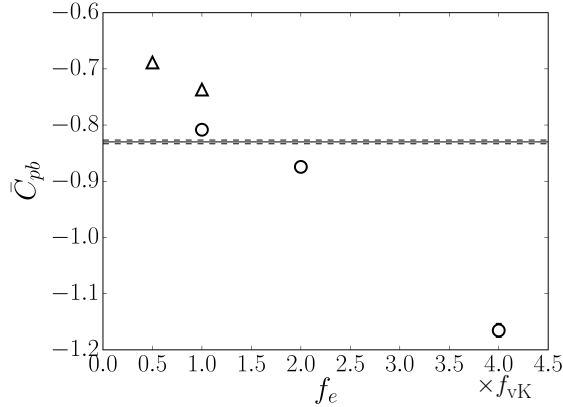
Figure 3.8: mean base-pressure coefficients for PSD controlled cases. (solid line: baseline, and dash lines denote r.m.s about mean), (open circle: PSD), and (triangle: STS)
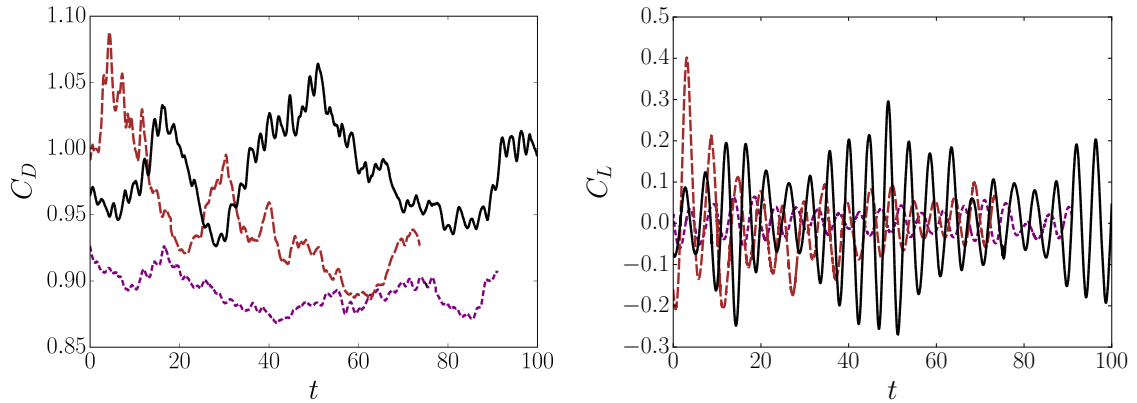
| | |
| (a) | (b) |

Figure 3.9: Drag and lift coefficients with different forcing waveform speeds: (a) drag coefficient (C_D); (b) lift coefficient (C_L). (solid line, black) uncontrolled case; (dotted, purple) controlled case with $S = 0.5f_{vK}\lambda_z$; (dash, brown) controlled case with $S = f_{vK}\lambda_z$

vortex formation takes place, the lesser is the upstream effect of von Kármán vortex shedding on the cylinder, and consequently the larger pressure recovery is achieved in the wake as shown in figure 3.8.

3.2.4   Discussion

The effect of flow actuation in the form of blowing and suction on the formation length and wake width is shown in figure 3.11. The formation length has been computed as a distance along the wake center line from the base of the cylinder to a point where $\langle u'u' \rangle$ reaches maximum and wake width is found by searching the maximum $\langle u'u' \rangle$ at the same point but traversing along the cross stream direction, and

59

(a)　　　　　　　　　　　　　　　　(b)
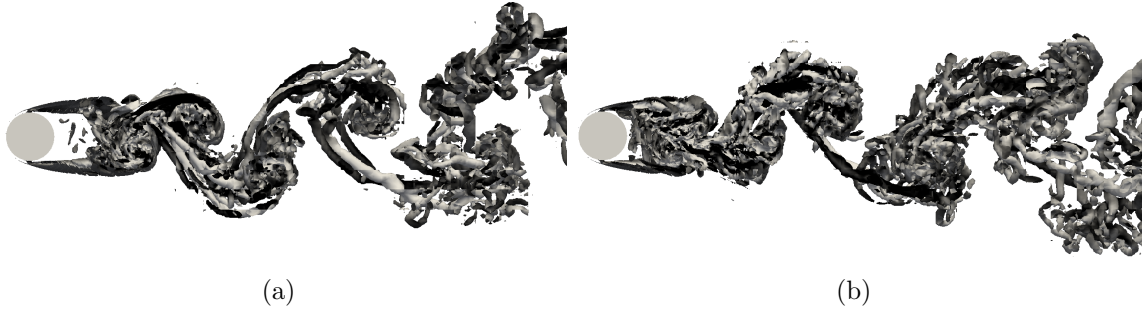
Figure 3.10: Instantaneous wake structures of STS controlled cases computed using Q-criterion(iso-surface=1): (a) $S = 0.5 f_{\text{vK}} \lambda_z$; (b) $S = f_{\text{vK}} \lambda_z$.

(a)　　　　　　　　　　　　　　　　(b)
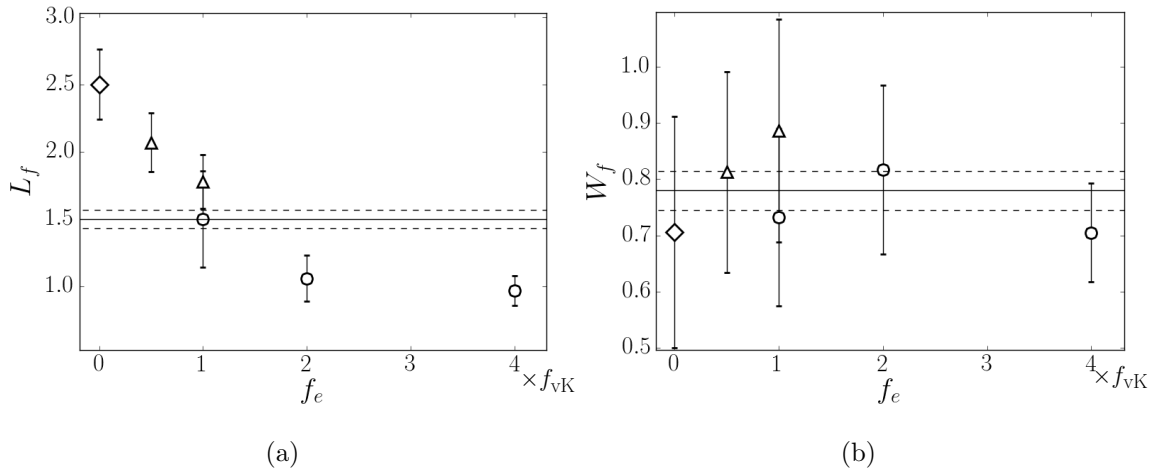
Figure 3.11: Vortex formation length (L_f) and Wake width (W_f) for controlled cases: (a) formation length; (b) Wake width. (solid line: baseline), (diamond: SDTI), (triangle: STS), and (circle: PSD)

;

the error bars indicate the rms of the corresponding quantity about the spanwise mean. Spanwise-dependent time-independent forcing shows the largest vortex formation length, followed by the forcing with spanwise-traveling sinusoids having speed $S = 0.5 f_{\text{vK}} \lambda_z$, $S = f_{\text{vK}} \lambda_z$, and then periodic spanwise-dependent actuation with forcing frequency corresponding to f_{vK}, $2 f_{\text{vK}}$ and, $4 f_{\text{vK}}$, respectively. The aerodynamic parameters in the form of coefficients of mean drag, lift fluctuation, base pressure and their respective % reduction is shown in table 2. These quantities are averaged both in time and spanwise direction. The maximum drag reduction is obtained in the case of SDTI actuation, followed by STS in both cases, and PSD with forcing frequency of f_{vK}.

Figure 3.12 and 3.13 demonstrate the $\langle u'v' \rangle$ Reynolds stress for the uncontrolled and controlled cases as $\langle u'v' \rangle$ is an extremely useful to quantify vortical activity in the near wake. As can be seen from figure 3.12a Reynolds stress develops further

60
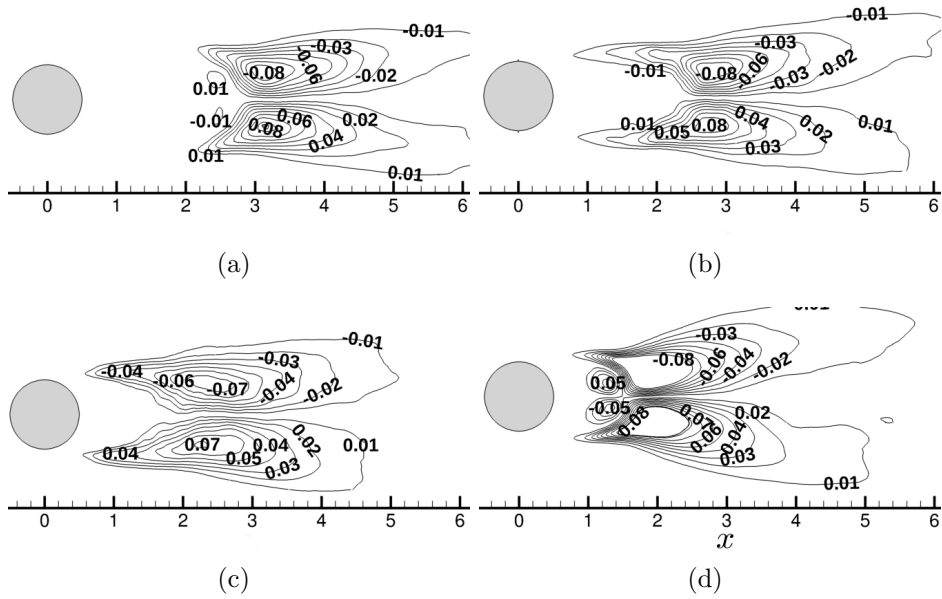
Figure 3.12: $\langle u'v' \rangle$ contours of controlled cases in the near wake region of circular cylinder: (a) SDTI case; (b) STS case with $S = 0.5f_{\mathrm{vK}}\lambda_z$; (c) STS case with $S = f_{\mathrm{vK}}\lambda_z$; (d) uncontrolled case.
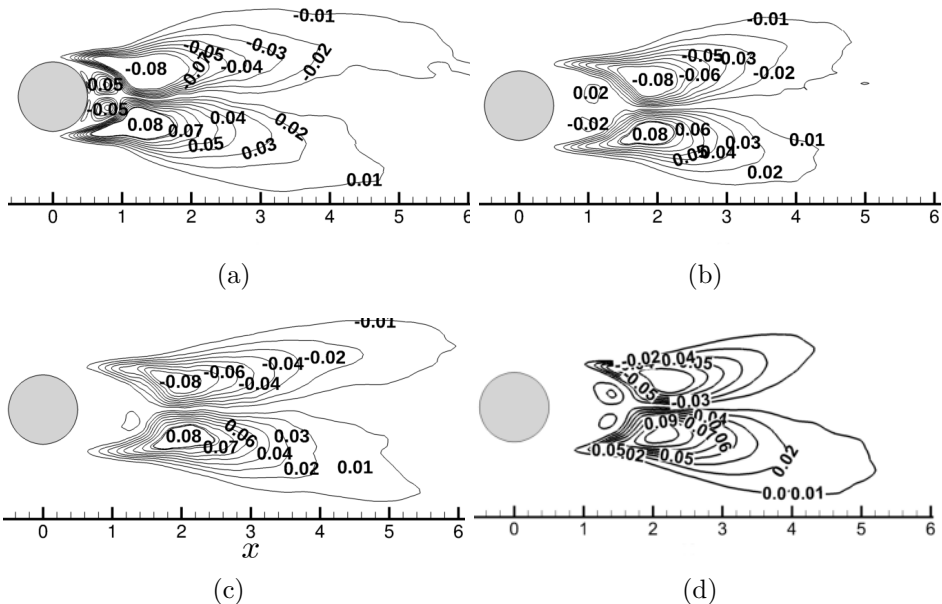
Figure 3.13: $\langle u'v' \rangle$ contours of controlled cases in the near wake region of circular cylinder: (a) PSD case with $f_e = 4f_{\mathrm{vK}}$; (b) PSD case with $f_e = 2f_{\mathrm{vK}}$; (c) PSD case with $f_e = f_{\mathrm{vK}}$; (d) baseline case.

downstream behind the cylinder for SDTI case, resulting in almost no vortical activity in the near wake. For STS cases, vortex development takes place further from the cylinder base as compared to uncontrolled case which is the prime reason for drag reduction, however $\langle u'v' \rangle$ contours for SDTI case are closely spaced as compared to STS cases where Reynolds stress contours are rather wider, and their upstream tails extends much longer as compared to SDTI case.

Figure 3.13 shows the pattern of Reynolds stress for the PSD cases where location of $\langle u'v' \rangle$ peak value is moved upstream for controlled cases with forcing frequency $2f_{\mathrm{vK}}$, $4f_{\mathrm{vK}}$, in contrast to that, Reynolds stress peak value shifted downstream for the controlled case with actuation frequency f_{vK}. The tails of Reynolds stress extends for a larger distance in the upstream direction together with an increase of the Reynolds stress peak value region resulting in intensification of vortex shedding for both controlled cases with forcing frequency $2f_{\mathrm{vK}}$, $4f_{\mathrm{vK}}$. The error bars in figure 3.11 show the rms of mean quantity along the spanwise direction which is related to spanwise variation of formation length. Kim & Chio [23] reported that in case of distributed forcing drag reduction is obtained from the spanwise distortion of vortex shedding and this effect is maximized close to the maximum suction location along the span. This phenomena could be linked to the drag reduction for SDTI case. Similar phenomena could also be at work with the difference that now disruption in shear layer evolution behind circular cylinder is occurring randomly along the span rather than at a fixed spanwise position which explains the larger rms values of figure 3.11 for the STS controlled cases.

Table 3.1: Changes in the mean properties due to AFC. The bar indicated time-averaged and rms stand for root-mean-square of the quantities in time.

	f_e	S	$\mathbf{A}$	λ_z	$\bar{C}_D$	$\acute{C}_L$	$\overline{C}_{pb}$	$\Delta C_D^{\mathrm{rms}}$	$\Delta C_L^{\mathrm{rms}}$
Baseline-case	-	-	-	-	0.987	0.132	-0.83	-	-
Steady	-	-	0.3	2D	0.845	0.011	-0.73	14.3%	91.7%
Unsteady	f_{vK}	-	0.3	2D	0.92	0.061	-0.8	6.8%	53.8%
Unsteady	$2f_{\mathrm{vK}}$	-	0.3	2D	1.034	0.179	-0.88	-4.8%	-35.6%
Unsteady	$4f_{\mathrm{vK}}$	-	0.3	2D	1.29	0.665	-1.16	-30.7%	-403.8%
Traveling unsteady	-	$0.5f_{\mathrm{vK}}\lambda_z$	0.3	2D	0.88	0.025	-0.69	10.84%	81.1%
Traveling unsteady	-	$f_{\mathrm{vK}}\lambda_z$	0.3	2D	0.91	0.056	-0.74	7.8%	57.6%

The vortex formation and shedding is related to the values of $\langle u'v' \rangle$, $\langle u'u' \rangle$ which is higher for PSD controlled cases and smaller for STS and SDTI cases.
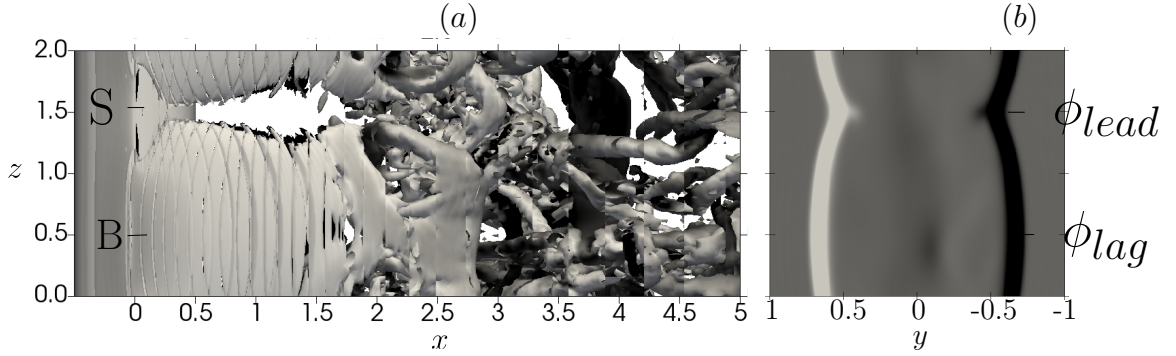
Figure 3.14: Instantaneous vortical structures behind cylinder. (a) Top view of vortical structures for SDTI for ($\lambda = 2D$, $A = 0.3u_0$) computed using Q-criterion=1. (b) (y, z)-plane of color map of $\omega_z \in [-5, 5]$ sectioned at $x = 0.5$.

3.2.4.1   Mechanism of drag reduction

Here, we propose a potential mechanism responsible for the reduction of drag force for AFC cases. It has been noticed that spanwise-dependent forcing when applied in the in-phase configuration disrupts the vortex formation process in the near wake. Shear layers separating from the top and bottom of cylinder surface are distorted in such a way that the flow is decelerated right behind the maximum blowing point i.e. $z = 0.5D$, causing a phase lag, and is accelerated right behind the maximum suction location i.e. $z = 1.5D$, generating a phase lead, resulting in delay of vortex formation process downstream of circular cylinder as shown in fig 3.14 a and fig 3.14 b. This conjecture is supported by the contours of velocity magnitude drawn in the (x, z) plane at $y = 0.5D$. A high velocity region of flow emanating close to the maximum suction point is evident in fig 3.15.
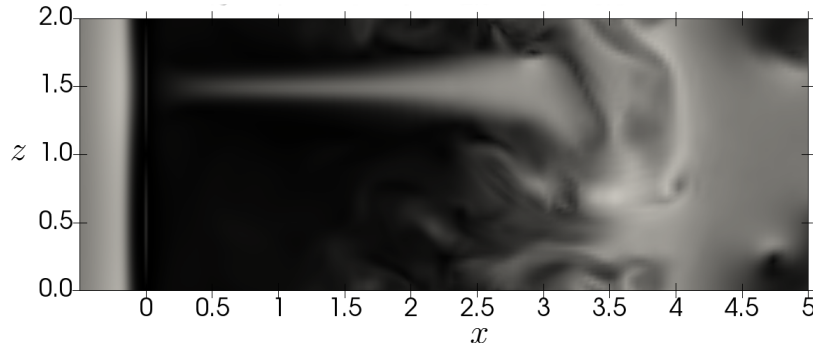
Figure 3.15: velocity magnitude $\in [0, 1.534]$ colour map at y-plane= 0.5

Reynolds stress is a reasonable measure of vortical activity in the wake of circular cylinder. It is speculated that boundary layer thickness at the maximum suction
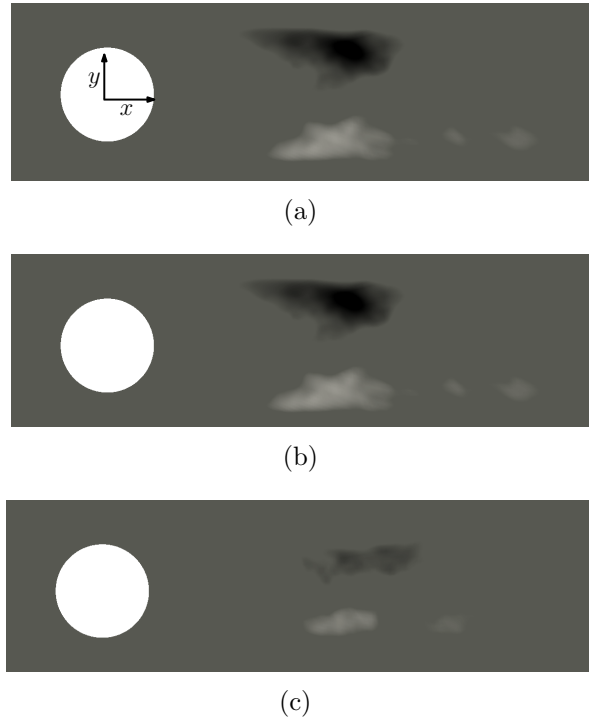
Figure 3.16: Reynolds stress $\langle u'v' \rangle \in [-0.09917, 0.1085]$ behind circular cylinder at (a) $z = 0.5D$, (b) $z = 1D$, and (c) $z = 1.5D$.

point is significantly reduced which disrupts the roll-up process of shear layer in the near wake. This results in a variation of Reynolds stress along the span in the near wake as show in fig 3.16. The fig 3.16 shows the distribution of $\langle u'v' \rangle$ at the maximum blowing and maximum suction point. $\langle u'v' \rangle$ at maximum suction location shows relatively weak signatures of vortical activity than maximum blowing location. Similarly, pressure recovery at the maximum suction point is expected to be higher than the maximum blowing point.

The mechanism of drag reduction for PSD at $f_e = f_{\mathrm{vK}}$ remains essentially the same as that for SDTI forcing, nevertheless, the percentage of drag reduction is relatively small than SDTI forcing. The locations of maximum blowing and suction alternatively change between $z = 0.5D$ and $1.5D$ leading to the distortion of the vortex shedding process in the near wake which results in drag reduction and delay of vortex formation downstream of the cylinder base. Fig 3.17 shows the contours of instantaneous spanwise vorticity in a crossflow plane (y, z) at $x = 0.5D$ for PSD forcing at $f_e = f_{\mathrm{vK}}$ at the instant of maximum suction at $z = 1.5D$. The disruption of shear layer roll-up process in the vicinity of cylinder wall together with the appearance of higher velocity region close to $z = 1.5D$ is evident, confirming the mechanism of drag reduction as described earlier in SDTI forcing. At the instant of maximum

64

suction at $z = 0.5D$, the whole process is repeated at the spanwise location $z = 0.5D$. The three-dimensional distortion of shear layer for PSD forcing at $f_e = 2f_{vK}$ is significantly smaller compared to PSD forcing at $f_e = f_{vK}$ which seems to be the main reason for negligible drag reduction for PSD actuation at $f_e = 2f_{vK}$. In contrast to that, drag and lift fluctuation are increased significantly for PSD forcing at $f_e = 4f_{vK}$ where vortex is formed much closer to the base of the circular cylinder with the corresponding higher suction pressure. It is speculated that forcing frequency excites the inherent shear layer instability which induces higher suction due to the presence of large number of small scale vortices. These small scale vortices might enhance the shear layer roll-up process resulting in the vortex formation much closer to the cylinder base.
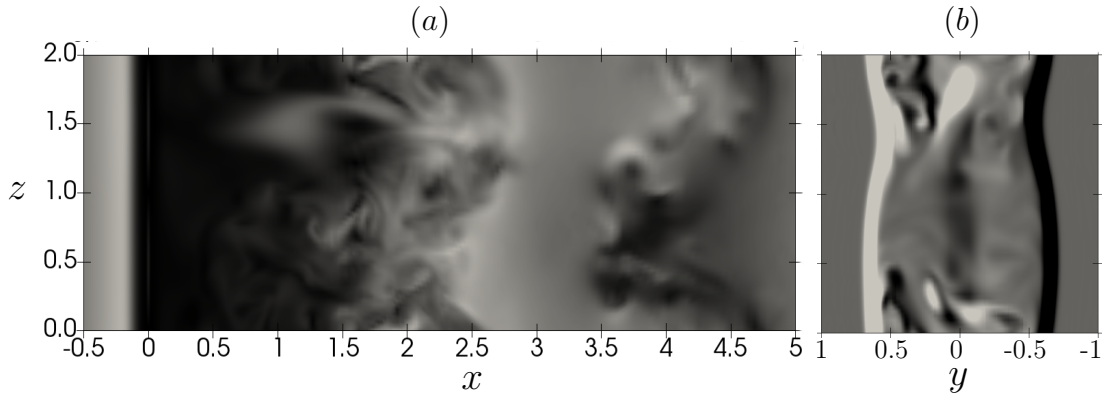
Figure 3.17: Instantaneous flow features behind circular cylinder for PSD forcing at maximum suction at $z = 1.5$. (a) contours of instantaneous spanwise vorticity in a crossflow plane at $x = 0.5D$, (b) contours of instantaneous velocity magnitude in a (x, z)-plane at $y = 0.5D$

In the last AFC case, forcing is applied in the form of sinusoids emanating from the top and bottom walls of the cylinder and traveling oppositely in the spanwise direction. Again, the drag reduction and lift fluctuation attenuation is driven by the same mechanism, *i.e.* delay of the vortex formation in the downstream direction due to the disruption of shear layers evolution right behind the cylinder as shown in fig 3.18. We believe that the maximum suction locations plays a vital role in drag reduction and suppression of lift fluctuation.

It is interesting to notice that Reynolds stress remains, essentially, spanwise independent due to traveling of forcing wave at a constant speed. Non-negligible reduction in drag force has also been observed at a higher constant speed but smaller in magnitude than that of lower constant speed forcing.
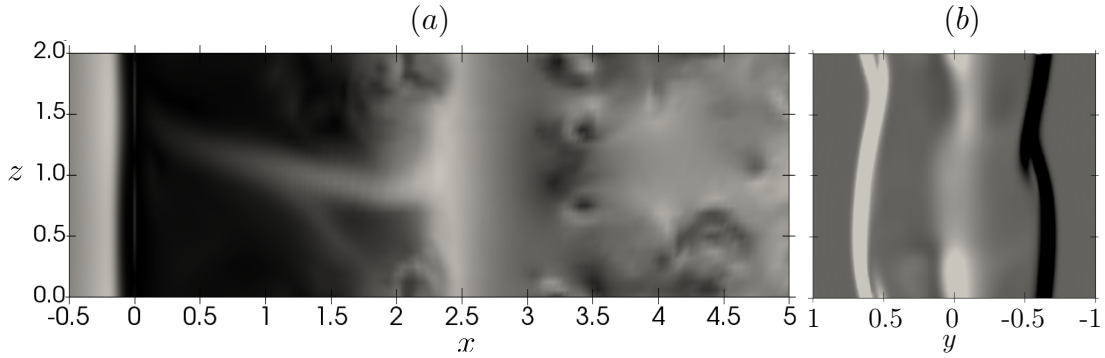
Figure 3.18: Instantaneous flow features behind circular cylinder for STS forcing. (a) contours of instantaneous spanwise vorticity in a crossflow plane at $x = 0.5D$, (b) contours of instantaneous velocity magnitude in a (x, z)-plane at $y = 0.5D$

3.3 Two-dimensional AFC analysis in the context of system dynamics

This section deals with the numerical investigation of an interesting phenomenon observed during the implementation of AFC on two-dimensional flow past circular cylinder at $Re = 2000$. This part constitutes an independent investigation of transition of two-dimensional chaotic flow past circular cylinder to periodic state under the effect of AFC.

Dynamics of the two-dimensional flow past circular cylinder under in-phase and anti-phase actuation (forcing phase-difference corresponds to 180 degree), and the effect of forcing frequency and forcing amplitude, in both configurations, is sought at $Re = 2000$. Same slot positions as that for three-dimensional cases, have been adopted for in-phase and out-of-phase actuation configurations with Gaussian jet profile truncated at $\pm 1.8\zeta$, where ζ is standard deviation, with momentum coefficient C_μ=0.0015-0.22 for out-stroke jet cycle. The forcing frequency was varied from one to 4 times the natural vortex shedding frequency, and the oscillation amplitude from $A = 0.1u_0$ to $1.2u_0$. The actuation jet profiles from the top and bottom slots are given by U_{xy} in eq-(3.1).

The 5484 plane elements has been employed, and mesh density is increased in the vicinity of jet slots. The first cell height is kept below y^+=1 (wall units). Next, we investigate the results obtained from two-dimensional parametric analysis with AFC implemented.

3.3.1 Dynamics of a special case with actuation frequency $(f_e = 2f_{\text{vK}})$

The dynamics of two-dimensional flow past cylinder cylinder at $Re = 2000$ is governed by mild chaos. The controlled case with $f_e = 2f_{\text{vK}}$ displays very interesting scenario as forcing amplitude is quasi statically increased: dynamics is dominated by chaos at low values of A, and then beyond a critical value, system undergoes period doubling cascade which finally saturates at perfectly periodic state. The determination of critical points for period doubling cascade would require extravagant amount of computational resources and time, therefore, main features of this particular scenario have been reported in this work.

3.3.1.1 Chaos

The flow exhibits chaos for the two-dimensional uncontrolled case and the controlled cases at low values of forcing amplitude having forcing frequency f_{vK}, and it dominates dynamics over a wide range of forcing amplitude. Figure 3.19 shows the bifurcation diagram of the controlled case with forcing frequency f_{vK} as the A is increased. In the current investigation, chaotic dynamics of the controlled case has been found for $A < 0.5u_0$. The critical point for the onset of period doubling cascade has not been investigated.

Figure 3.20(a) indicates the dynamics of the baseline case projected on the (u,C_l) and (v,C_l) planes, where u and v are streamwise and crossflow velocity components at (0.2D, 0.5D) in the flow domain. The same location for the velocity components has been used in the study of dynamical behaviour for the rest of the analysis. Poincaré map is applied to analyze the dynamics which clearly represents the presence of mild chaos, as the open circles are clustered in a relatively small region of phase space. A haphazard distribution of open circle filling entire phase space would represent higher degree of chaos. Chaotic behaviour can also been observed from the spectrum of C_l, where highest spectral peak corresponds to the natural vortex shedding frequency.

Similar chaotic dynamics can also be seen for the controlled case in figure 3.20(b) with $A = 0.3u_0$ with the fact the randomness of the flow trajectories has now been increased than two-dimensional uncontrolled case.

3.3.1.2 Period doubling cascade

Flow topology behind circular cylinder changes somewhere between $0.5u_0 < A < 0.55u_0]$ and undergoes period doubling cascade. we observed period-4 solution for the
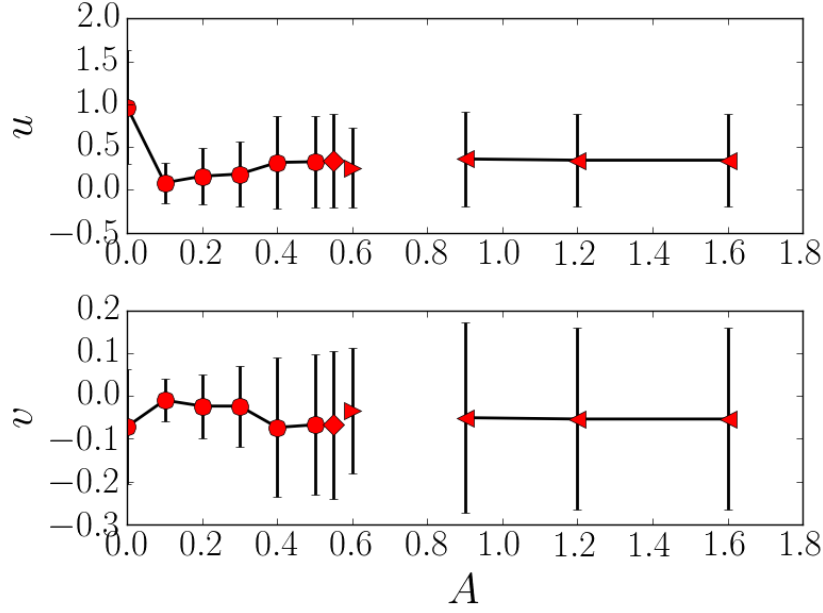
Figure 3.19: Bifurcation diagram of the controlled case with actuation frequency f_{vK}. The vertical velocity component (top) and the horizontal velocity component (bottom) at $(0.2D, 0.5D)$ as a function of A. Different symbols represent chaotic solution (open circles), period-4 orbits (open diamonds), period-2 orbit (right triangle), and the periodic solutions (left triangles). The vertical bars represent fluctuation amplitude.

AFC system where four fixed points appear and each having a period four times the fundamental period corresponding to fundamental frequency. Figure 3.21(a) demonstrates the dynamics of the period-4 case projected on the (u, C_l) and (v, C_l) planes, where 4 open circles indicate four fixed points in such a way that any given solution is repeated after going through the rest of the fixed points. Poincaré maps is very useful to show the continuous-time dynamics in discrete form: periodic orbits in continuous dynamics transform into discrete points. The flow pattern behind circular cylinder corresponding to fixed points has been shown in the figure 3.22. These snapshots have been taken at four instants evenly spaced along the time corresponding to four solutions at the four different fixed points. The first snapshot corresponds to the solution at the Poincaré section defined by $u^P = 1.2$ corresponding to opencircle and the second vorticity field corresponds to second fixed point shown by diamond in the figure 3.22. Similarly third and fourth figures display the flow topology at Poincaré crossings shown by left and right triangles, respectively. The dynamics is repeated with a period four times the fundamental period.

The spectrum of the period-4 case has been shown in fig 3.21(a) by the modulus of the Fourier coefficient $|\hat{C}_l|$ obtained from the Fourier transform of the corresponding
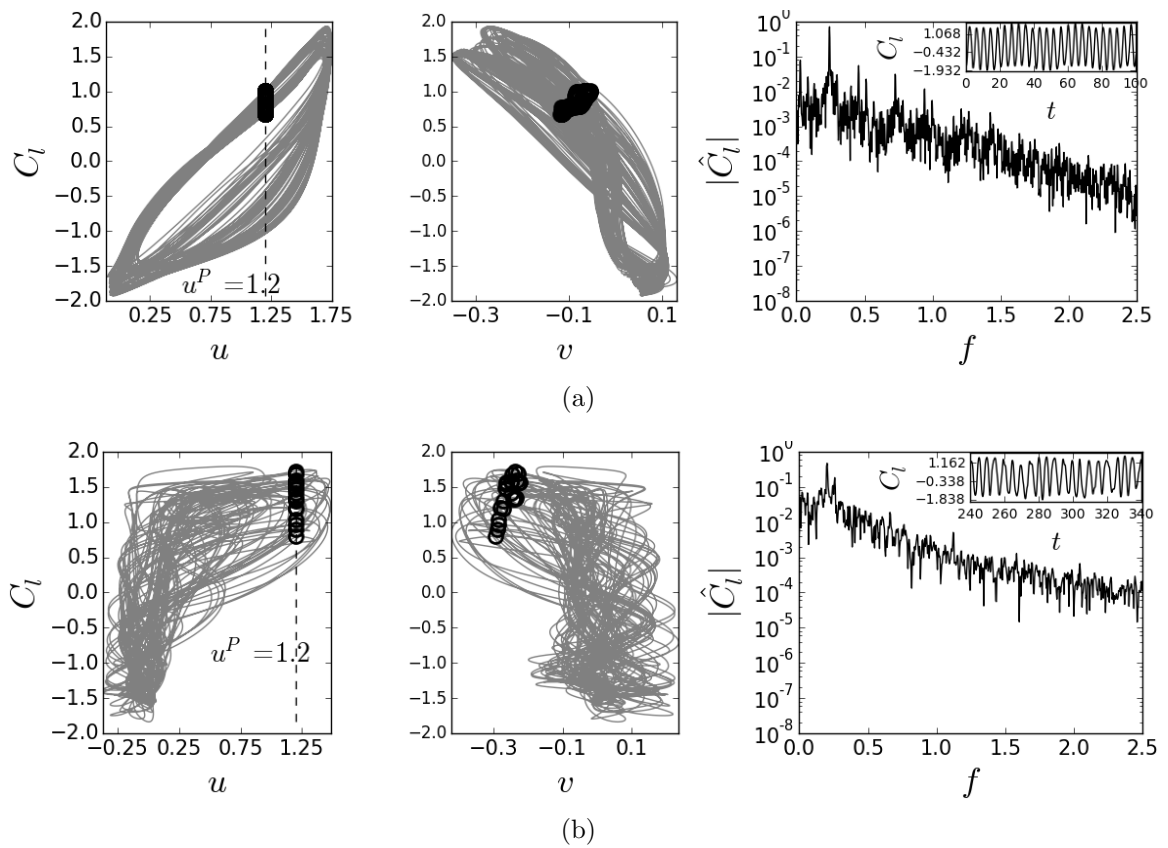
Figure 3.20: Chaotic dynamics of two-dimensional uncontrolled and controlled cases at $Re = 2000$ along with phase map projection on the (u,C_l) and (v,C_l) planes. The open circles denote the fixed point of the Poincaré map defined by $u^P = 1.2$ and $\dot{u}$. spectrum $|\hat{C}_l|$ of the C_l are indicated on the right figures with the corresponding time series in the insets. a) uncontrolled case and b) AFC case with $A = 0.3u_0$

69

C_l time series where several peaks to the left of the highest peak can also be spotted which corresponds to the first, second and third subharmonics of the fundamental frequency whereas highest peak corresponds to the fundamental frequency. These three subharmonics are the characteristics of the period-4 orbit. Period-4 can be spotted by a diamond symbol in the bifurcation diagram. With further increase of forcing amplitude results the transition of dynamics from period-4 to period-2 orbit when projected on the phase plane (u, C_l) and (v, C_l). Now, flow topology repeats itself after twice the period of fundamental period as shown in fig 3.21(b) and fig 3.21(c)

3.4   Conclusions

AFC in the form of blowing and suction from the top and bottom slots of circular cylinder is implemented at $Re = 2000$ to improve aerodynamics performance. Parametric exploration is sought to find the optimal forcing wavelength and forcing amplitude using in-phase spanwise-dependent time-independent forcing. Unsteadiness is investigated by time-periodic spanwise dependent forcing and spanwise traveling sinusoids with variable speed. Aerodynamic drag reduction and lift fluctuation attenuation is found largest for SDTI followed by STS cases with forcing frequencies $0.5f_e$ and f_e, respectively, and finally for PSD controlled case with actuation frequency f_{vK}. It is observed that applied forcing induces spanwise distortion of shear layer development which effects the vortex roll-up process locally in the near wake that causes the vortex formation to occur further downstream and allows pressure to recover in the near wake, thus reducing drag and lift fluctuations. However, PSD forcing with $4f_{vK}$ enhances vortex shedding and drag coefficient which could be an ideal candidate for the energy harvesting applications.
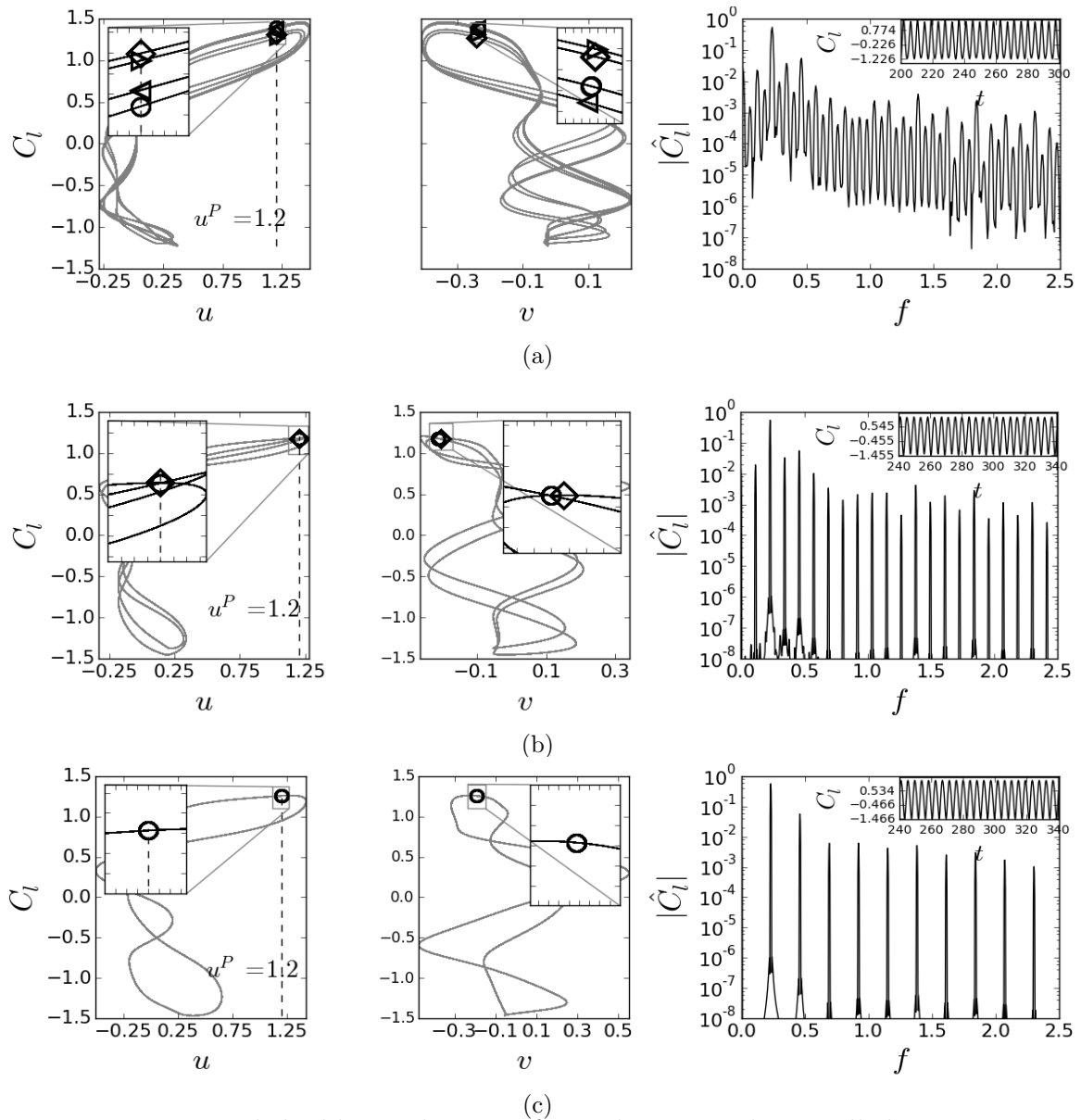
Figure 3.21: Period doubling solutions of two-dimensional controlled case at $Re = 2000$ explained by phase map projection on the (u,C_l), (v,C_l) planes, and spectrum $|\hat{C}_l|$ of the C_l time series. The symbols denote the fixed points of the Poincaré map defined by $u^P = 1.2$ and $\dot{u}$. (a) period-4 solutions (b) period-2 solutions and (c) periodic solution
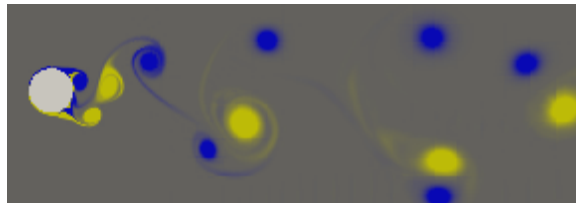
(a)
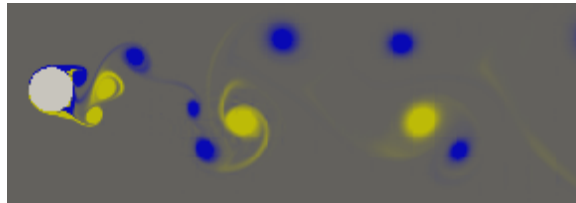
(b)
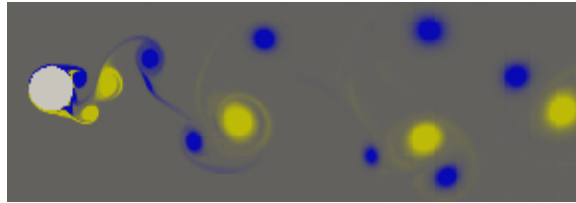
(c)
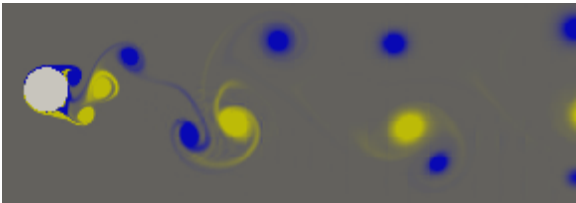
(d)

Figure 3.22: Spanwise-vorticity field evolution ($\omega_z = [-5, 5]$) of the period-4 orbit evenly spaced along the full period of third subharmonic of fundamental frequency. snapshots taken at instant when flow crosses the Poincaré map, defined by $u^P = 1.2$ and $\dot{u} > 0$, through fixed points sequentially (top to bottom in this figure) indicated by open circle, diamond, left triangle, and right triangle, respectively

Chapter 4

Time dependence of flow inside laminar fluidic oscillator

In the previous chapter, we investigated different flow control techniques in order to enhance aerodynamic performance of flow past bluff bodies. The flow over a circular cylinder can be forced via flow actuators in practical situations, therefore, we will focus our attention in this chapter to one such device feasible for the practical implementation of AFC.

4.1   Introduction

Researches [87, 86] have been exploring various ways of flow manipulation around objects immersed in fluid to enhance aerodynamic performance and system efficiency. Substantial development has been witnessed in the Active flow control (AFC) field following the experiments of Prandtl – using suction as a control mechanism to postpone flow separation on a circular cylinder.

In AFC, energy is injected to the mean flow through actuator in various ways to achieve control authority. Flow control actuators were categorized into following types [18]: fluidic, moving object/surface, plasma, and others (e.g. electromagnetic, magneto-hydrodynamic etc). Fluidic actuators control the flow through addition/subtraction of fluid in the vicinity of solid walls. They have been further categorized into zero-net-mass-flux (ZNMF) [108] and non-ZNMF actuators as described in the main introduction section. Morphing surface [109], vibrating flaps [110, 2], and rotating surface [111] etc are prominent examples of moving surface/object actuators. Plasma actuators [112] have gained much attention of the scientific community in the recent years due to their solid-state nature and quick response time.
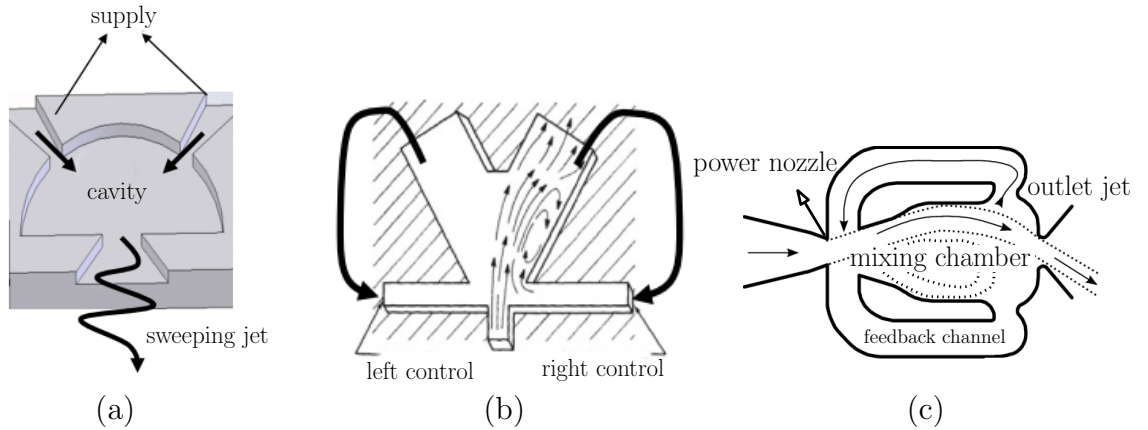
Figure 4.1: Different type of fluidic oscillators. (a) feedback free fluidic oscillator [16], (b) single feedback channel fluidic oscillator [16] and, (c) two-feedback channels fluidic oscillator.

While flow control actuators have shown higher flow control efficiency in numerical/experimental studies [18], there are still challenges for the integration of these devices into the actual systems. Operating voltages, supporting complex electronic systems, and control mechanisms such as surface motion in some cases limit the incorporation of these device into the actual systems. Ideally, a real system would demand lower intake-power, smaller air supply components, electromagnetic interference free actuators, yet simple, reliable, maintenance free, and able to function under harsh conditions such as rain, snow, ice, dust and debris impact, high temperatures, high levels of vibrations etc.

Fluidic oscillators are the ones which seem to meet these criteria, and huge number of patents signify their importance. Despite large scatter of these devices, they can be broadly classified into three types: feedback free [33], single feedback channel, and two feedback channel oscillators as shown in figure 4.1. In a feedback free actuator, fluid is delivered through two inlet ports into main chamber where incoming fluid streams interact with each other. Due to the design of the geometry and inherent fluid flow instabilities, a sweeping jet is generated at the output port of this device as shown in fig 4.1(a).

In an experimental investigation using pressure sensitive paint (PSP), [113] observed that the interaction of the incoming power streams within the mixing (or interaction) chamber results in the formation of a Kelvin-Helmholtz-unstable shear layer. The ensuing complex interaction of counter-rotating vortices that form at either side of the shear layer is then exploited to generate a sweeping jet at the exit of the device. [?] studied a micro-jet-interaction fluidic oscillator in order to characterize the rela-

74

tion between power supply rate and output oscillation frequency from the standpoint of potential applications. The irregular trends they observed, including a kink seemed to indicate that distinct driving mechanism might be at play depending on the flow regime considered. As a matter of fact, three different jet oscillation mechanisms were later revealed using particle image velocimetry (PIV) with a refractive-index matched sodium-iodide solution [114]. The corresponding flow regimes were named *weak*, *transitional* and *high* flow rate regimes. A detailed analysis in the *low* regime showed that the jet bifurcation regulates the transfer of kinetic energy between the interacting streams. Phase averaging unveiled the presence of four vortices, two dome and two side vortices. The former, which appear and disappear alternatively along a full cycle, were shown responsible for the jet bifurcation, while the latter vortices, present all along, alternatively grew and shrank thus regulating the exit jet oscillation as shown in figure 4.2.
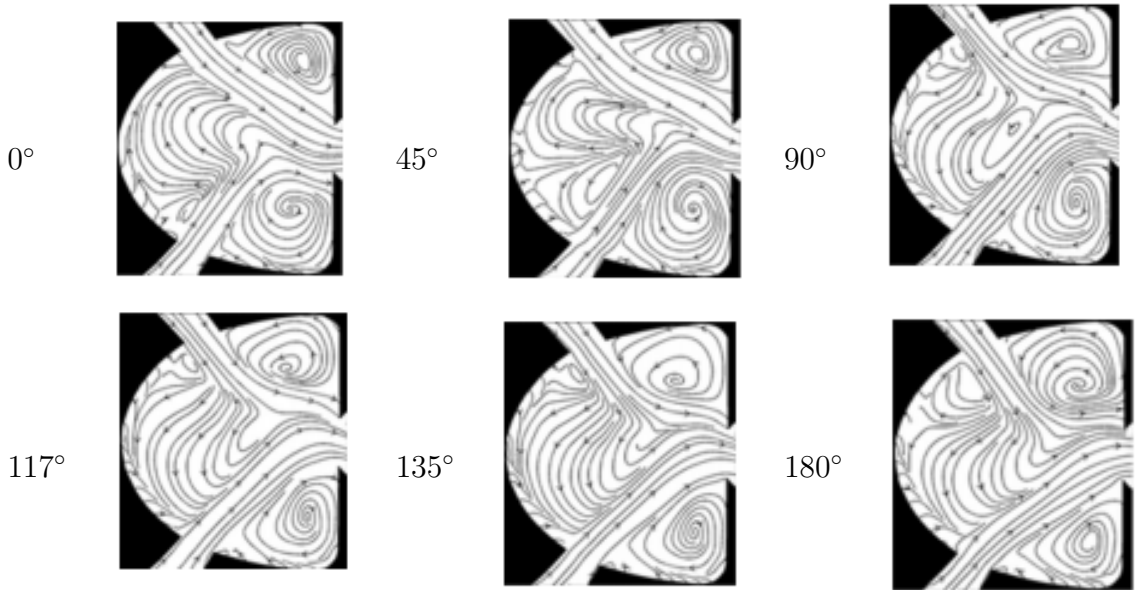
Figure 4.2: Flow physics during half cycle of oscillation [17]. At $\theta = 0$, Upper jets core is connected to the exiting jet while the lower jet is bifurcated. Size of the lower dome vortex grows as it is fed by the left side of lower shear layer at $\theta = 45$. At $\theta = 90$, lower dome vortex approaches the upper jet and initiates its bifurcation. Lower dome vortex collides with the saddle point and bursts at $\theta = 117$. Lower jet core is connected to the exit jet and onset of an upper dome vortex at $\theta = 135$, which further grows in size at $\theta = 180$.

A typical single feedback loop FO is shown in fig 4.1(b). The jet while entering the device tends to bend to one of the side walls due to intrinsic instabilities, the so-called Coanda effect. The Coanda effect increases the fluid entrainment along

the jet-attached-wall side. The results in pressure reduction which induces pressure gradient across the jet so that pressure is lower on the jet-inclined side compared to opposite side. Resultantly, a compression wave from the high pressure side and rarefaction wave from the low pressure side travel to the opposite side through the feedback channel which drives the flow to move from high pressure side to lower pressure side. his flow grows the vortex or separation bubble in the low pressure area and finally win the stabilizing Coanda Effect and the jet detaches from the wall. After passing through the central axis, the jet is attached to the opposite side of the device and this process repeats.

Two feedback channel fluidic oscillators base their operation on the alternate attachment of a single input flow stream, fed through the so-called power nozzle, unto one or the other of the internal walls of the plenum (or mixing) chamber through the Coandă effect. The underlying mechanism relies on the bi-stability of two mutually-symmetric wall-attached (to either one of the two walls) flow configurations (or states) that are alternatively destabilised by the timely diversion of momentum through purposely-designed feed-back channels that push the flow stream towards the opposite wall. The alternative bending of the stream as it wanders from one wall to the other results in the sweeping motion of the outcoming jet beyond the exit nozzle. Before the introduction of feedback channels, the switching mechanism of the power stream between the adjacent walls was driven by the application of a transverse disturbance in the form of a pressure pulse [115] or a fluid injecion [116], such that the oscillation did not qualify as self-sustained. Nowadays, a typical curved-sweeping-jet oscillator replaces the external momentum source as switching mechanism by an adequate diversion of ouput momentum through purposefully designed feedback channels. The power stream, attached to either one of the side walls by the action of the Coandă effect, is made to impinge quasi-orthogonally on the wall that leads to the exit nozzle throat. As a result, part of the momentum is directed towards the feedback channel on the side to which the stream is bent. This momentum is reintroduced back transversally at the exit of the power nozzle, which pushes the power stream away from the wall to which it is attached. As the recirculation bubble grows the feedback channel is blocked and the power stream left at the mercy of the Coandă effect from the opposite wall, which captures it, thus completing the full sweep of the jet. The process then repeats symmetrically. The alternative sweeping of the power stream leads to a self-induced and self-sustaining oscillating jet at exit [117] in complete absence of moving parts, which renders these devices very robust and reliable against mechanical failure. Mass injection has been long thought the main

source of momentum feedback driving the jet sweeping for these type of devices, as time resolved pressure and PIV measurements [118] seem to reflect. [119] have nevertheless shown that static pressure may become the main feedback momentum source underlying the sweeping mechanism under certain circumstances.

Fluidic oscillators are devices which manipulate flow field by the injection of fluid as pulsating-jet/spatially-oscillating-jet into the mean flow. The fluidic oscillator which produces pulsating jets are referred to as fluidic diverters [120] in literature. The jet from the chamber is directed to two channels separated by a splitter. Anti-phase-pulsating jets from the output ports are produced at the exit of these channels. These devices have been used in a variety of applications such as combustion control [121, 122, 123], separation control in compressors stator vane separation control [124], generation of microbubles [125] in bioreactors. Other type of actuators which produces spatially oscillating jets at the device output port have been extensively studied in the literature [16]. Historically, these devices have been used for diverse applications such as sensing, logic, nozzles for windshield water distribution, sprinklers, shower heads for their robustness and reliability and non-vulnerability to electromagnetic interference. Flip-flop nozzles [126, 127] are the known earliest example of sweeping jets used for flow control to enhance mixing performance. These sweeping jet devices have been extensively studied in the recent years for the active flow control [128, 129] , noise [130, 131], and combustion control [121] applications. This technology has demonstrated significant improvement in aerodynamic performance in the field of separation control for streamlined [132] and bluff bodies [133, 134, 135]. The research covered two-dimensional airfoils [128, 129, 136, 137] with significant improvement in performance indicators, and complex three-dimensional models [128] and swept wings [138, 139, 140]. The use of fluidic oscillators is motivated by an anticipation that these devices are more efficient than the steady jets, and require less mass flow. Because of the sweeping motion, their lateral impact area is increased and, therefore, a larger spacing between adjacent actuators leads to the need for fewer actuators. Even though more assessment of system efficiency is required, initial studies (e.g. [141]) support the claim of greater efficiency with fluidic oscillators. Implementation of an array of fluidic oscillators on the control surfaces yield reasonable increase in the side force [142, 143]. This technology is proven to be equally viable for the bluff bodies. The potential solution for the requirement of less mass-flow/supply-pressure could be realized by using modulated fluidic oscillators [144, 145]. These devices are modulated at the lower frequency and could be triggered for the given fraction of a duty cycle.
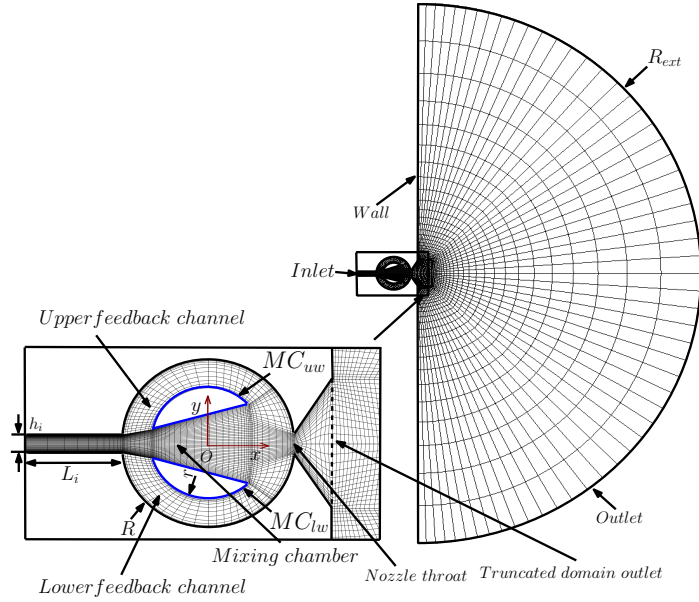
Figure 4.3: Computational domain and mesh. The inset shows a detail of the mesh inside the fluidic oscillator. The streamwise-crossflow plane is discretised in high-order quadrilateral spectral elements.

Even though literature is full of variety of fluidic oscillators, there is hardly any study outlining the critical values of mass flow rate/Re for the onset of time-dependent behavior inside two-feedback channel fluidic oscillator. The proprietary nature of these device limit research community to carry out fundamental study of internal dynamics. However, there are studies describing the onset of time-dependence behavior inside traditional two-feedback channel oscillator [146] Critical Reynolds number for the onset of primary instability is not reported, instead a range is given within which bifurcation might have occurred. In the present study, the time dependence has been investigated for the novel designed fluidic oscillator.

4.2 Problem formulation and numerical approach

The incompressible viscous flow inside the fluidic oscillator is governed by the Navier-Stokes equations given by Eq. 2.1, nondimensionalized by inlet channel width (h_i), fluid kinematic viscosity (ν) and inlet velocity (U). The velocity profile at the inlet channel has a plane Poiseuille profile such that mean velocity along the streamwise direction at the inlet channel is unity, given as

$$u(y) = \tfrac{3}{2}(1 - (\tfrac{y}{h_i})^2), \tag{4.1}$$

Re	K	P	St	$\bar{C}_L$	C'_L	$\bar{C}_D$	C'_D
100	4694	4	0.0128	-0.855	0.533	0.084	0.072
-	4694	6	0.0128	-0.862	0.538	0.085	0.073
-	4694	8	0.0128	-0.866	0.544	0.086	0.074
-	6476	4	0.0129	-0.856	0.534	0.084	0.073
-	6476	6	0.0128	-0.860	0.538	0.085	0.073

Table 4.1: Mesh and aerodynamics parameters of fluidic oscillator

For simplicity in non-dimensionalization, the inlet and nozzle throat widths were set to unity. The inner (r) and outer radii (R) are 3 and 4.5, respectively. The velocity profile at the inlet-channel's exit has been computed for various channel's lengths and the profile was found to converge for an inlet-channel-length of $L_i = 5$, and the external domain is extended to $R_{ext} = 75h_i$ to consider the outside effect on the fluidic oscillator's cavity dynamics.

The domain in the streamwise-crossflow plane takes $(x, y) \in [-9.5, 81.5] \times [-75, 75]$ (see figure 4.3) with the origin located at the center of the fluidic oscillator as shown by the O in figure 4.3.

The boundary conditions are no-slip at the walls $\mathbf{u}_w = 0$ and homogeneous Neumann at the downstream boundary $(\nabla \mathbf{u} \cdot \hat{\mathbf{n}}) = 0$. For pressure, high order homogeneous Neumann boundary conditions are applied everywhere except for the downstream boundary, where homogeneous Dirichlet conditions $p = 0$ are imposed.

Resolution study has been performed to find the ideal mesh for the optimal use of computational resources. Two different meshes were selected and their in-plane polynomial expansions (P) were varied to see their effects on the flow parameters i.e. St, $\bar{C}_L$, C'_L, $\bar{C}_D$, and C'_D, where St is Strouhal number, $\bar{C}_L$ is the time-averaged lift coefficient, C'_L is the rms of lift coefficient, $\bar{C}_D$ is the time-averaged drag coefficient and C'_D is the rms drag coefficient as show in table 4.1, computed on mixing chamber upper wedge (MC_{uw}) as depicted in fig 4.3.

Incompressible Navier-Stokes solver of the spectral/finite element package Nektar++ [82] has been employed for complete resolution of the flow. Spatial discretisations of 4694 high-order quadrilateral elements (K) have been used in the streamwise-crossflow plane, with Lagrange polynomial expansions up to order $P - 1 = 5$. Normal wall units i.e. y^+ for the mesh employed were $\leqslant 0.27$. A continuous Galerkin projection has been enforced across element boundaries. A particularly refined mesh has been set up in the vicinity of the crucial area such as mixing chamber, inlet and outlet of feedback channels, and outlet nozzle, as shown in the inset of figure 4.3, to properly

resolve complex internal dynamics. The skew-symmetric form of the advection term has been adopted for discrete operators in order to preserve their continuous counterpart's symmetric properties. A second order velocity-correction splitting scheme with a time-step ($\Delta t = 0.005$) was used to provide sufficient time-integration accuracy.

Three different cases have been considered in the present study regarding spatial dimensions: two-dimensional case with semi-circular buffer-zone ($2D_f$) is used for all analyses in this work and shown in fig 4.3 (numerical simulations carried out in this work refer to $2D_f$-case else otherwise stated); two-dimensional case with truncated buffer-zone ($2D_t$) shown by dotted line in the inset of fig 4.3; and the three-dimensional case with streamwise-crossflow dimensions as that of $2D_f$-case but with spanwise periodic extent of $L_z = 14h_i$. 20 Fourier modes have been employed in the homogeneous direction which yielded $O(6)$ modal energy decay at $Re = 88$. This spanwise domain length is chosen following $2.5D$ stability analysis as explained in § 4.3.1

4.2.1 Analysis of flow dynamics of fluidic oscillator

The flow dynamics inside the FO is governed by a steady state at a sufficiently low Re i.e. $Re < 75.745$. This simple flow topology transitions into a much complex flow state as the Re is increased, and the two-dimensional stable steady state solution undergoes a series of bifurcations starting from the inception of time-dependent flow in the presence of outside chaos. In this section, we present descriptions of the dynamics of the various flow regimes that were observed along the initial part of the bifurcation cascade. $2D_f$, $2D_t$ and three dimensional cases have been employed to investigate the primary flow transition, especially $2D_t$-case is used for comparison with $2D_f$ and the three-dimensional cases in order to assess the effect of outside chaos on the flow dynamics and the critical point in the latter cases. However, seconds flow transition along its route to chaotic state is analyzed by $2D_f$ and $2D_t$ cases.

Fig 4.4 represents the stable steady state of flow inside FO at $Re = 75$. The flow in the inlet channel has a plane Poiseuille profile which enters the mixing chamber and leaves the outlet nozzle without being deflected. The jet outside the FO retains its direction, and diffuses slowly into the external atmosphere.

The flow topology inside the FO is dominated by two stationary vortices formed close to the exit of mixing chamber, located symmetrically about $y = 0$ axis. The inlet jet happens to be stable enough to remain insensitive to the so-called Coanda effect. Similarly, two recirculation regions with opposite sense of rotation are present in the
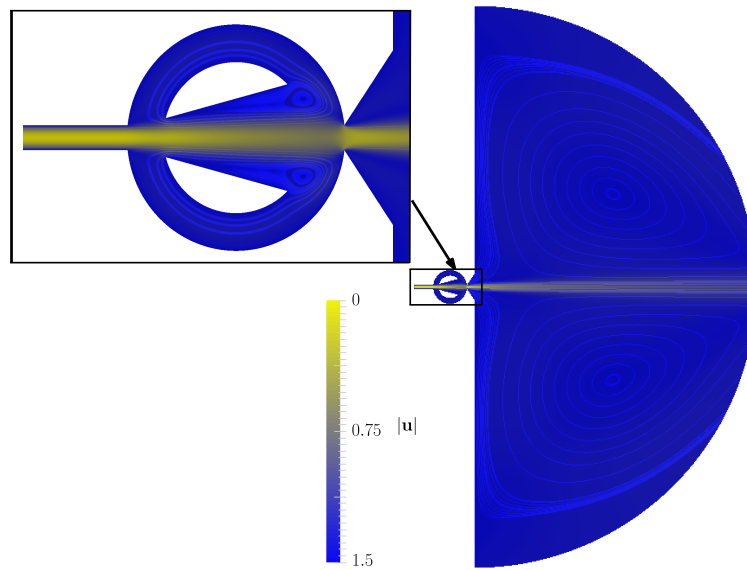
Figure 4.4: Color map for the velocity magnitude for two-dimensional case, together with streamlines at $Re = 75$, $|\mathbf{u}| \in [\mathbf{0}, \mathbf{1.5}]$

external domain which are the manifestation of the finite domain jet entrainment effect in a steady atmosphere as show in figure 4.4.

Fig 4.5(b) illustrates the spectrum $|\hat{C}_l|$ of the $C_l(t)$ time series shown in the inset, where C_l is the combined-lift coefficient calculated on the upper-mixing-chamber-wedge (MC_{uw}) and the lower-mixing-chamber-wedge (MC_{lw}) as indicated in fig **??**, for $2D_f, 2D_t$ and the three-dimensional cases at $Re = 88$. An indication of clear peaks at the fundamental frequency $f = 0.0137$ which corresponds to a time period $T = 73$ time units for $2D_f$ and $2D_t$, represents the existence of a time-dependent flow state inside FO, and the higher energy at the fundamental frequency and the subsequent harmonics indicate nonlinear evolution of the time-dependent solution away from the bifurcation point. Three-dimensional solution at $Re = 88$ registers the first peak at the almost-same frequency (shifted to a little higher frequency) of two-dimensional cases as depicted in the Fig 4.5(b).

The flow inside the mixing chamber cavity features space-time symmetric periodic oscillations, in the presence of outside chaos at $Re = 88$ for two- and three-dimensional cases. Fig 4.5(a) shows the phase map trajectories of the dynamics inside FO mixing chamber through projection on the (u_p, C_l) and (v_p, C_l) planes for $2D_f, 2D_t$ and the three-dimensional case at $Re = 88$, where u_p and v_p are the streamwise and crossflow velocity components registered by the probe located inside the FO at the origin (O). Space-time symmetry of the cavity jet about FO axis is clearly evident from the
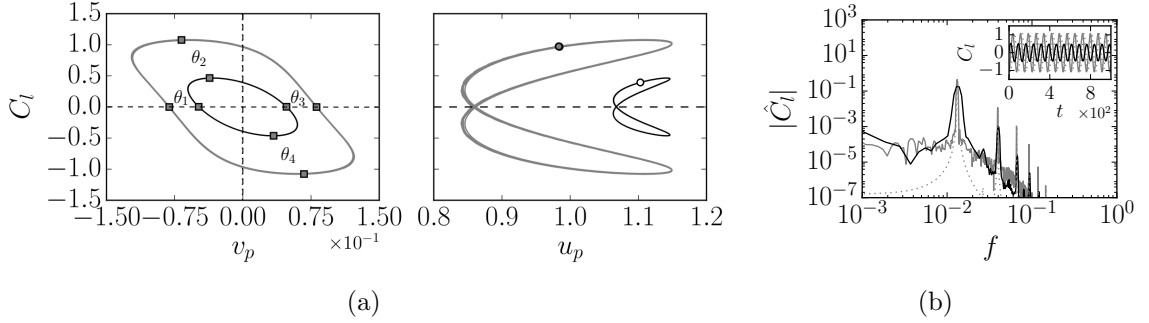
Figure 4.5: Periodic state at $Re = 88$ for $2D_f$, $2D_t$ and the three-dimensional cases, (solid dark line: three-dimensional case, solid grey line: $2D_f$-case, dotted grey line: $2D_t$-case). (a) Phase map projection on the (v_p, C_l) and (u_p, C_l) planes. The C_l and u_p, v_p denote the combined-lift-coefficient acting on the MC_{uw} and MC_{lw}, and the streamwise and crossflow velocity components at probe located at O. The circles represent the fixed points of the Poincaré map defined by $v_p = 0, \dot{v}_p > 0$. The squares represent the phase angles calculated from the C_l time series using Hilbert transform: $\theta_1 = 0, \theta_2 = \frac{\pi}{2}, \theta_3 = \pi, \theta_4 = \frac{3\pi}{2}$. (b) Spectrum $|\hat{C}_l|$ of the C_l time-series. The inset shows the time-series of the corresponding cases.
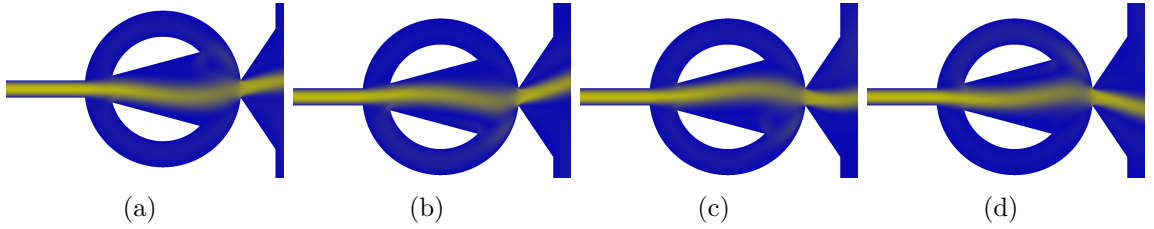
Figure 4.6: Velocity field at the instantaneous phases of the periodic solution for $2D_f$-case at $Re = 88$. (a) $\theta_1=0$, (b) $\theta_2=\frac{\pi}{2}$, (c) $\theta_3=\pi$, and (d) $\theta_4=\frac{3\pi}{2}$. Color codes as fig 4.4

phase map trajectories traced by flow in the (u_p, C_l) phase plane as indicated in the fig 4.5(a) for $2D_f, 2D_t$ and the three-dimensional case.

In order to evaluate the effect of outside chaos on the internal dynamics of FO, a study with $2D_t$-case is undertaken by truncating the external domain of $2D_f$-case at a location shown by dashed line in the inset of fig **??**. It has been observed that the instability inside FO remains unaffected by the removal of external chaos which could be explained by observing remarkably similar cavity-dynamics as that of $2D_f$-case when projected on the (u_p, C_l) and (v_p, C_l) planes as shown in fig 4.5(a). Another important observation in the cavity dynamics of $2D_t$-case is the display of perfectly periodic trend, in contrast to $2D_f$-case and three-dimensional cases- having some degree of pseudo-periodicity which might be linked to the degree of outside chaos. The degree of outside chaos in the internal dynamics for both $2D_f$- and three-dimensional cases is directly related to the thickness of the skewed-8 loop in fig 4.5(a).
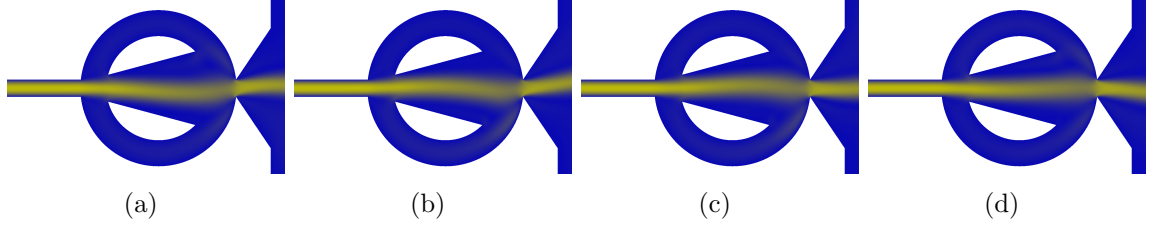
Figure 4.7: Velocity field at the instantaneous phases of the periodic solution for three-dimensional case at $Re = 88$.(a) $\theta_1{=}0$, (b) $\theta_2{=}\frac{\pi}{2}$, (c) $\theta_3{=}\pi$,and (d) $\theta_4{=}\frac{3\pi}{2}$. Color codes as fig 4.4
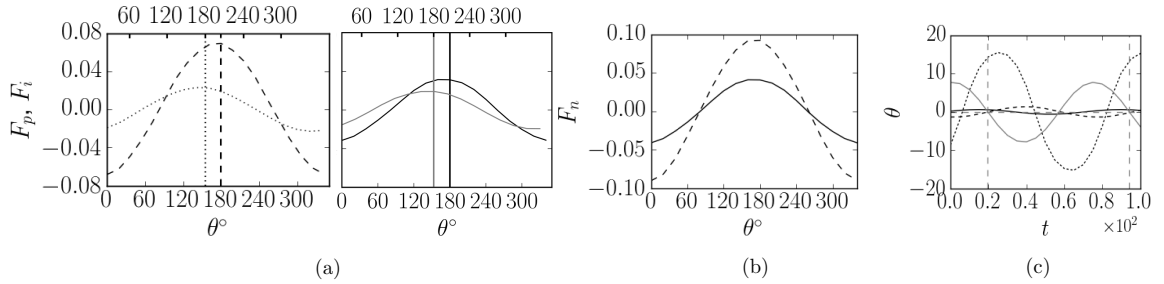
Figure 4.8: Flow characteristics through the feedback channels for $2D_f$ and the three-dimensional case at $Re = 88$: (a) phase averaged pressure (F_p) and inertial forces (F_i) components computed over eight cycles acting on the incoming jet for two- and three-dimensional cases ; (three-dimensional case, solid-dark line: F_p, solid-grey line: F_i), ($2D_f$-case, dashed line: F_p, dotted line: F_i). The bottom and top x-axes represent $\theta°$ for F_p and F_i, respectively, and the gap between vertical lines represent phase difference between F_i and F_p for $2D_f$ and the three-dimensional cases. The line style of vertical lines correspond to the line style of the plots of the corresponding forces. (b) phase-averaged-net-force (F_n) acting on the incoming jet to the mixing chamber, (solid line: three-dimensional case, dashed line: $2D_f$-case). (c) jet deflection angles at the entrance and exit of mixing chamber. Three- dimensional case: (solid-dark line: mixing chamber inlet, solid-grey line: mixing chamber exit), $2D_f$-case: (dashed line: mixing chamber inlet, dotted line: mixing chamber exit). The vertical dash lines represent the time span of one complete cycle.
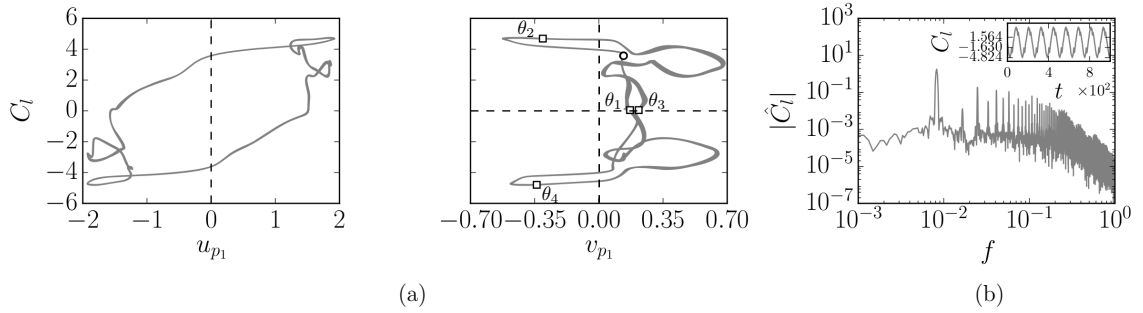
Figure 4.9: Pseudo-periodic state at $Re = 300$ for $2D_f$-case. (a) Phase map projection on the (u_{p_1}, C_l) and (v_{p_1}, C_l) planes. The C_l and u_{p_1}, v_{p_1} denote the combined-lift-coefficient acting on MC_{uw} and MC_{lw}, and difference of the corresponding streamwise and crossflow velocity components at probes located symmetrically about fluidic oscillator axis i.e. $(0, \pm 0.9)$, respectively. The circles represent the fixed points of the Poincaré map defined by $u_{p_1} = 0, \dot{u}_{p_1} > 0$. The squares represent the phase angles calculated from the C_l time series using Hilbert transform: $\theta_1 = 0, \theta_2 = \frac{\pi}{2}, \theta_3 = \pi, \theta_4 = \frac{3\pi}{2}$ (b) Spectrum $|\hat{C}_l|$ of the C_l time-series.

The first fig in fig 4.5(a) represents the flow of trajectories when dynamics inside FO's cavity is projected on the (v_p, C_l) plane. The squares located in the path of the trajectories for all cases under study i.e. the three-dimensional, $2D_f$, and $2D_t$-cases, denote the evenly spaced phases as indicated in the fig 4.5(a). C_l time-series is used to calculate the instantaneous phases via Hilbert transform[13]. The jet incoming to the mixing chamber cavity is already bent towards the MC_{lw} and the outgoing jet leaves the cavity through the nozzle opposite to the vertical direction of the incoming jet, at θ_1. The pressure distribution and shear forces acting on MC_{lw} and MC_{uw} are same in magnitude but opposite in direction, therefore, C_l registers an almost zero value at θ_1 for all cases. However at θ_2, in fig 4.6(b) and fig 4.7(b), the incoming jet has moved upward that results in jet impingement at the bottom side of exit region which increases the pressure inside the bottom feedback channel and results in maximum C_l for all cases as shown in fig 4.5(a). The next half cycle is symmetric with respect to the FO axis as demonstrated by the antisymmetry of the $\theta_1 = \theta_3$ and $\theta_2 = \theta_4$ both in the fig 4.5(a), and in the figs 4.6 and 4.7.

At $Re = 88$, the jet, while entering the mixing chamber inlet, has already become unstable, and attaches to one of the lateral walls of the mixing chamber through the so-called "Coanda effect". The jet impingement at the exit wall results in the development of a high pressure wave which propagates across the entire fluidic oscillator, and consequently, establishes a pressure differential between the inlet and exit of the feedback channel that results in a mass flow through the feedback channels. This

pressure differential allows a part of fluid to be fed back to the inlet through the feedback channel that then feeds the recirculation region developing between one of the mixing chamber lateral walls and the incoming jet. A pressure differential established between the exit planes of upper and lower feedback channels exerts pressure force on the incoming jet which leads the force due to the mass flow (inertial force), i.e. $\frac{\dot{m}^2}{\rho A}$, where $\dot{m}$ is the mass flow rate, ρ is the fluid density and A is the area at this location, through the feedback channels as illustrated in fig 4.8(a) and (b).

The transported mass to the outlet of feedback channels from the aft region of mixing chamber exerts a momentum force on the incoming jet which is balanced in case of a stable steady jet. However, when the jet is attached to either of the lateral walls, this balance between momentum forces is disturbed. Fig 4.8(a) shows the phase averaged inertial and pressure forces acting on the incoming jet and the vertical dash lines represent $\theta = \pi$ for former forces for $2D_f$ and three-dimensional cases, and the phase difference between these forces is shown by the gap between the respective $\theta = \pi$ vertical dashed lines. The phase difference between the inertial and pressure forces is found to be $\Delta\theta = 25°$ and $\Delta\theta = 27°$ for $2D_f$ and three-dimensional cases, respectively. Another important observation is that the inertial force for $2D_f$ is of the same order for three-dimensional case, however, the pressure force is almost twice for $2D_f$-case than three-dimensional case which is also shown in net force acting on the incoming jet indicated in fig 4.8(b).


(a)   (b)   (c)   (d)
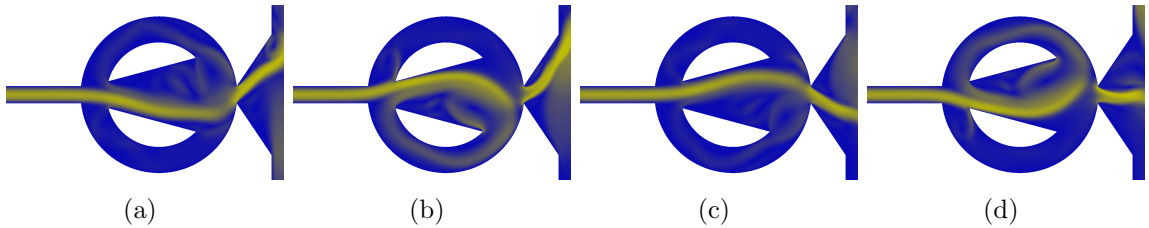
Figure 4.10: Velocity field at instantaneous phases of periodic solution for $2D_f$-case at $Re = 300$.(a) $\theta_1=0$, (b) $\theta_2=\frac{\pi}{2}$, (c) $\theta_3=\pi$,and (d) $\theta_4=\frac{3\pi}{2}$. Color codes as fig 4.4

It would also be interesting to see the phase relationship between the incoming jet to the mixing chamber and the sweeping jet leaving the fluidic oscillator, and their corresponding deflection angles. Probes located at the center of the inlet channel exit and the output nozzle throat have been used to compute the instantaneous jet deflection angles. The jet prescribes a smaller deflection, both at the inlet and exit, for three-dimensional periodic solution as compared to the corresponding two-dimensional solution as shown in fig 4.8(c). The upstream jet has a phase lag of
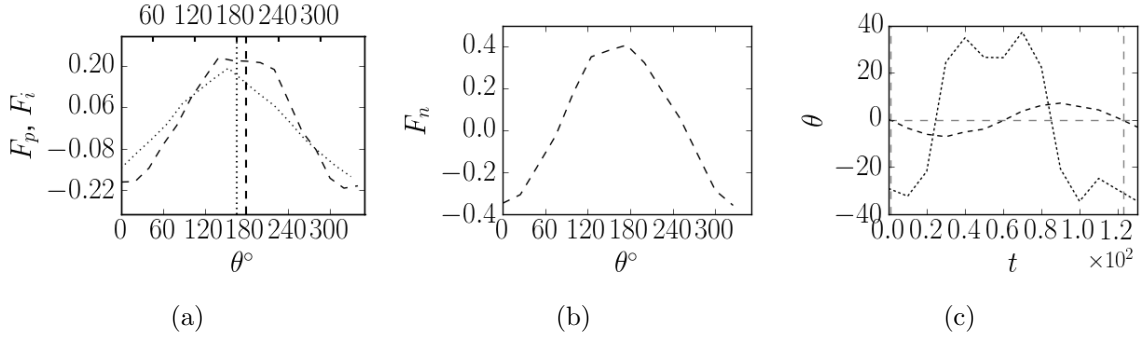
Figure 4.11: Flow characteristics of fluidic oscillator for $2D_f$-case at $Re = 300$. (a) pressure force (F_p) and inertial force (F_i) components acting on the incoming jet, (b) net force (F_n) acting on the incoming jet at the entrance of mixing chamber inlet, (c) jet deflection angle of the incoming jet at mixing chamber inlet and at throat. Line-styles as in fig 4.8 for $2D_f$-case.

$63.85^o \pm 5.85$ and 65.46 ± 3.35 with respect to downstream jet for three-dimensional and two-dimensional cases, respectively.

The two-dimensional solution follows a phase map trajectory symmetrically about FO axis when projected on (u_p, C_l) for $Re < 290$. In contrast to $2D_f$ solution at $Re = 88$, the $2D_f$ solution displays a more complex trajectories when dynamics is projected on the (u_{p_1}, C_l) and (v_{p_1}, C_l) phase planes at $Re = 300$ as shown in fig 4.9(a), where u_{p_1} and v_{p_1} are the difference of the corresponding streamwise and crossflow velocity components at probes located symmetrically about the fluidic oscillator axis i.e. $(0, \pm 0.9)$, respectively. The pseudo periodic solution at $Re = 300$ no longer traces symmetric path in the (v_{p_1}, C_l) plane as shown in fig 4.9(a) which signifies the flow bifurcation from space-time-symmetric periodic state to asymmetric time-dependent state as explained in § 4.3.2. Spectrum $|\hat{C}_l|$ of the $C_l(t)$ is represented in fig 4.9(b), where the dominant peak represents the fundamental frequency $f = 0.0082$ which corresponds to a time period $T = 121.95$. It is interesting to note that the frequency shows a decreasing trend with increase in the Re, which is quite contrary to the fluidic oscillators operating in the turbulent regime.

Velocity fields at evenly divided phases provide us better insight to understand the complex dynamics inside cavity at $Re = 300$ for $2D_f$-case. Incoming jet undergoes higher deflection at $Re = 300$ as compared to two-dimensional and three-dimensional solutions at $Re = 88$ at corresponding phases of 0 and π. The small protrusions of the phase map trajectory in the (v_{p_1}, C_l)-phase plane as demonstrated in fig 4.9(a) are probably due to the presence of small vortices attached to the upper and lower mixing chamber lateral walls at the phases of θ_2 and θ_4, respectively. A striking

86
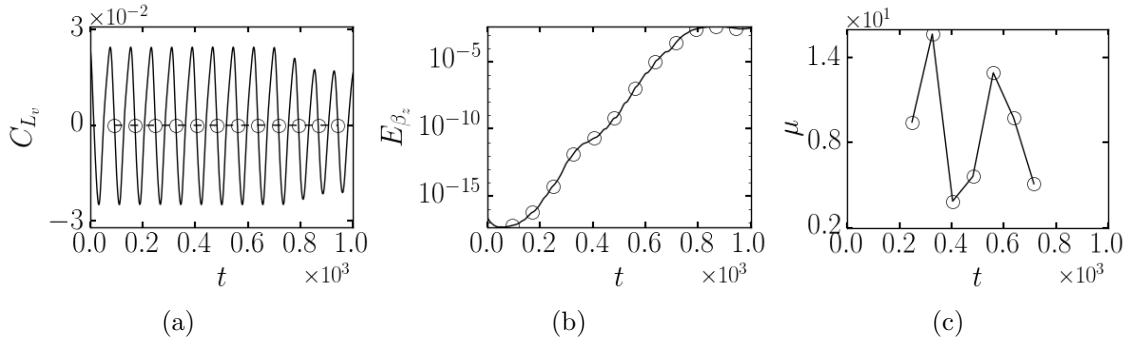
Figure 4.12: Computation of Floquet multiplier from time traces of C_{L_v} time series at $Re = 100$; (a) C_{L_v} time series with Poincaré section defined at phase angle ($\phi = 90\deg \pm 0.1$)(denoted by open circle); (b) linear growth of Fourier mode with $\beta = \frac{2\pi}{13}$; (c) $\mu = \frac{\mathbf{u}^n}{\mathbf{u}^{n-1}}$ computed at each crossing

difference between these two cases, i.e. $2D_f$ solutions at $Re = 88$ and 300, is the direct transportation of fluid from the feedback channels outlet for $Re = 300$ which is not the case for $Re = 88$ at θ_2 and θ_4. It is notable to see that contribution of the pressure and inertial forces to the net force exerted on the entering jet is nearly same as shown in figs 4.11(a) and (b) which is in contrast to net force at $Re = 88$ for $2D_f$-case. A clarification of what determines the relative increase in the inertial force component at $Re = 300$ may be related to the fluidic oscillator geometry at the exit, which somehow manages to promote the mass flow through the inlet of feedback channels with the increase in Re. Also, at this higher Re, external jet sweep angle is almost twice to that at $Re = 88$ for two-dimensional case, however the incoming jet lateral oscillation remains of the same order as illustrated in fig 4.11(c).

4.3 Results

Results of flow inside fluidic oscillator are presented as follows

4.3.1 Pseudo Floquet Stability Analysis

Floquet stability analysis has been the focus of many numerical investigations for the characterization of secondary instability of the circular [43, 85] and square [147] cross-section cylinder time-dependent wake since the pioneering experimental study of [42]. Linear stability analyses have shown remarkable success in the laminar regime, however, nonlinear interactions of competing Fourier Floquet modes hamper the application of these methods at higher Re.

87

(a)　　　　　　　(b)　　　　　　　(c)
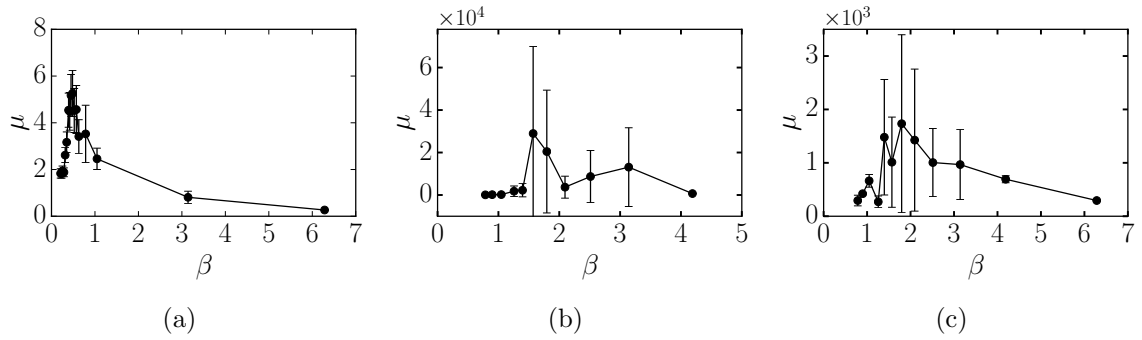
Figure 4.13: Floquet multiplier vs wavenumber ($\beta = \frac{2\pi}{L_z}$) where error bars represent standard deviation in the computation of Floquet multiplier: (a) $Re=100$; (b) $Re=200$ and ; (c) $Re=300$

(a)　　　　　　　　　　　　(b)

Figure 4.14: Vorticity field during the evolution of Fourier mode in the linear regime(a) instantaneous spanwise vorticity field of spanwise mean flow at $Re=100$ in the linear growth regime, $\omega_z \in [-5, 5]$; (b) instantaneous crossflow vorticity field of Fourier mode at the same instant as that of mean flow at $Re = 100$, $\hat{w} \in [-1, 1]$

In the current work, pseudo-Floquet analysis has been carried out using a time-stepping approach by carrying out the following steps. First, two-dimensional time-dependent base flow inside fluidic oscillator is fully resolved using Spectral element method as outlined in §2.2. The time-dependent solution is then integrated until it reaches a statistically stationary state. Then, the two-dimensional converged base flow is perturbed with an infinitesimal three-dimensional perturbation of the following form:

$$\mathbf{u}(x, y, z, t) = \mathbf{U}(x, y, t) + \epsilon \tilde{\mathbf{u}}(x, y, z, t) \tag{4.2}$$

where $\mathbf{u}(x, y, z, t){=}(u, v, w)$ and $\tilde{\mathbf{u}}(x, y, z, t){=}(\tilde{u}, \tilde{v}, \tilde{w})$ are the velocity and perturbation fields. By plugging the above equation back to the Navier-Stokes equations i.e. eq 2.1 and ignoring second and high order terms in ϵ, we seek the evolution of perturbation of order ϵ of the linearized Navier-Stokes equations about the base flow as following

$$\frac{\partial \tilde{\mathbf{u}}}{\partial t} = -(\mathbf{U} \cdot \nabla)\tilde{\mathbf{u}} - (\tilde{\mathbf{u}} \cdot \nabla)\mathbf{U} - \frac{1}{\rho}\nabla \tilde{p} + \frac{1}{Re}\nabla^2 \tilde{\mathbf{u}} \tag{4.3}$$

where $\tilde{p}$ is the perturbation to the pressure that enforces continuity:

$$\nabla \cdot \tilde{\mathbf{u}} = 0 \tag{4.4}$$

Floquet theory is related to the solution of periodic-linearized differential equations which in this case is Eq (4.3) with periodic coefficients defined by the base flow $\mathbf{U}$. The base flow $\mathbf{U}$ stability is characterized by the Floquet multiplier, $\mu = e^{\sigma T}$ such that Fourier modes with $|\mu| > 1$ are the exponentially growing modes (unstable modes).

The fluidic oscillator under present study is homogeneous in the spanwise direction, therefore, the perturbation can be expressed in Fourier expansion as follows

$$\tilde{\mathbf{u}}(x, y, z, t) = \int_{-\infty}^{\infty} \hat{\mathbf{u}}(x, y, \beta, t)e^{i\beta z}d\beta \tag{4.5}$$

A pseudo-Floquet stability analysis is carried out at $Re = 100, 200, 300$ to obtain two objectives: the primary objective is to evaluate the fastest growing modes with their characteristic wavelength that will aid in the selection of spanwise domain length i.e. L_z for three-dimensional studies; and the secondary one is the identification of the location where the fastest growth of the most unstable mode occurs.

A base flow at $Re = 100$ features a pseudo-periodic trajectory in the phase space defined by drag force along the x-axis and shear-force lift component along the $y-$axis.

A range of wave numbers Fourier mode's growth/decay rate is computed to find the fastest growing mode.

Figure 4.12 demonstrates the Floquet multiplier computation at $Re = 100$ in the present work. A phase angle of $\phi = 90°$ in the skin-friction-lift coefficient (viscous lift coefficient) C_{L_v} time series has been used to define the Poincaré section as demonstrated in fig 4.12, where open circle markers denote the Poincaré crossings. Fig 4.12's middle panel indicates the linear growth of single Fourier mode ($\beta = 0.483$) and the right panel features the computation of Floquet multiplier at each crossing. The base flow at $Re = 100$ has a period of 73 time units and it's important to mention here that the growth regime for base flow at $Re = 200$ and 300 is so incredibly unstable to three-dimensional perturbation that in some cases only one Poincaré crossing exists near the middle of the growth regime of the growing mode. Therefore, variability has been defined by a standard deviation of the Floquet multiplier computed at each crossing during growth/decay of the corresponding Fourier mode.

The degree of base flow's instability at different Re can be seen through the value of Floquet multiplier as in fig 4.13. The higher value of μ also contributes to the higher variability, depicted in fig 4.13(b), and 4.13(c) at $\beta = 1.57$, and 1.8, respectively. Absence of error bars in fig 4.13c reflects the fact that μ is computed only at a single crossing.

Figure 4.14 presents the instantaneous vorticity field of the mean flow and the Fourier mode within the linear regime at $Re = 100$. It is interesting to see that Fourier mode grows in the external domain outside the fluidic oscillator, which in order words suggests that flow inside the fluidic oscillator remains essentially two-dimensional at this Re whereas three dimensionality originates in the outside region. The same is also true for $Re = 200$ and 300.

Pseudo-Floquet analysis predicts the most unstable modes wavelengths at $Re = 100$, 200, and 300 given by $\beta = 0.483$, 1.57, and 1.8, respectively. A question arises as to which spanwise domain length for the fluidic oscillator relaxes the requirement of full three-dimensional numerical investigation. It is suggested that two-dimensional investigation might be of practical interest if the fluidic oscillators depth is shorter than the predicted fastest growing modes wavelength computed using pseudo-Floquet analysis and the three-dimensionality triggering location lies outside the fluidic oscillator cavity.
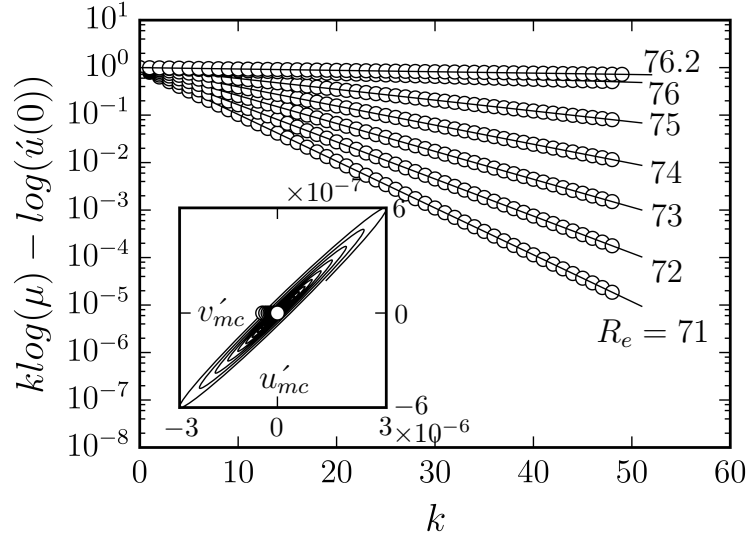
Figure 4.15: Asymptotic evolution of perturbation field around the stable steady state for $2D_t$-case. Sequences of $\tilde{u}_{mc}^{P}$, corresponding to the Poincaré map for $Re \in [71, 76.2]$. Logarithmic fits are denoted by solid lines. A phase map trajectory projected in the phase space that generates a sequence at $Re = 71$ is indicated in the inset. The prime denotes the deviation from the steady state and subscripts represent the probe location *i.e.* mixing chamber, $(0, 0.9h_i)$.

4.3.2 Discussion

In this section, we illuminate the transitional mechanism from the stable steady state to a space-time-symmetric pseudo-periodic state for two-and three-dimensional cases, followed by asymmetric pseudo-periodic transition from the former state for the two-dimensional cases. The methodology of handling the outside chaos will be elucidated.

4.3.2.1 The Hopf bifurcation

In this section, we formulate the characterization of periodic state for two- and three-dimensional cases, followed by characterization of asymmetric pseudo-periodic state from the former state for the two-dimensional case. The methodology of handling the outside chaos will also be elucidated.

The pre-Hopf time history of the field variables display spiraling trend towards approaching asymptotic convergence as illustrated by the phase map trajectories of two-dimensional solution at $Re = 71$ by projecting into the (u'_{mc}, v'_{mc}) phase plane as shown in the inset of fig 4.15, where u'_{mc}, v'_{mc} denote the deviations of streamwise and cross flow velocity components from the steady state measured at probe location $(0, 0.9h_i)$.

Spiraling convergence pertains to the fact that leading eigenmodes are complex conjugate pair approaching the stable focus in a periodic manner. The same approach has been used here as the one adopted in pseudo-Floquet analysis to split the flow field into the mean flow and perturbation field. For sufficiently small perturbation fields of order $O(\epsilon)$ with $\epsilon << 1$, the perturbation nonlinear term, *i.e.* $(\tilde{\mathbf{u}} \cdot \nabla)\tilde{\mathbf{u}}$, becomes negligible $O(\epsilon^2)$ compared to other terms which remain of order $O(\epsilon)$. The momentum and conservation of mass equations after linearizing look exactly as Eq's (4.3) and (4.4). The linearized system of equations becomes generalized eigenproblem where leading eigenmode determines the nature of the solution. In the linear regime, dynamics is governed by normal modes and final solution can take the form of superposition of the evolution of individual eignmodes as follows

$$(\tilde{\mathbf{u}}, \tilde{p})(t) = \sum b_i(\hat{\mathbf{u}}_\mathbf{i}, \hat{p}_i)e^{\lambda_i t} \tag{4.6}$$

where b_i is the projection of the initial perturbation field $(\tilde{\mathbf{u}}, \tilde{p})(0)$ on mode i, with eigenmodes sorted in decreasing order based on the real part of the corresponding eigenvalue. All eigenvalues with complex conjugate have negative real part for a stable focus when perturbation field features exponential decay along all eigendirections, and the dynamics along all manifolds follow the leading eigenmode's manifold. In case of three-dimensional DNS, growing modes interact nonlinearly in the initial transients regime which hinders the use of modal analysis. Nevertheless, once the initial nonlinear regime has been passed, the solution asymptotically evolves towards the linear regime resulting the dynamics to follow the leading eigenmode. For a spiraling convergence, the leading eigenmode is complex conjugate pair $(\hat{\mathbf{u}}_1, \hat{p}_1) = (\hat{\mathbf{u}}_1^r, \hat{p}_1^r) \pm i(\hat{\mathbf{u}}_1^i, \hat{p}_1^i)$ with complex eigenvalue *i.e.* $\lambda_1 = \lambda_1^r + i\lambda_1^i$, the superscripts r and i denotes real and imaginary part, respectively. As the solution goes into the asymptotic linear regime, all field variables follow periodic slowly-converging pattern for a stable focus with shared frequency and damping rate, ultimately, yielding the final solution. Perturbation field's velocity components follow the decay as following

$$\begin{aligned}
\tilde{u}_{mc} &= b_1\hat{u}_{mc}e^{(\lambda_1^r+\lambda_1^i)t} + c.c. \\
\tilde{v}_{mc} &= b_1\hat{v}_{mc}e^{(\lambda_1^r+\lambda_1^i)t} + c.c.
\end{aligned} \tag{4.7}$$

where $c.c.$ denote the complex conjugate, and b_1 is the initial condition uniquely determined from the perturbation field at time origin. Eq (4.7) suggests that all degrees of freedom follow the leading eigenmode in the exponentially oscillating manner. The critical Re can be estimated along with the corresponding frequency and

damping rate by monitoring the leading eigenmode and the corresponding eigenvalues i.e. λ^r, λ^i preceding the transition of stable focus into the progressively amplitude-increasing periodic orbits. It would require prohibitive number of cases in the vicinity of critical Re which could be overcome by fitting an exponential curve to the available data points using Poincaré maps. In Poincaré method, we define a Poincaré section and observe the resulting discrete-time dynamics. Poincaré section and map are defined as follows

$$S = (\tilde{\mathbf{u}}, \tilde{p}) : \tilde{v}_{mc} = 0, \dot{\tilde{v}}_{mc} = 0$$
$$P : S \mapsto S \tag{4.8}$$
$$b^P \mapsto P(b^P) = \Phi_{T^P}(b^P)$$

Poincaré map converts the continuous-time dynamics to discrete-time by mapping current state a^P to the next state $P(a^P)$ after a lapse of time τ, where τ is the flight time from one mapping to the other. Successive application of Poincaré map results in a sequence, $a^P(k)$ with the corresponding sequence of flight times $t^P(k)$ for each flight as $T^P(k) = t^P(k) - t^P(k-1) = \frac{2\pi}{\lambda_1^i}$.

$$t^P(k) = t^P(0) + T^P k$$
$$\tilde{u}_{mc}^P(k) = \tilde{u}_{mc}^P(0)\mu^k \tag{4.9}$$

where μ is the Floquet multiplier/dominant multiplier of the fixed point of the corresponding Poincaré map. In the linear regime, all degree of freedom converge to the fixed point asymptotically, therefore, λ_1^i can be estimated as

$$T^P = \lim_{k \longrightarrow \infty} T^P(k) = \frac{2\pi}{\lambda_1^i}$$
$$\lambda_1^r = \log \mu \frac{1}{T^P} \tag{4.10}$$

Fig 4.15 illustrates the sequences of flow state approaching the stable steady state, and the solid line denotes the logarithmic fits to the exponential tails. The inset fig features a phase map trajectory projected onto the $(\tilde{u}_{mc}, \tilde{v}_{mc})$ phase plane with Poincaré crossing defined by $\tilde{v}_{mc} = 0, \dot{\tilde{v}}_{mc} = 0$. Critical Re_H can be estimated from the quadratic fit to the last few points of λ_1^r prior to the bifurcation to periodic solutions as shown in fig 4.16(a). The frequency for the branch of periodic orbits at the Re_H can be estimated from a second quadratic fit to last few points of λ_1^i as shown in fig 4.16(a). However, for the two- and three-dimensional full domain cases, all the
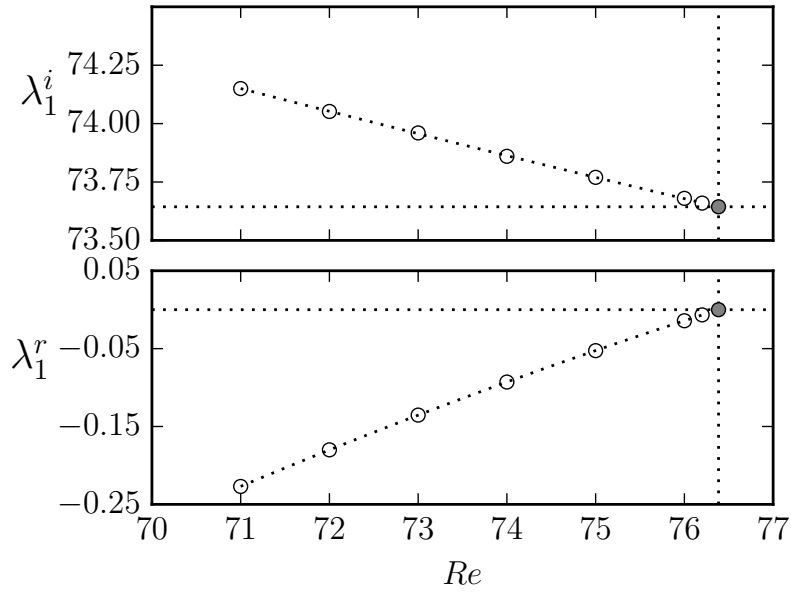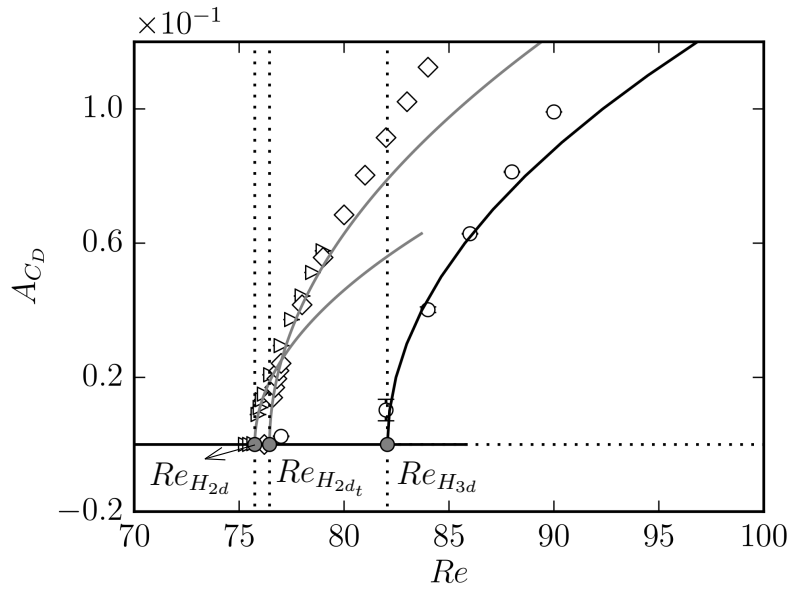
Figure 4.16: Hopf bifurcation for $2D_f$, $2D_t$ and, three-dimensional cases. (a) real (damping rate) and imaginary (frequency) part of leading eigenvalue close to the bifurcation point fitted with quadratic polynomial for $2D_t$. (b) Drag coefficient amplitude vs Re of the periodic solution for two-dimensional case, two-dimensional case with external domain truncated and, three-dimensional solution. The filled grey circles denote bifurcation point of the corresponding solution. The dotted line through points represent square root fit. Circles for three-dimensional solutions, diamonds for two-dimensional truncated domain, and triangles for two-dimensional solutions

solutions were plotted against Re, and square root fit was applied to the periodic solution close to the bifurcation point, yielded the Re_H for the corresponding cases, i.e. $Re_{H_{2d}} = 75.745, Re_{H_{3d}} = 82.063$, for the two- and three-dimensional solutions as shown in fig 4.16(b). Square root fit with vanishing linear term confirms the supercritical nature of Hopf bifurcation for all three cases. The physical properties of the jet inside cavity features very high degree of resemblance between three cases (two-dimensional truncated domain, two-dimensional full domain, and three-dimensional) such as sweeping frequency, phase map trajectories, jet topology at corresponding phase angles etc. Therefore, it can be concluded that jet oscillation is governed by the same mechanism, i.e. supercritical Hopf bifurcation, for all three cases. The time traces of the modal energy for three-dimensional case demonstrate that Hopf instability in the flow regime between $Re_{H_{2d}}$ and $Re_{H_{3d}}$ is suppressed by the inception of three-dimensionality. Furthermore, it can be concluded that existance of the outer buffer zone shifts the Re_c to earlier value.

4.3.2.2 The Pitchfork bifurcation

The drag coefficient amplitude and upstream effect of chaos inside mixing chamber cavity keep on building up with increase in Re for two-dimensional periodic solutions of Navier-Stokes equations. Consequently, the mixing chamber cavity dynamics becomes highly nonlinear with the appearance of more small-scale vortices as shown in fig 4.10. Nevertheless, the internal jet features space-time symmetry about the fluidic oscillator axis i.e. $y = 0$ for $Re \leqslant 294$. However, space-time symmetry has been found to be broken for two-dimensional pseudo-periodic solutions for $Re \geqslant 294.31$ and $Re \geqslant 294.42$ through pitchfork bifurcation for full and truncated domain, respectively. Again, Poincaré map has been employed to define the bifurcation parameters. First, drag coefficients of the upper and lower mixing chamber lateral walls were obtained at the Poincaré crossings, defined by $C_l = 0, \dot{C}_l > 0$, after the pseudo-periodic two-dimensional solution had approached converged state. Normal distribution function was fit to the data points following the normality test. The lower wall drag coefficient was scaled by -1 to estimate the degree of asymmetry. The difference distribution function defined the bifurcation parameter and two-standard deviation was considered to have 95% certainty. Fig 4.17 illustrate the pitchfork bifurcation of two-dimensional pseudo-periodic solutions of incompressible Navier-Stokes equations over a range of Re. A square root fit, with vanishing linear term, to the trailing data points confirms the supercritical nature of the bifurcation for both cases. The error bars corresponding to each data point represent 95% confidence level which indicates
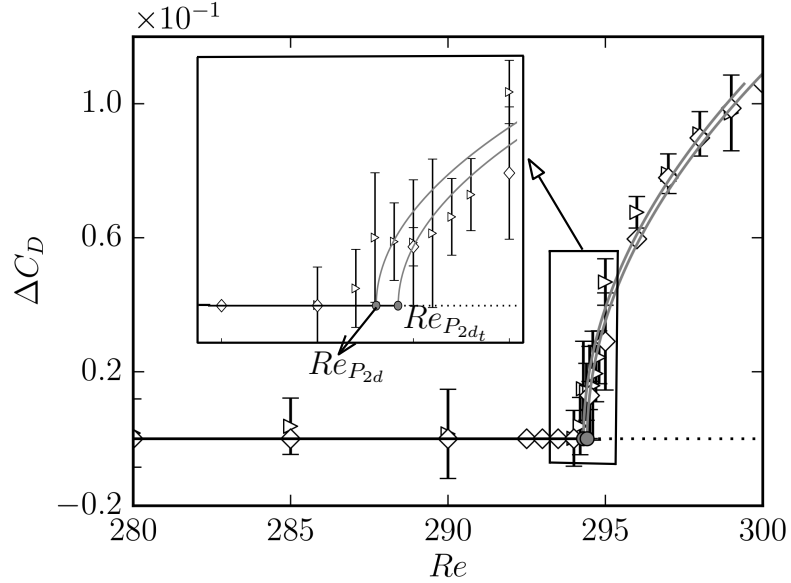
Figure 4.17: Pitchfork bifurcation diagram for two-dimensional pseudo-periodic solutions of Navier-Stokes equations.(triangles:two-dimensional full domain, diamonds:two-dimensional truncated domain) The error bars indicate the 95% confidence interval

that we are 95% certain about the fitting curve that it would pass through the given data point. Also, we are 95% confident that $Re_{P_{2d}} = 294.31$ and $Re_{P_{2d_t}} = 294.42$ are the the critical Reynolds number for two-dimensional full- and truncated-domains, respectively.

4.4 Conclusions

In this chapter, time-dependence study of the flow inside novel laminar fluidic oscillator has been carried out using high order spectral element methods (SEM). Spanwise Fourier modes of length scales i.e. $L_z \geqslant 3.5h_i$ are found to be the most unstable ones for $Re \geqslant 300$, predicted by pseudo Floquet analysis, which provided justification for the two-dimensioal study in the laminar regime. It was found that the stable steady state flow inside fluidic oscillator cavity transits to periodic state through supercritical Hopf bifurcation for both two- and three-dimensional cases. The critical Reynolds number for two-($Re_{H_{2d}}$) and three-dimensional ($Re_{H_{3d}}$) flow were found to be $Re_{H_{2d}} = 75.745$ and $Re_{H_{3d}} = 82.063$, respectively. Three-dimensionality was found to suppress the two-dimensional Hopf instability in the flow regime between $Re_{H_{2d}}$ and $Re_{H_{3d}}$. The secondary transition of two-dimensional cavity flow was found to be

governed by the supercritical Pitchfork bifurcation of orbits. The critical Reynolds number (Re_P) for the pitchfork bifurcation was found to be $Re_P = 294.31$.

Chapter 5

Conclusions and future work

This chapter concludes the work of this dissertation and presents novel contributions made to the wealth of numerical data in the field of aerodynamics with particular attention paid to the active flow control methods in the transitional regime.

Flow past a circular cylinder being a canonical problem for flow past bluff bodies has been the most studied configuration as it provides a wealth of knowledge about the complex phenomena occurring in the wake of bluff bodies such as separating shear layers, turbulent transition of shear layers and wake instabilities in the transitional flow regime. These separating shear layers are at the origin of massive wakes that result in higher aerodynamic drag, vibration and acoustic noise etc. Active flow control is implemented via numerical experiments on flow past circular cylinder at $Re = 2000$ using novel time-dependent spanwise-dependent forcing technique with the goal to achieve improved aerodynamic performance. This thesis also investigates the time-dependent characterisation of flow inside a novel laminar-fluidic-oscillator, a suitable candidate for AFC applications.

Flow past circular cylinder is fully resolved using high order Spectral/h-p methods at $Re = 2000$. It has been found that spanwise domain length $L_z \gtrsim 2.5D$ is sufficient to compute the correct first and higher order flow statistics in the near- and far-wake. The long-standing controversy of U- and V-state of the streamwise velocity cross-stream profile in this flow regime has been settled via scaling the corresponding recirculation bubbles and comparing the wake statistics at the relative locations. Footprints of intermittent shear layer vortices have been observed in the spectra of streamwise and crossflow velocities characterized by broadband peak at frequencies other than fundamental frequency and/or their harmonics that are consistent with the experimental observations. A phase difference of 225° between the primary and secondary instabilities was observed via decomposition the flow velocity into primary and secondary components that pointed out the occurrence of streamwise vortices in

the braid regions between the large scale von Kármán type vortecies having opposite sense of spanwise vorticity.

Spanwise wavelength of secondary disturbance has been quantified using Hilbert transform of the pseudo crossflow component of vorticity. Streamwise and cross-stream evolution of the average wavelength display opposite behavior in the shear layer and wake regions: in the shear layer region, average wavelength decreases as a function of streamwise distance until it reaches a minimum value and increases thereafter in the wake region. The three-dimensional disturbance is seen to be strongest in the near wake region close to the large-scale spanwise vortex formation corroborated by previous investigations.

Linear stability analysis of time-dependent two-dimensional wakeflow via time-stepping approach predicts the spanwise wavelength of the least stable mode and the corresponding spatial location where the growth rate in the linear regime is maximized at $Re = 2000$, in remarkable agreement with the DNS study and experimental measurements of Mansy et al. [14].

In chapter 3, AFC in the form of blowing and suction from the top and bottom slots of the circular cylinder is implemented at $Re = 2000$ to improve aerodynamics performance. Parametric exploration is sought to find the optimal forcing wavelength and amplitude using in-phase spanwise-dependent time-independent forcing. Unsteadiness is investigated by time-periodic spanwise dependent forcing and spanwise traveling sinusoids with variable speed. Reduction in the lift fluctuations and drag is the greatest for SDTI case followed by STS cases with a forcing frequencies $0.5f_e$ and f_e, and PSD case with an actuation frequency of f_{vK}. It is observed that applied forcing causes spanwise distortion of shear layer evolution locally that ultimately leads to drag reduction and suppression of lift fluctuations. However, PSD forcing with $4f_{\mathrm{vK}}$ amplifies vortex shedding and drag coefficient which makes it suitable for energy harvesting applications.

In chapter 4, numerical experiments are carried out to investigate the time-dependence of flow inside novel laminar fluidic oscillator in the presence of outside chaos. Pseudo-Floquet analysis predicts the wavelengths of the fastest growing modes to be $L_z \geqslant 3.5h_i$ which lends support to the two-dimensional study of fluidic oscillator at $Re \leq 300$, even though three-dimensional simulations are also performed where deemed necessary. It was found that the stable steady state flow inside fluidic oscillator cavity transits to space-time-symmetric periodic state through supercritical Hopf bifurcation for both two- and three-dimensional cases. The critical Reynolds number for two-($Re_{H_{2d}}$) and three-dimensional ($Re_{H_{3d}}$) flow were found to

be $Re_{H_{2d}} = 75.745$ and $Re_{H_{3d}} = 82.063$, respectively, however, flow dynamics inside both two and three-dimensional fluidic oscillators shows remarkable similarity. Moreover, three-dimensionality was found to suppress the two-dimensional Hopf instability in the flow regime between $Re_{H_{2d}}$ and $Re_{H_{3d}}$. The secondary transition of two-dimensional cavity flow was found to be governed by the supercritical Pitchfork bifurcation of cycles. The critical Reynolds number (Re_P) for the pitchfork bifurcation is found to be $Re_P = 294.31$. From a physical viewpoint, cavity jet oscillation in the post Hopf-bifurcation flow regime is mainly driven by pressure force with magnitude almost twice that of the inertial force. However in the post Pitchfork-bifurcation flow regime both the inertial and the pressure forces contribute almost equally to the flipping of the cavity jet. It has been found that pressure force leads the phase as compared to the corresponding inertial force.

Future work

The cylinder wake comprising the shear-layer instability and wake instabilities is almost completely characterized in the transitional flow regime, however, a further investigation to the absolute/convective nature of the shear-layer instability in the context of global instability viewpoint will complement the present work which will be pursued in future.

AFC with unsteady forcing proved a useful technique to improve aerodynamic parameters for flow past bluff bodies. Further experimental investigation at the same Re could be performed to complement the numerical work. It order to further investigate the practical implementation of this technique, implementing discrete slots for forcing the flow past circular cylinder in the in-phase configuration could provide useful results which could not be done in the present work due to high requirement of computational resources.

The time-dependence of flow inside fluidic oscillator has been characterized in the early transition regimes. The first two bifurcations along its route to fully turbulent flow has been evaluated in the present work, however further numerical work at higher Re could unveil the bifurcations leading to fully chaotic flow which constitute the future work. The novel fluidic oscillator could be implemented in a wide range of applications such as mixing enhancement, efficient heat transfer, active flow control.

Bibliography

[1] A. Prasad and C.H.K. Williamson. The instability of the shear layer separating from a bluff body. *J. Fluid Mech.*, 333:375–402, 1997.

[2] A. Seifert, S. Eliahu, D. Greenblatt, and I. Wygnanski. Use of piezoelectric actuators for airfoil separation control. *AIAA J.*, 36(8):1535–1537, 1998.

[3] M. Kotsonis, S. Ghaemi, L. Veldhuis, and F. Scarano. Measurement of the body force field of plasma actuators. *J. Phys. D*, 44(4):045204, 2011.

[4] D. Lockerby. *Numerical simulation of boundary-layer control using MEMS actuation.* PhD thesis, University of Warwick, 2001.

[5] C. Norberg. An experimental investigation of the flow around a circular cylinder: influence of aspect ratio. *J. Fluid Mech.*, 258:287–316, 1994.

[6] C. Norberg. Effects of Reynolds number and a low-intensity freestream turbulence on the flow around a circular cylinder. Technical Report 87/2, Chalmers University, Göteborg, Sweden, 1987.

[7] C. Norberg. Fluctuating lift on a circular cylinder: review and new measurements. *J. Fluids Struct.*, 17(1):57–96, 2003.

[8] E. Konstantinidis and S. Balabani. Flow structure in the locked-on wake of a circular cylinder in pulsating flow: Effect of forcing amplitude. *Int. J. Heat Fluid Flow*, 29(6):1567–1576, 2008.

[9] C Norberg. LDV-measurements in the near wake of a circular cylinder. *ASME Paper No. FEDSM98-521*, 1998.

[10] E. Konstantinidis, S. Balabani, and M. Yianneskis. The effect of flow perturbations on the near wake characteristics of a circular cylinder. *J. Fluids Struct.*, 18(3-4):367–386, 2003.

[11] P. Parnaudeau, J. Carlier, D. Heitz, and E. Lamballais. Experimental and numerical studies of the flow over a circular cylinder at Reynolds number 3900. *Phys. Fluids*, 20(8):085101, 2008.

[12] E. Konstantinidis, S. Balabani, and M. Yianneskis. Conditional averaging of PIV plane wake data using a cross-correlation approach. *Exp. Fluids*, 39(1): 38–47, 2005.

[13] S. Gsell, R. Bourguet, and M. Braza. Three-dimensional flow past a fixed or freely vibrating cylinder in the early turbulent regime. *Phys. Rev. Fluids.*, 3: 013902, Jan 2018.

[14] H. Mansy, P.M. Yang, and D.R. Williams. Quantitative measurements of three-dimensional structures in the wake of a circular cylinder. *J. Fluid Mech.*, 270: 277–296, 1994.

[15] C.K. Chyu and D. Rockwell. Near-wake structure of an oscillating cylinder: effect of controlled shear-layer vortices. *J. Fluid Mech.*, 322:21–49, 1996.

[16] S. Raghu. Fluidic oscillators for flow control. *Exp. Fluids*, 54(2):1455, 2013.

[17] M. N. Tomac and J. W. Gregory. Internal jet interactions in a fluidic oscillator at low flow rate. *Exp. Fluids*, 55(5):1730, 2014.

[18] L. N. Cattafesta III and M. Sheplak. Actuators for active flow control. *Annu. Rev. Fluid Mech.*, 43(1):247–272, 2011.

[19] S. P. Singh and S. Mittal. Flow past a cylinder: shear layer instability and drag crisis. *Int. J. Numer. Methods Fluids*, 47(1):75–98, 2005.

[20] J.H. Gerrard. The wakes of cylindrical bluff bodies at low Reynolds number. *Philosophical Transactions of the Royal Society of London. Series A, Mathematical and Physical Sciences*, 288(1354):351–382, 1978.

[21] B. Kumar, J. J. Kottaram, A. K. Singh, and S. Mittal. Global stability of flow past a cylinder with centreline symmetry. *J. Fluid Mech.*, 632:273–300, 2009.

[22] S. Mittal. Instability of the separated shear layer in flow past a cylinder: Forced excitation. *Int. J. Numer. Methods Fluids*, 56(6):687–702, 2008.

[23] J. Kim and H. Choi. Distributed forcing of flow over a circular cylinder. *Phys. Fluids*, 17(3):033103, 2005.

[24] J. C. Owen, P. W. Bearman, and A. A. Szewczyk. Passive control of viv with drag reduction. *J. Fluids Struct.*, 15(3):597–605, 2001.

[25] G Rocco and SJ Sherwin. stabilisation of the absolute instability of a flow past a cylinder via spanwise forcing at re= 180. *Procedia IUTAM*, 14:115–121, 2015.

[26] P. W. Bearman and J. C. Owen. Reduction of bluff-body drag and suppression of vortex shedding by the introduction of wavy separation lines. *J. Fluids Struct.*, 12(1):123–130, 1998.

[27] D. R. Williams, H. Mansy, and C. Amato. The response and symmetry properties of a cylinder wake subjected to localized surface excitation. *J. Fluid Mech.*, 234:71–96, Jan 1992.

[28] J. C. Lin, J. Towfighi, and D. Rockwell. Near-wake of a circular-cylinder - control by steady and unsteady surface injection. *J. Fluids Struct.*, 9(6):659–669, Aug 1995.

[29] D. Greenblatt and I. J. Wygnanski. Control of flow separation by periodic excitation. 36(7):487–545, 10 2000.

[30] G. B. Schubauer and H. K. Skramstad. Laminar-boundary-layer oscillations and transition on a flat plate. Technical report, NATIONAL AERONAUTICS AND SPACE ADMINISTRATION WASHINGTON DC, 1948.

[31] M. Samimy, I. Adamovich, B. Webb, J. Kastner, J. Hileman, S. Keshav, and P. Palm. Development and characterization of plasma actuators for high-speed jet control. *Exp. Fluids*, 37(4):577–588, 2004.

[32] B. Cybyk, K. Grossman, and J. Wilkerson. Performance characteristics of the sparkjet flow control actuator. In *2nd AIAA Flow Control Conference*, page 2131, 2004.

[33] S. Raghu. Feedback-free fluidic oscillator and method, July 3 2001. US Patent 6,253,782.

[34] R. W. Warren. Fluid oscillator, January 9 1962. US Patent 3,016,066.

[35] Th. v. Karmn. ber den mechanismus des wiederstandes, den ein bewegter korper in einer flssigkeit erfahrt. *Nachrichten von der Gesellschaft der Wissenschaften zu Gttingen, Mathematisch-Physikalische Klasse*, 1912:547–556, 1912.

[36] R.D. Henderson. Details of the drag curve near the onset of vortex shedding. *Phys. Fluids*, 7(9):2102–2104, 1995.

[37] D. Barkley and R.D. Henderson. Three-dimensional floquet stability analysis of the wake of a circular cylinder. *J. Fluid Mech.*, 322:215–241, Sep 10 1996.

[38] T. Sarpkaya. Vortex-induced oscillations: a selective review. *J. Appl. Mech.*, 46 (2):241–258, 1979.

[39] N. Ferguson and G.V. Parkinson. Surface and wake flow phenomena of the vortex-excited oscillation of a circular cylinder. *J. Eng. Ind.*, 89(4):831–838, 1967.

[40] J. C. Hardin and S. L. Lamkin. Aero-acoustic computation of cylinder wake flow. *AIAA J.*, 22(1):51–57, 1984.

[41] M. S. Howe. *Frontmatter*, pages i–vi. Cambridge Monographs on Mechanics. Cambridge University Press, 1998.

[42] C.H.K. Williamson. Mode A secondary instability in wake transition. *Phys. Fluids*, 8(6):1680–1682, 1996.

[43] R. D. Henderson and D. Barkley. Secondary instability in the wake of a circular cylinder. *Phys. Fluids*, 8(6):1683–1685, 1996.

[44] C.H.K. Williamson. The existence of two stages in the transition to three dimensionality of a cylinder wake. *Phys. Fluids*, 31(11):3165–3168, 1988.

[45] A. Roshko. On the development of turbulent wakes from vortex streets. Technical report, 1954.

[46] M.S. Bloor. The transition to turbulence in the wake of a circular cylinder. *J. Fluid Mech.*, 19(2):290–304, 1964.

[47] L. Schiller and W. Linke. Druck-und reibungswiderstand des zylinders bei reynoldss- chen zahlen 5000 bis 40000. *Z. Flugtech. Motorluft*, 24:193–198, 1933.

[48] A. Prasad and C.H.K. Williamson. The instability of the separated shear layer from a bluff body. *Phys. Fluids*, 8(6):1347–1349, 1996.

[49] C.H.K. Williamson. Three-dimensional transition in the near wake of a cylinder. *Bull. Am. Phys. Soc.*, 32:2098, 1987.

[50] C.H.K. Williamson, J. Wu, and J. Sheridan. Scaling of streamwise vortices in wakes. *Phys. Fluids*, 7(10):2307–2309, 1995.

[51] H.Q. Zhang, U. Fey, B. R. Noack, M. Knig, and H. Eckelmann. On the transition of the cylinder wake. *Phys. Fluids*, 7(4):779–794, 1995.

[52] J. Wu, J. Sheridan, M. C. Welsh, and K. Hourigan. Three-dimensional vortex structures in a cylinder wake. *J. Fluid Mech.*, 312:201–222, 1996.

[53] I. Wygnanski, F. Champagne, and B. Marasli. On the large-scale structures in two-dimensional, small-deficit, turbulent wakes. *J. Fluid Mech.*, 168:31–71, 1986.

[54] W.K. George. Asymptotic effect of initial and upstream conditions on turbulence. *J. Fluids Eng.*, 134(6):061203, 2012.

[55] Y. Zhou and R. Antonia. Effect of initial conditions on characteristics of turbulent far wake. *JSME Int. J. Ser. B*, 37(4):718–725, 1994.

[56] G.L. Brown and A. Roshko. Turbulent shear layers and wakes. *J. Turb.*, 13: N51, 2012.

[57] S.L. Tang, R.A. Antonia, L. Djenidi, and Y. Zhou. Complete self-preservation along the axis of a circular cylinder far wake. *J. Fluid Mech.*, 786:253274, 2016.

[58] Y. Zhou, R. A. Antonia, and W.K. Tsang. The effect of Reynolds number on a turbulent far-wake. *Exp. Fluids*, 25(2):118–125, Jul 1998.

[59] L.M. Lourenco and C. Shih. Characteristics of the plane turbulent near wake of a circular cylinder, a particle image velocimetry study. Taken from [62], 1993.

[60] Y. Zhou and R. A. Antonia. A study of turbulent vortices in the near wake of a cylinder. *J. Fluid Mech.*, 253:643–661, 1993.

[61] L. Ong and J. Wallace. The velocity field of the turbulent very near wake of a circular cylinder. *Exp. Fluids*, 20(6):441–453, 1996.

[62] P. Beaudan and P. Moin. Numerical experiments on the flow past a circular cylinder at sub-critical Reynolds number. Technical report, NASA STI/Recon Technical Report N, dec 1994.

[63] R. Mittal. Progress on LES of flow past a circular cylinder. *CTR Annual Research Briefs*, pages 233–241, 1996.

[64] M. Breuer. Large eddy simulation of the subcritical flow past a circular cylinder: numerical and modeling aspects. *Int. J. Numer. Methods Fluids*, 28(9):1281–1302, 1998.

[65] X. Ma, G.S. Karamanos, and G.E. Karniadakis. Dynamics and low-dimensionality of a turbulent near wake. *J. Fluid Mech.*, 410:29–65, 2000.

[66] A.G. Kravchenko and P. Moin. Numerical studies of flow over a circular cylinder at Re_D=3900. *Phys. Fluids*, 12(2):403–417, 2000.

[67] J. Franke and W. Frank. Large eddy simulation of the flow past a circular cylinder at Re= 3900. *J. Wind Eng. Ind. Aerod.*, 90(10):1191–1206, 2002.

[68] O. Lehmkuhl, I. Rodríguez, R. Borrell, and A. Oliva. Low-frequency unsteadiness in the vortex formation region of a circular cylinder. *Phys. Fluids*, 25(8): 085109, 2013.

[69] H. Ouvrard, B. Koobus, A. Dervieux, and M.V. Salvetti. Classical and variational multiscale LES of the flow around a circular cylinder on unstructured grids. *Comput. Fluids*, 39(7):1083–1094, 2010.

[70] I. Afgan, Y. Kahil, S. Benhamadouche, and P. Sagaut. Large eddy simulation of the flow around single and two side-by-side cylinders at subcritical reynolds numbers. *Phys. Fluids*, 23(7):075101, 2011.

[71] H. Chen, Z. Li, and Y. Zhang. U or V shape: Dissipation Effects on Cylinder Flow Implicit Large-Eddy Simulation. *AIAA J.*, 55(2):459–473, 2016.

[72] F. Tremblay. *Direct and large-eddy simulation of flow around a circular cylinder at subcritical Reynolds numbers.* PhD thesis, Technische Universität München, 2002.

[73] S. Dong, G.E. Karniadakis, A. Ekmekci, and D. Rockwell. A combined direct numerical simulation–particle image velocimetry study of the turbulent near wake. *J. Fluid Mech.*, 569:185–207, 2006.

[74] R. Mittal. Large-eddy simulation of flow past a circular cylinder. Technical report, 1995.

[75] A.H. Mohammad, Z.J. Wang, and C. Liang. Large eddy simulation of flow over a cylinder using high-order spectral difference method. *Adv. Appl. Math. Mech.*, 2(4):451–466, 2010.

[76] G. Lodato and A. Jameson. Les modeling with high-order flux reconstruction and spectral difference schemes. *ICCFD paper*, 2201:9–13, 2012.

[77] J.G. Wissink and W. Rodi. Numerical study of the near wake of a circular cylinder. *Int. J. Heat Fluid Flow*, 29(4):1060–1070, 2008.

[78] R.D. Peltzer. The effect of upstream shear and surface roughness on the vortex shedding patterns and pressure distributions around a circular in transitional Reynolds number flows. *MSc, VPI and SU*, 1980.

[79] H.G.-C. Woo, J.A. Peterka, and J.E. Cermak. Experiments on vortex shedding from stationary and oscillating cables in a linear shear flow. Technical report, 1981.

[80] J.H. Gerrard. Experimental investigation of seperated boundary layer undergoing transition to turbulence. *Phys. Fluids*, 10(9P2):S98–&, 1967.

[81] A. Prasad and C. H. K. Williamson. Three-dimensional effects in turbulent bluff-body wakes. *J. Fluid Mech.*, 343:235–265, 1997.

[82] C.D. Cantwell, D. Moxey, A. Comerford, A. Bolis, G. Rocco, G. Mengaldo, D. De Grazia, S. Yakovlev, J.-E. Lombard, D. Ekelschot, B. Jordi, H. Xu, Y. Mohamied, C. Eskilsson, B. Nelson, P. Vos, C. Biotto, R.M. Kirby, and S.J. Sherwin. Nektar++: An open-source spectral/hp element framework. *Comput. Phys. Commun.*, 192:205 – 219, 2015.

[83] C. H. K. Williamson. Vortex dynamics in the cylinder wake. *Annu. Rev. Fluid Mech.*, 28(1):477–539, 1996.

[84] C.H.K. Williamson. Three-dimensional wake transition. *J. Fluid Mech.*, 328: 345–407, 1996.

[85] B. R. Noack and H. Eckelmann. A global stability analysis of the steady and periodic cylinder wake. *J. Fluid Mech.*, 270:297–330, 1994.

[86] H. Choi, W.P. Jeon, and J. Kim. Control of flow over a bluff body. *Annu. Rev. Fluid Mech.*, 40:113–139, 2008.

[87] S. Rashidi, M. Hayatdavoodi, and J. A. Esfahani. Vortex shedding suppression and wake control: A review. 126:57–80, Nov 1 2016.

[88] I. J. Wygnanski. A century of active control of boundary layer separation: A personal view. In *Solid Mechanics and its Applications*, volume 129, pages 155–165, 2006.

[89] P.R. Ashill. Flow control: Passive, active, and reactive flow management m. gad-el-hak cambridge university press, the edinburgh building, cambridge cb2 2ru, uk. 2000. 421pp. illustrated. 60. isbn 0-521-77006-8. 105(1045):150–150, 2001.

[90] S. Dong, G. S. Triantafyllou, and G. E. Karniadakis. Elimination of vortex streets in bluff-body flows. *Phys. Rev. Lett.*, 100:204501, May 2008.

[91] M Tanner. A method for reducing the base drag of wings with blunt trailing edge. 23(1):15–23, 1972.

[92] N. Tombazis and P. W. Bearman. A study of three-dimensional aspects of vortex shedding from a bluff body with a mild geometric disturbance. *J. Fluid Mech.*, 330:85–112, 1997.

[93] R. M. Darekar and S. J. Sherwin. Flow past a square-section cylinder with a wavy stagnation face. *J. Fluid Mech.*, 426:263–295, 2001.

[94] G. Rocco and S. J. Sherwin. Stabilisation of the absolute instability of a flow past a cylinder via spanwise forcing at re=180. volume 14 of *Procedia IUTAM*, pages 115–121, 2015.

[95] G. Del Guercio, C. Cossu, and G. Pujals. Optimal streaks in the circular cylinder wake and suppression of the global instability. *J. Fluid Mech.*, 752: 572–588, Aug 2014.

[96] T. S. Leu and C. Ming H. Control of global instability in a non-parallel near wake. *J. Fluid Mech.*, 404:345–378, 2000.

[97] P. A. Monkewitz, P. Huerre, and J. M. Chomaz. Global linear stability analysis of weakly non-parallel shear flows. *J. Fluid Mech.*, 251:1–20, 1993.

[98] F. Giannetti and P. Luchini. Structural sensitivity of the first instability of the cylinder wake. *J. Fluid Mech.*, 581:167–197, 2007.

[99] G. Del Guercio, C. Cossu, and G. Pujals. Stabilizing effect of optimally amplified streaks in parallel wakes. *J. Fluid Mech.*, 739:37–56, Jan. 2014.

[100] G. Del Guercio, C. Cossu, and G. Pujals. Optimal perturbations of non-parallel wakes and their stabilizing effect on the global instability. *Phys. Fluids*, 26(2), Feb 2014.

[101] B. Marasli, F. H. Champagne, and I. J. Wygnanski. Modal decomposition of velocity signals in a plane, turbulent wake. *J. Fluid Mech.*, 198:255–273, Jan 1989.

[102] S. J. Lee and H. B. Kim. The effect of surface protrusions on the near wake of a circular cylinder. *J. Wind Eng. Ind. Aerod.*, 69:351–361, 1997. Proceedings of the 3rd International Colloqium on Bluff Body Aerodynamics and Applications.

[103] S. Jeon, J. Choi, W. P. Jeon, H. Choi, and J. Park. Active control of flow over a sphere for drag reduction at a subcritical reynolds number. *J. Fluid Mech.*, 517:113–129, 2004.

[104] N Fujisawa and G Takeda. Flow control around a circular cylinder by internal acoustic excitation. *J. Fluids Struct.*, 17(7):903–913, Jun 2003.

[105] J. Jeong and F. Hussain. On the identification of a vortex. *J. Fluid Mech.*, 285: 69–94, 1995.

[106] A. Kourta, H.C. Boisson, P. Chassaing, and H. Ha. Minh. Nonlinear interaction and the transition to turbulence in the wake of a circular cylinder. *J. Fluid Mech.*, 181:141–161, 1987.

[107] M. Braza, P. Chassaing, and H.Ha. Minh. Prediction of large-scale transition features in the wake of a circular cylinder. *Phys. Fluids A*, 2(8):1461–1471, 1990.

[108] A. Glezer and M. Amitay. Synthetic jets. *Annu. Rev. Fluid Mech.*, 34(1): 503–529, 2002.

[109] C. L. Thill, J. Etches, I. Bond, K. Potter, and P. Weaver. Morphing skins. *AJ*, 112(1129):117–139, 2008.

[110] Y. Katz, B. Nishri, and I. Wygnanski. The delay of turbulent boundary layer separation by oscillatory active control. *Phys. Fluids A*, 1(2):179–181, 1989.

[111] H. Viets, M. Piatt, and M. Ball. Boundary layer control by unsteady vortex generation. *J. Wind Eng. Ind. Aerod.*, 7(2):135–144, 1981.

[112] E. Moreau. Airflow control by non-thermal plasma actuators. 40(3):605, 2007.

[113] J. W. Gregory, J. P. Sullivan, and S. Raghu. Visualization of jet mixing in a fluidic oscillator. 8(2):169–176, 2005.

[114] M. N. Tomac and J. Gregory. Frequency studies and scaling effects of jet interaction in a feedback-free fluidic oscillator. In *50th AIAA Aerospace Sciences Meeting including the New Horizons Forum and Aerospace Exposition*, page 1248, 2012.

[115] C. E. Spyropoulos. A sonic oscillator. In *????????*, volume Vol. III, pages 27–52, 1964.

[116] W. Gaylord and V. Carter. Fluerics. 27. Flueric temperature-sensing oscillator design. Technical report, Harry Diamond Labs Washington DC, 1969.

[117] R. Woszidlo, F. Ostermann, C. N. Nayeri, and C. O. Paschereit. The time-resolved natural flow field of a fluidic oscillator. *Exp. Fluids*, 56(6):125, 2015.

[118] B. C. Bobusch, R. Woszidlo, J. M. Bergada, C. N. Nayeri, and C. O. Paschereit. Experimental study of the internal flow structures inside a fluidic oscillator. *Exp. Fluids*, 54(6):1559, 2013.

[119] M. Baghaei and J. M. Bergada. Analysis of the forces driving the oscillations in 3d fluidic oscillators. *Energies*, 12(24):4720, 2019.

[120] D. Culley. Variable frequency diverter actuation for flow control. In *3rd AIAA Flow Control Conference*, page 3034, 2006.

[121] D. Guyot, P. Taticchi Mandolini Borgia, C. O. Paschereit, and S. Raghu. Active control of combustion instability using a fluidic actuator. In *46th AIAA Aerospace Sciences Meeting and Exhibit*, page 1058, 2008.

[122] D. Guyot, B. Bobusch, C. O. Paschereit, and S. Raghu. Active combustion control using a fluidic oscillator for asymmetric fuel flow modulation. In *44th AIAA/ASME/SAE/ASEE Joint Propulsion Conference & Exhibit*, page 4956, 2008.

[123] D. Guyot, C. O. Paschereit, and S. Raghu. A fluidic actuator for active combustion control. In *ASME Turbo Expo 2008: Power for Land, Sea, and Air*, pages 583–595. American Society of Mechanical Engineers, 2008.

[124] D. E. Culley, M. M. Bright, P. S. Prahst, and A. J. Strazisar. Active flow separation control of a stator vane using embedded injection in a multistage compressor experiment. 126(1):24–34, 2004.

[125] W. B. Zimmerman, B. N. Hewakandamby, V.áclav Tesař, H. C. H. Bandulasena, and O. A. Omotowa. On the design and simulation of an airlift loop bioreactor with microbubble generation by fluidic oscillation. 87(3):215–227, 2009.

[126] H. Viets. Flip-flop jet nozzle. *AIAA J.*, 13(10):1375–1379, 1975.

[127] G. Raman, E. J. Rice, and D. M. Cornelius. Evaluation of flip-flop jet nozzles for use as practical excitation devices. *J. Fluids Eng.*, 116(3):508–515, 1994.

[128] R. Seele, P. Tewes, R. Woszidlo, M. A. McVeigh, N. J. Lucas, and I. J. Wygnanski. Discrete sweeping jets as tools for improving the performance of the v-22. 46(6):2098–2106, 2009.

[129] C. Cerretelli and K. Kirtley. Boundary layer separation control with fluidic oscillators. 131(4):041001, 2009.

[130] G. Raman and S. Raghu. Cavity resonance suppression using miniature fluidic oscillators. *AIAA J.*, 42(12):2608–2612, 2004.

[131] G. Raman and S. Raghu. Miniature fluidic oscillators for flow and noise control-transitioning from macro to micro fluidics. In *Fluids 2000 Conference and Exhibit*, page 2554, 2000.

[132] E. Phillips, R. Woszidlo, and I. Wygnanski. The dynamics of separation control on a rapidly actuated flap. In *5th Flow Control Conference*, page 4246, 2010.

[133] J. Wilson, D. Schatzman, E. Arad, A. Seifert, and T. Shtendel. Suction and pulsed-blowing flow control applied to an axisymmetric body. *AIAA J.*, 51(10): 2432–2446, 2013.

[134] M. Metka and J. W. Gregory. Drag reduction on the 25-deg ahmed model using fluidic oscillators. *J. Fluids Eng.*, 137(5):051108, 2015.

[135] H.-J. Schmidt, R. Woszidlo, C. N. Nayeri, and C. O. Paschereit. Drag reduction on a rectangular bluff body with base flaps and fluidic oscillators. *Exp. Fluids*, 56(7):151, 2015.

[136] M. DeSalvo, E. Whalen, and A. Glezer. High-lift enhancement using fluidic actuation. In *48th AIAA Aerospace Sciences Meeting Including the New Horizons Forum and Aerospace Exposition*, page 863, 2010.

[137] M. Desalvo, E. Whalen, and A. Glezer. High-lift enhancement using active flow control. In *6th AIAA flow control conference*, page 3245, 2012.

[138] P. Tewes, L. Taubert, and I. Wygnanski. On the use of sweeping jets to augment the lift of a lambda-wing. In *28th AIAA applied aerodynamics conference*, page 4689, 2010.

[139] S. Endrikat, B. Roentsch, J. C. Little, L. Taubert, C. Farbos de Luzan, E. J. Gutmark, and I. J. Wygnanski. Physics and control of the flow over a generic trapezoidal wing planform. In *54th AIAA Aerospace Sciences Meeting*, page 1823, 2016.

[140] M. P. Jentzsch, L. Taubert, and I. J. Wygnanski. On the use of sweeping jets to trim and control a tailless aircraft model. In *35th AIAA Applied Aerodynamics Conference*, page 3042, 2017.

[141] C. Otto, P. Tewes, J. C. Little, and R. Woszidlo. Comparison of fluidic oscillators and steady jets for separation control on a wall-mounted hump. In *2018 AIAA Aerospace Sciences Meeting*, page 1281, 2018.

[142] E. A. Whalen, M. Spoor, P. M. Vijgen, J. Tran, A. Shmilovich, J. C. Lin, and M. Andino. Full-scale flight demonstration of an active flow control enhanced vertical tail. In *8th AIAA Flow Control Conference*, page 3927, 2016.

[143] A. Shmilovich, Y. Yadlin, and E. Whalen. Computational evaluation of flow control for enhanced control authority of a vertical tail. *AIAA J.*, pages 2211–2220, 2016.

[144] S. Raghu, Gregory J. W., and Sullivan JP. Modulated high frequency fluidic actuators for flow control (flow control 2). In *The Proceedings of the International Conference on Jets, Wakes and Separated Flows (ICJWSF) 2005*, pages 465–469. The Japan Society of Mechanical Engineers, 2005.

[145] T. M. Crittenden and S. Raghu. Combustion powered actuator with integrated high frequency oscillator. 1(1):87–97, 2009.

[146] G. Suárez M. Instability mechanisms of fluidic oscillators. B.S. thesis, Universitat Politècnica de Catalunya, 2017.

[147] H. M. Blackburn and J. M. Lopez. On three-dimensional quasiperiodic floquet instabilities of two-dimensional bluff body wakes. *Phys. Fluids*, 15(8):L57–L60, 2003.